Materials Science & Engineering R 137 (2019) 38–65

Contents lists available at ScienceDirect

Materials Science & Engineering R

journal homepage: www.elsevier.com/locate/mser

Low dimensional metal halide perovskites and hybrids

Chenkun Zhou[a], Haoran Lin[b], Qingquan He[b], Liangjin Xu[b], Michael Worku[c], Maya Chaaban[b], Sujin Lee[b], Xiaoqin Shi[b,d], Mao-Hua Du[e], Biwu Ma[a,b,c,*]

[a] Department of Chemical and Biomedical Engineering, FAMU-FSU College of Engineering, Tallahassee, Florida, 32310, United States
[b] Department of Chemistry and Biochemistry, Florida State University, Tallahassee, Florida, 32306, United States
[c] Materials Science and Engineering Program, Florida State University, Tallahassee, Florida, 32306, United States
[d] School of Materials Science and Engineering, Nanjing University of Science and Technology, Nanjing, 210094, China
[e] Materials Science & Technology Division, Oak Ridge National Laboratory, Oak Ridge, Tennessee, 37831, United States

ARTICLE INFO

Keywords:
Low dimensionality
Organic metal halide hybrids
Halide Perovskites
Nanomaterials
Optoelectronics

ABSTRACT

Organic-inorganic metal halide hybrids are an important class of crystalline materials with exceptional structural and property tunability. Recently metal halide perovskites with ABX_3 structure have been extensively investigated as new generation semiconductors for various optoelectronic devices, including photovoltaic cells, light emitting diodes, photodetectors, and lasers, for their exceptional optical and electronic properties. By controlling the morphological dimensionality, low dimensional metal halide perovskites, including 2D perovskite nanoplatelets, 1D perovskite nanowires, and 0D perovskite quantum dots, have been developed to exhibit distinct properties from their bulk counterparts, due to quantum size effects. Besides ABX_3 perovskites, organic-inorganic metal halide hybrids, containing the same fundamental building block of metal halide octahedra (BX_6), can also be assembled to possess other types of crystallographic structures. Using appropriate organic and inorganic components, low dimensional organic-inorganic metal halide hybrids with 2D, quasi-2D, corrugated-2D, 1D, and 0D structures at the molecular level have been developed and studied. Due to the strong quantum confinement and site isolation, these low dimensional metal halide hybrids at the molecular level exhibit remarkable and unique properties that are significantly different from those of ABX_3 perovskites. In light of the rapid development of low dimensional metal halide perovskites and hybrids, it is indeed timely to review the recent progress in these areas. Also, there is a need to clarify the difference between morphological low dimensional metal halide perovskites and molecular level low dimensional metal halide hybrids, as currently the terminologies of low dimensional perovskites are not appropriately used in many cases. In this review article, we discuss the synthesis, characterization, application, and computational studies of low dimensional metal halide perovskites and hybrids.

1. Introduction

The origin of "Perovskite" dates back to 1830s when calcium titanate ($CaTiO_3$) was first discovered by Gustav Rose and named in honor of Russian mineralogist L.A. Perovski. After that, the definition of perovskite has been extended to include compounds that have a similar crystal structure as that of $CaTiO_3$. Recently, metal halide perovskites have emerged as a highly promising class of functional materials for a variety of applications, including photovoltaic cells (PVs), light emitting diodes (LEDs), photodetectors, lasers, scintillators, etc. for their remarkable optical and electronic properties, as well as solution processibility. Metal halide perovskites adopt a chemical formula of ABX_3, where A and B stand for cations of different size and X represents halide anions. The first halide perovskites $CsPbX_3$ (X = Cl, Br, or I) were discovered in 1958 by Moller [1]. Later, organic metal halide perovskites were reported in 1978 to have methylammonium cation (MA) as A-site cation [2]. In addition to three-dimensional (3D) structure, layered two-dimensional (2D) perovskites containing < 100 > or < 110 > metal halide layers were investigated by Mitzi and coworkers in 1990s [3,4]. Their good carrier mobility and solution processibility enabled their applications in thin-film transistors and LEDs [4,5]. However, metal halide perovskites had not received much attention at that time due to the inferior device performance as compared to those based on organic and inorganic materials [6].

Miyasaka's pioneering work in 2009, using $MAPbBr_3$ and $MAPbI_3$ as light harvesting materials for sensitized PVs, renewed the research

* Corresponding author at: Department of Chemistry and Biochemistry, Florida State University, Tallahassee, Florida, 32306, United States.
E-mail address: bma@fsu.edu (B. Ma).

https://doi.org/10.1016/j.mser.2018.12.001
Received 23 October 2018; Accepted 3 December 2018
0927-796X/

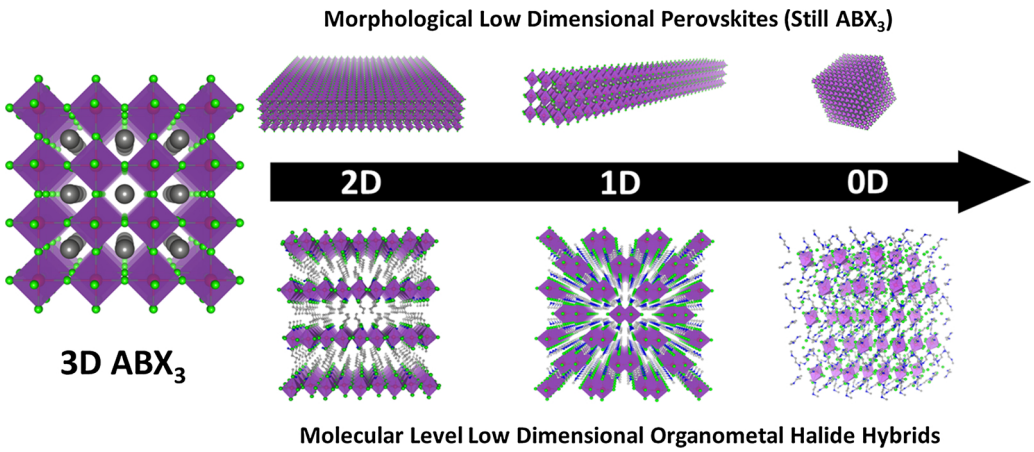

Fig. 1. 3D ABX_3 metal halide perovskites and perovskite-related materials with different dimensionalities at both morphological and molecular levels.

interest in metal halide perovskites [7]. Since then, the power conversion efficiencies (PCEs) of perovskite-based PVs have experienced unprecedented improvement from around 4% to more than 22% within 6 years. In addition to PV applications, the use of metal halide perovskites for room temperature electroluminescence devices has been demonstrated by Friend and coworkers in 2014 [8]. The rich chemistry of metal halide perovskites enables many ways of band structure control and color tuning by manipulating the composition and dimensionality. For instance, by controlling the halide compositions, the emission spectra of metal halide perovskites could be readily tuned to cover the entire visible spectral region [9–11]. Besides composition control, dimensionality control at both morphological and molecular levels has been demonstrated as an effective approach to manipulating the photophysical properties of this class of materials. In 2014, by using long alkyl chain as organic capping ligands, 6 nm-sized 0D $MAPbBr_3$ quantum dots were prepared by Pérez-Prieto and coworkers [12]. In the following year, colloidal 2D perovskite nanoplatelets were reported by Tyagi and coworkers to exhibit quantum confinement effects [13]. In the same year, atomically thin 2D perovskites were obtained by Yang group with efficient photoluminescence [14]. Uniform 1D ultrathin nanowires were also synthesized by the same group to show high photoluminescence quantum efficiencies (PLQEs) [15]. By choosing different combinations of organic acids and amines, the shape and dimensionality of metal halide perovskites can be facilely tuned to form 3D nanocubes, 2D nanoplatelets, 1D nanorods, and 0D quantum dots [16]. Apart from morphological dimensionality control, dimensionality control can also be achieved at the molecular level. For example, quasi-2D structures can be obtained by controlling the number of metal halide layers to achieve tunable band gap and photoluminescence. Layered 2D metal halide perovskites hold great promise to improve the stability of optoelectronic devices [17]. Besides 2D perovskites containing (100) flat sheets of metal halide octahedra, corrugated-2D organic-inorganic metal halide perovskites containing (110) crystallographic planes were found to have large structural distortion and strong exciton-lattice coupling with efficient exciton self-trapping [18]. Due to the formation of self-trapped excitons, broadband white emission with relatively high PLQE was achieved in a series of corrugated-2D structures [19–21]. Lowering the dimensionality further to 1D at the molecular level leads to stronger exciton self-trapping or structural distortion. For example, an efficient bluish white broadband emission was obtained in a 1D structure because of the stronger quantum confinement and exciton-lattice interaction. In an extreme case, with the individual metal halides completely separated from each other by the organic moieties, a true 0D structure at the molecular level can form with bulk crystals exhibiting intrinsic properties of individual metal halides [22]. As a result of the excited state reorganization of individual metal halides, strongly Stokes-shifted broadband emissions with PLQEs of up to near-unity were obtained for 0D organic metal halide hybrids.

Despite the tremendous achievements in metal halide perovskites and perovskite-related materials, the notions of “morphological” and “molecular level” low-dimensionalities are sometimes confused or misused by the research community. Therefore, we believe it is necessary to clarify the difference between these two types of materials. Morphological low-dimensional metal halide perovskites, including 2D nanoplatelets, 1D nanowires and nanorods, and 0D quantum dots [23], are nanoscale materials with quantum confinement in at least one direction. Intrinsically, they are still made up of corner-sharing metal halide octahedra and their crystallographic structures are indeed identical to that of bulk 3D metal halide perovskites. Therefore, in most cases, their chemical formulas can still be expressed by ABX_3 and their properties are derived from corresponding 3D ABX_3 perovskites with quantum confinement effects. Unlike morphological low dimensional materials, the properties of molecular level low-dimensional materials are independent of their crystal size. Inside the bulk crystals, the individual metal halide species (layers, wires, or polyhedrons) are isolated from each other by organic cations, enabling the bulk crystals to display the intrinsic properties of the individual building blocks. Fig. 1 shows the lowering of dimensionality from 3D to 2D, 1D, and 0D at both morphological and molecular levels to obtain new materials related to ABX_3 metal halide perovskites. In order to better distinguish the morphological and molecular level low dimensional materials, here we use the term of “low dimensional perovskites” for morphological nanoscale metal halide perovskites and “low dimensional metal halide hybrids” for bulk assemblies of low dimensional organic metal halide hybrids at the molecular level. In this review article, we discuss the research progresses on both low dimensional metal halide perovskites and hybrids.

2. Morphological low dimensional perovskites

2.1. 2D metal halide perovskites

Morphological 2D metal halide perovskites can be obtained by reducing the thickness of 3D ABX_3 perovskites to form 2D nanoplatelets, nanosheets, and nanodisks [24–26]. The extreme case of 2D metal halide perovskites are those containing only a single layer of corner-sharing metal halides. Due to the quantum confinement effect, the Coulombic force between electron and hole becomes stronger when the electron-hole pairs are confined in a 2D plane, which results in higher exciton binding energy with blue-shifted emission as compared to their 3D counterparts [27]. To prepare 2D metal halide perovskites, different methods have been developed, such as solution process method and vapor method. For example, Tyagi and coworkers used the colloidal method to synthesize 2D $MAPbBr_3$ nanoplatelets with nearly single unit

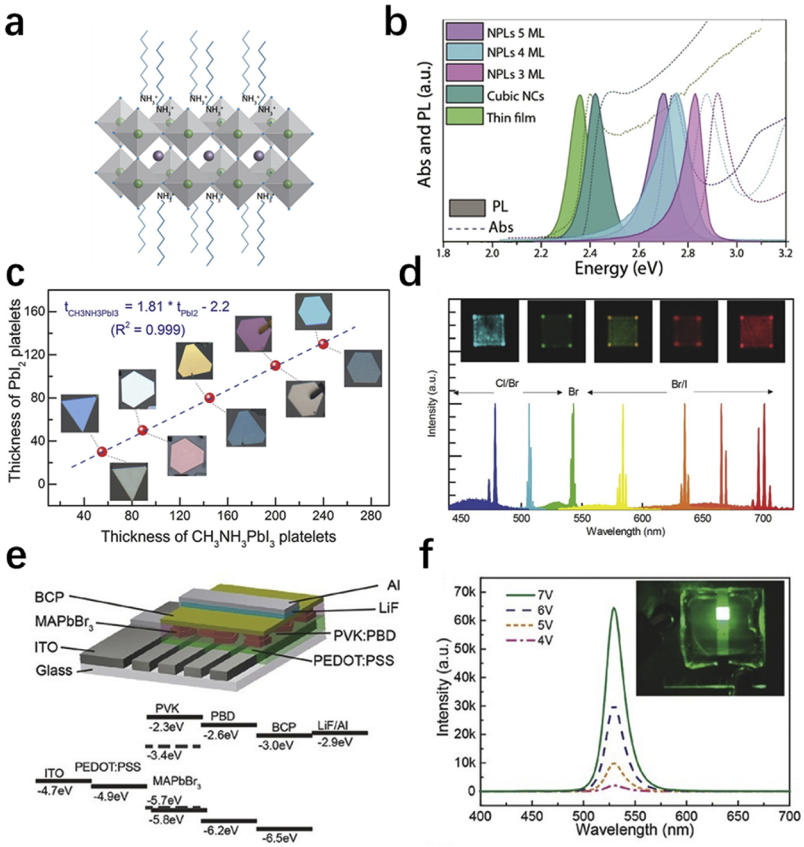

Fig. 2. (a) Schematic illustration of 2D perovskite nanoplatelets. Reprinted with permission from [13], Copyright 2015, American Chemical Society. (b) Absorption and PL spectra of $CsPbBr_3$ as a thin film, cube-shaped nanocrystals, and nanoplatelets of different thicknesses. Reprinted with permission from [28], Copyright 2016, American Chemical Society. (c) Lead halide perovskite nanoplatelets prepared via CVD method. The thickness of PbI_2 platelets before (images above data line) and after being converted to $MAPbI_3$ (images below data line). Note that the color of the PbI_2 platelets changed corresponding to the change in thickness (as measured by AFM). The thickness of the $MAPbI_3$ platelets was about 1.8 times higher compared to the corresponding PbI_2 platelets, which agrees well with the ratio of the c lattice constant between the two compounds. Reprinted with permission from [29]. (d) High-quality whispering-gallery-mode lasing from cesium lead halide perovskite nanoplatelets. Reprinted with permission from [31], Copyright 2016, Wiley-VCH. (e) Device architecture for a perovskite nanoplatelet based LED, and the flat-band energy level diagram of different layers of materials, showing conduction and valence band levels with respect to vacuum. (f) Electroluminescence spectrum from a standard device with PVK:PBD weight ratio of 64/36 at an applied voltage of 4–7 V. Inset: Photograph of a working device at 7 V. Reprinted with permission from [30], Copyright 2015, Wiley-VCH.

cell thickness and submicron lateral dimensions [13]. Manna and coworkers applied a room-temperature colloidal synthesis to prepare perovskite nanoplatelets with the thickness finely controlled between 3 to 5 layers [28]. Apart from solution-phase growth, chemical vapor deposition (CVD) approach was also investigated to prepare 2D perovskites. Xiong group reported the synthesis of lead halide perovskite nanoplatelets using a two-step CVD method (Fig. 2c) [29]. The nanoplatelets were synthesized on a muscovite mica using van der Waals epitaxial growth followed by a vapor-phase conversion. The unique properties of 2D metal halide perovskites have enabled a variety of applications, such as LEDs, lasers, and PVs [30–32]. (Fig. 2d-f). Ling and coworkers demonstrated bright LEDs based on perovskite nanoplatelets with high brightness of up to 10,590 cd m^{-2} [30]. Glovebox-free device fabrication was realized because of the high stability and moisture resistance of these organic-ligand capped perovskite nanoplatelets. The synthesis, properties, and applications of 2D metal halide perovskites have been well reviewed in several recent publications [33–36].

2.2. 1D metal halide perovskites

1D metal halide perovskites, such as nanowires and nanorods, have been reported to exhibit superior optical properties with long carrier diffusion length and lifetime [37–42]. To prepare single crystalline 1D perovskites, a number of methods have been developed, including vapor phase methods, solution phase methods, hot injection methods, and templated preparations [39,43–45]. Their applications in optoelectronic devices, including solar cells, photodetectors, waveguides, and nanolasers have been extensively explored [46,47]. In this session, we will highlight different methods for the synthesis of 1D perovskites and their application in optoelectronic devices.

2.2.1. Vapor phase methods

As an effective method of producing semiconductor nanowires, vapor phase synthesis has been employed for preparing 1D metal halide perovskites [48–50]. In 2014, Xiong and coworkers demonstrated the synthesis of $MAPbCl_3$ perovskite nanowires using vapor phase method, as illustrated in Fig. 3a [29]. In that work, $PbCl_2$ nanowires were grown on a mica substrate, followed by conversion into perovskite nanowires via the reaction with vapor-phase CH_3NH_3Cl molecules. However, 2D perovskite platelets were also produced as by-products during the formation of 1D nanowires. In order to improve the yield of perovskite nanowires, Xiong group replaced mica with the silicon oxide as substrates [51]. As a result, free-standing single-crystalline $MAPbI_3$, $MAPbBr_3$, and $MAPbI_xCl_{3-x}$ nanowires were obtained via a two-step vapor phase synthesis method (Fig. 3b-c). The vapor phase method was also used to prepare all-inorganic perovskites with higher stability [40,52–54]. Park and coworkers obtained the single-crystalline $CsPbX_3$ (X = Cl, Br, and I) perovskite nanowires using a vapor transport method, as shown in Fig. 3d [55]. The band gap of perovskite nanowires could be finely tuned over a wide range by controlling the composition ratio of the three halides. This method was also demonstrated by Joselevich and coworkers to produce high-quality $CsPbBr_3$ perovskite nanowires [56]. Interestingly, the obtained nanowires were grown almost exclusively horizontally and aligned on a sapphire substrate. More recently, Pan and coworkers synthesized high-quality in-plane aligned halide perovskite $CsPbX_3$ (X = Cl, Br, I) nanowires on an annealed sapphire substrate [57,58]. Composition-graded $CsPbBr_xI_{3-x}$ nanowires could also be synthesized using vapor phase synthesis based on the desynchronized deposition of metal halides and temperature controlled anion exchange reaction [54]. By increasing the Br/I ratio along with a single nanowire, the photoluminescence of these composition-graded nanowires changes at different positions from the center to the ends, enabling dual-color lasing under femtosecond laser excitation. Although great progress has been made in the synthesis of perovskite nanowires, vapor growth of high-quality perovskite nanorods were rarely reported [59–61]. An example to grow all-inorganic halide alloy perovskite nanorods via vapor phase deposition method

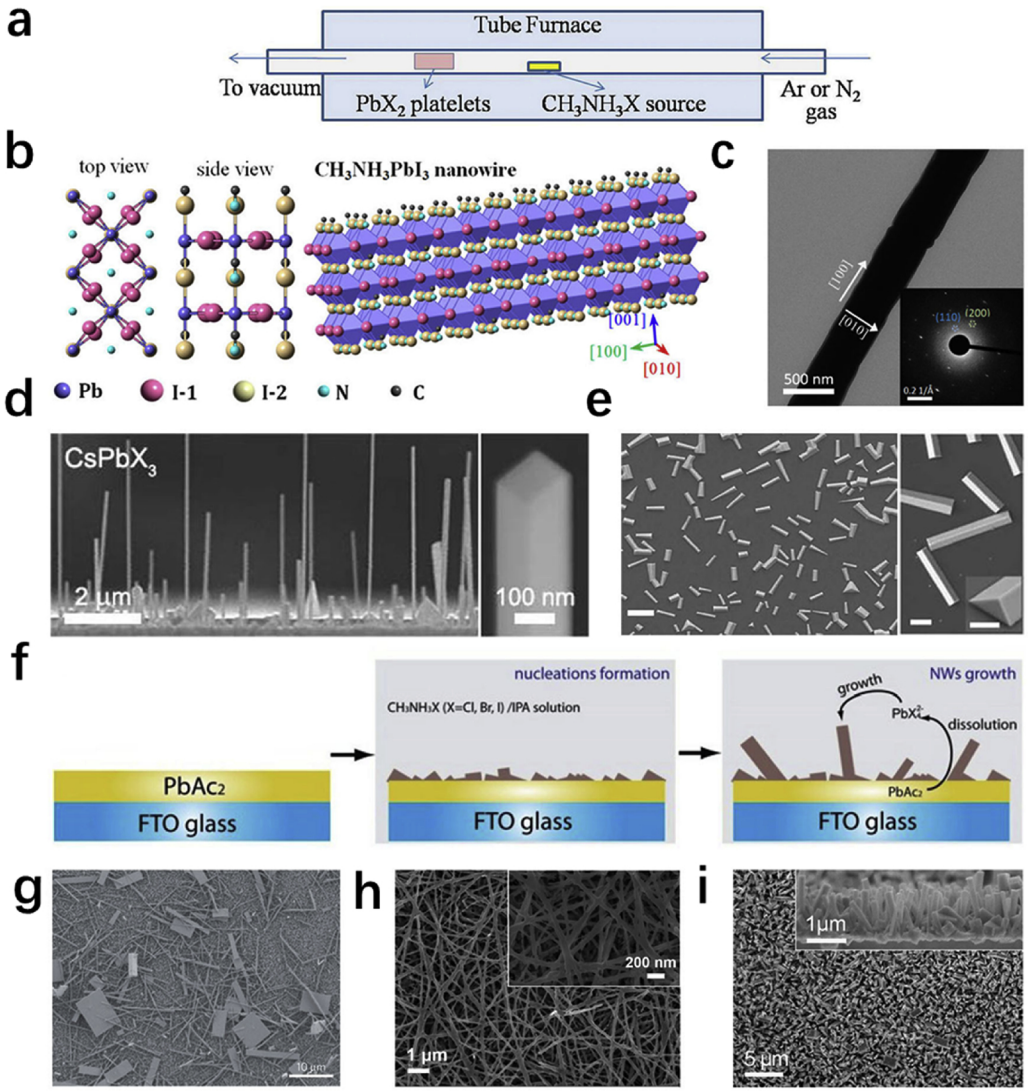

Fig. 3. (a) Schematic of the synthesis setup using a home-built vapor-transport system. Reprinted with permission from ref. [29], Copyright 2014, Wiley-VCH. (b) Structure simulation and (c) TEM images of $MAPbI_3$ nanowire. Insets in (c) is the corresponding SAED pattern. Reprinted with permission from ref. [51], Copyright 2015, American Chemical Society. (d) SEM images of vertically aligned $CsPbBr_3$ nanowires with a rectangular cross-section grown on a substrate. Reprinted with permission from ref. [55], Copyright 2016, American Chemical Society. (e) SEM images of $CsPbBr_3$ perovskite nanorods (scale bar, (left) 10 μm, (right) 1 μm). The inset is an enlarged tilt view of a perovskite nanorod, showing a triangular cross section and a smooth end facet (scale bar, 400 nm). Reprinted with permission from ref. [59] Copyright 2017, American Chemical Society. (f) Scheme illustrating the solution growth process of single-crystal lead halide perovskite $MAPbX_3$ (X = Cl, Br or I) nanowires. (g) SEM images of the obtained $MAPbI_3$ nanostructures. Reprinted with permission from ref. [62], Copyright 2015, Nature Publishing Group. (h) Plane-view SEM images of $MAPbI_3$ formed by a two-step spin coating method. Reprinted with permission from ref. [63], Copyright 2015, American Chemical Society. (i) Top view SEM image of $MAPbBr_3$ nanorod array. Inset shows cross-sectional view of $CH_3NH_3PbBr_3$ array. Reprinted with permission from ref. [64], Copyright 2015, American Chemical Society.

was demonstrated by Pan and coworkers [59]. In that work, the CsX and PbX_2 powders (molar ratio is 2:1) were firstly loaded in an alumina boat and put inside quartz tube mounted in a furnace. The reactants were then heated up to 570–600 °C and maintained for 15 min under the protection of Ar gas. As a result, $CsPbX_3$ (X = Cl, Br, and I) perovskite nanorods with the length of about 2–20 μm were achieved on the SiO_2/Si substrate (Fig. 3e).

2.2.2. Solution phase methods

Compared to the vapor phase methods, wet chemistry synthesis of metal halide perovskites has been found to be more cost-effective. Moreover, the as-prepared perovskite materials could be placed on different substrates [65–70]. In 2014, Horváth and coworkers reported the solution-phase synthesis of $MAPbI_3$ nanowires, which involved a low-temperature solution crystallization by a slip-coating process [44]. The width of obtained nanowires varied between 50 and 200 nm with lengths of up to 16 μm. These nanowires exhibit advantages over nanoparticles in terms of charge transport under illumination [71]. However, it is difficult to control the size of perovskite nanowires using this slip-coating method. In another important work performed by Zhu and coworkers, a $PbAc_2$ layer was spin-coated on a glass substrate and immersed in a CH_3NH_3X (X = Cl, Br, I or mixed halide precursor) solution at room temperature for about 20 h [62]. High-quality single-crystalline perovskite nanowires with lengths of up to 20 μm and flat rectangular end facets were attained (Fig. 3f–g). Based on the synthesis procedure, a dissolution-recrystallization growth mechanism was proposed. The key to preparing such high-quality nanowires is the low concentration of Pb precursor (PbI_4^{2-}) from the solid lead acetate film on the substrate that results in relatively slow release rate, and the optimized concentration of CH_3NH_3X precursor to maintain a low supersaturation condition. Following this work, a solution method without using surfactant ligand was reported to synthesize single-crystalline methylammonium lead halide perovskite nanowires and nanorods [72–77]. This method was further used for the preparation of formamidinium lead halide perovskite nanowires with enhanced thermal stability by Jin and coworkers [78]. Moreover, this solution synthesis method was investigated to prepare the all-inorganic $CsPbX_3$ (X = Cl, Br, I) perovskite nanowires by the same research group [79]. The single-crystalline $CsPbX_3$ nanowires were obtained with smooth end facets and subwavelength dimensions. Later, Park and coworkers developed a two-step spin coating procedure to prepare the uniform $MAPbI_3$ nanowires (Fig. 3h) [63]. The PbI_2 solution was firstly loaded on a TiO_2/FTO/glass substrate. Then the solution of CH_3NH_3I in isopropanol including 50 μL of dimethylformamide (DMF) was loaded on the PbI_2-coated substrate, in which the DMF played a key role in the formation of perovskite nanowires. Instead of forming nanocubic, the $MAPbI_3$ nanowire with the average diameter of 100 nm was formed by coating the PbI_2 layer with an isopropanol solution of CH_3NH_3I in the presence of DMF [80]. The crystal size tunability for $CH_3NH_3PbI_3$ nanowires were also demonstrated [42,81–84]. In 2015, Yang group

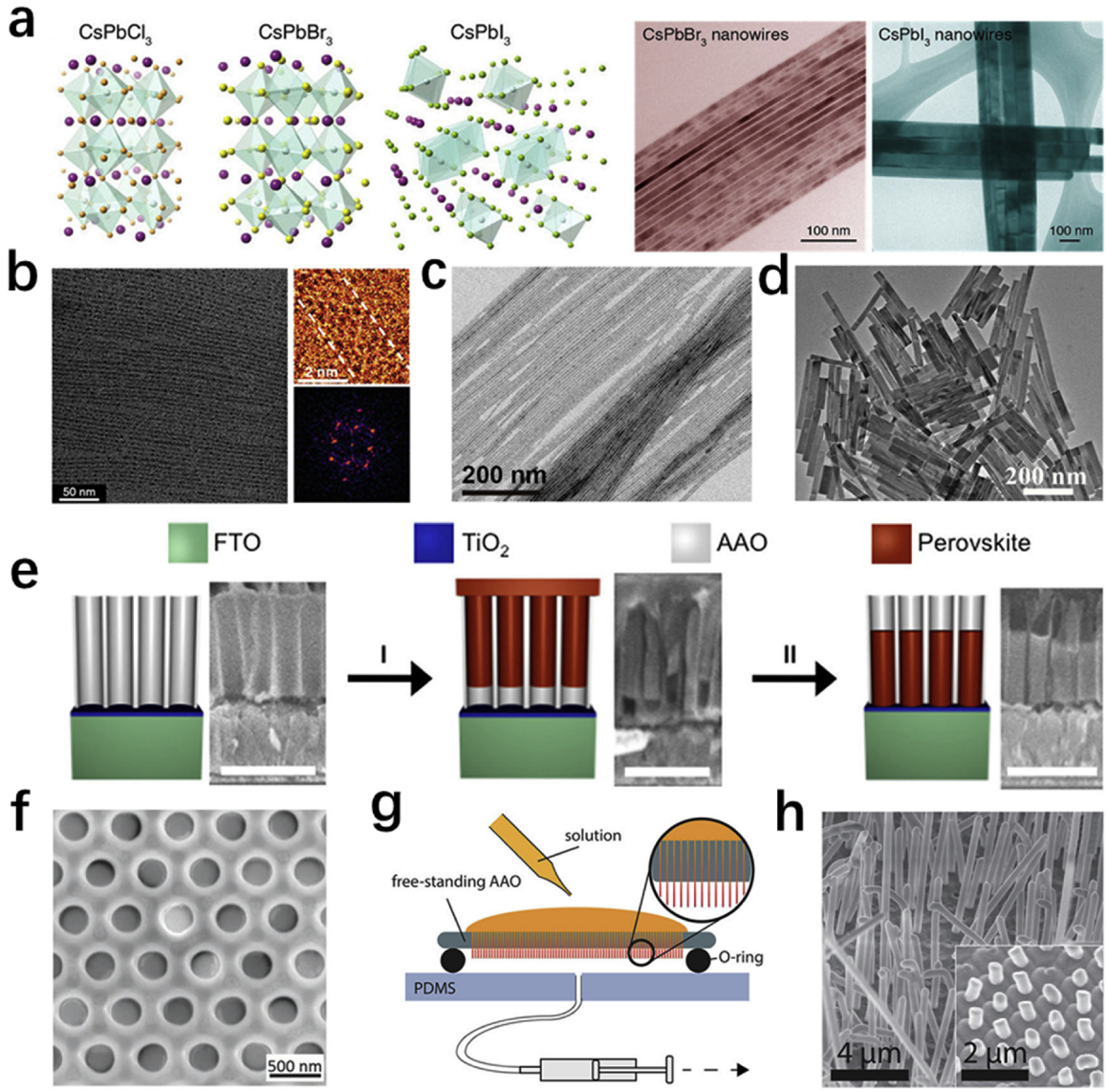

Fig. 4. (a) Schematic representations of three $CsPbX_3$ (X = Cl, Br, I) orthorhombic crystal structures. Cs, purple; Pb, blue. TEM images of $CsPbBr_3$ and $CsPbI_3$ nanowires. Reprinted with permission from "ref [45], [J. Am. Chem. Soc., 2016, 138, 7236-7239], Copyright 2015 & 2016, American Chemical Society. (b) TEM and aberration-corrected HRTEM images of $CsPbBr_3$ ultrathin nanowires. Reprinted with permission from ref. [87], Copyright 2016, American Chemical Society. (c) TEM image of the obtained $CsPbBr_3$ nanowires with the diameter of 5.1 nm. Reprinted with permission from ref. [88], Copyright 2016, American Chemical Society. (d) TEM image of the $CsSnI_3$ quantum rods. Reprinted with permission from ref. [94], Copyright 2016, American Chemical Society. (e) Synthesis procedure of perovskite nanowire array in AAO. $MAPbI_3$ precursor solution penetrates the AAO pores, followed by spin coating and annealing (I). The sample is exposed to a dimethyl sulfoxide/chlorobenzene solution followed by a short annealing step (II). Reprinted with permission from ref. [97], Copyright 2016, American Chemical Society. (f) Top view SEM image of $MAPbI_3$ nanowires in AAO after growth. Reprinted with permission from ref. [98], Copyright 2016, Wiley-VCH. (g) Extrusion scheme of the $MAPbBr_3$ perovskite nanowires. (h) SEM images of the obtained nanowires. The inset shows shorter nanowires that have been obtained by exposing the template for shorter times to the pressure gradient. Reprinted with permission from ref. [99], Copyright 2017, American Chemical Society. (For interpretation of the references to colour in this figure legend, the reader is referred to the web version of this article).

demonstrated solution phase growth of $MAPbX_3$ (X = Br, I) nanorod arrays at room temperature (Fig. 3i) [64]. In that work, a saturated methanolic solution of lead acetate was coated on a PEDOT:PSS/ITO/glass substrate by spin-coating. This substrate was then placed in a solution of CH_3NH_3Br in 2-propanol to form orange $MAPbBr_3$ nanorod arrays. The conversion of $MAPbBr_3$ to $MAPbI_3$ by anion exchange was achieved upon annealing at 140 to 150 °C in CH_3NH_3I vapor without the change of morphology. This solution synthesis method and anion exchange procedure for synthesizing 1D perovskite nanomaterials have been demonstrated to prepare the fully inorganic perovskite nanowires by the same group [85,86]. The obtained nanowires are single crystalline with well-formed facets. It is worth mentioning that these nanowires display excellent stability while stored and handled under ambient conditions over the course of weeks.

2.2.3. Hot-injection methods

Recently, hot-injection methods have been employed to synthesize all-inorganic halide perovskite nanowires. Synthesis of cesium lead halide nanowires using a hot injection approach was first reported in 2015 by Yang and coworkers (Fig. 4a) [45]. The cesium precursor was injected into PbX_2 (X = Br, I) solution in the presence of oleylamine and oleic acid ligands at 150–250 °C. Single-crystalline ultrathin $CsPbBr_3$ nanowires with a diameter of 2.2 ± 0.2 nm were also prepared by the same group using this approach (Fig. 4b) [87]. Afterward, hot injection methods were widely investigated to synthesize $CsPbX_3$ colloidal nanowires [88–93]. For instance, Imran and coworkers presented a

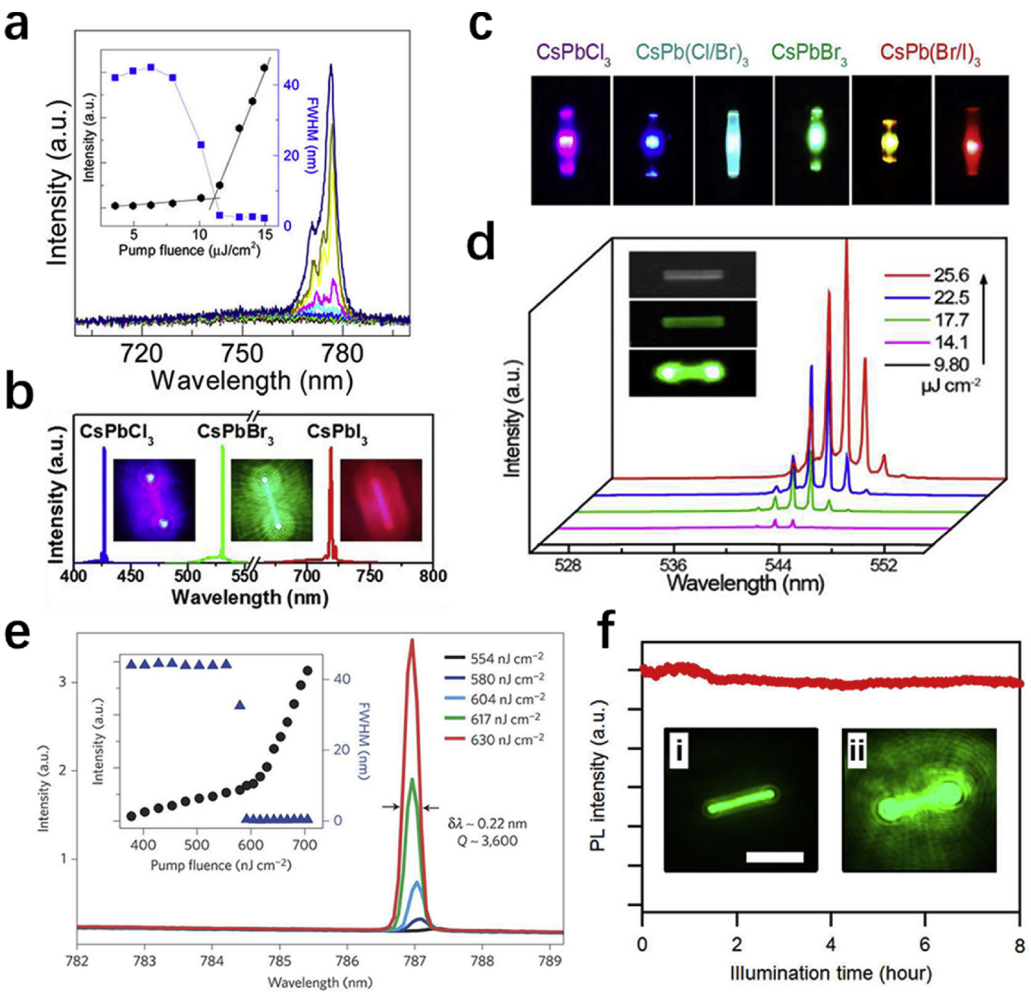

Fig. 5. (a) The evolution from spontaneous emission to lasing (Fabry-Pérot mode) in a typical $MAPbI_3$ nanowire. Reprinted with permission from ref. [51], Copyright 2015, American Chemical Society. (b) Wavelength tunability of the inorganic perovskite nanowire lasers. The inset shows the images of the emissions of the inorganic perovskite nanowire lasers. Reprinted with permission from ref. [55], Copyright 2016, American Chemical Society. (c) Real-color image of the band gap engineered triangular rod under local laser excitation. (d) Triangular rod emission spectra around the lasing threshold; inset: optical image (up) of a single triangular rod; the middle and bottom: images show the triangular micro/nanorod emission below and above P_{Th}, respectively. Reprinted with permission from ref. [59], Copyright 2017, American Chemical Society. (e) Nanowire emission spectra around the lasing threshold. Inset: Integrated emission intensity and the full width at half maximum (fwhm) as a function of *P* showing the lasing threshold at about 600 nJ cm^{-2}. The fwhm of the lasing peak ($\delta\lambda$) at 630 nJ cm^{-2} is 0.22 nm, corresponding to a *Q* factor about 3600. Reprinted with permission from ref. [62], Copyright 2015, Nature Publishing Group. (f) Integrated emission intensity of a nanowire laser as a function of pump time with up to 8 h of continuous illumination of 402 nm pulsed laser excitation (150 fs, 250 kHz) at room temperature. (i, ii) Fluorescence images of the nanowire below and above the lasing threshold, respectively. Scale bar is 10 μm. Reprinted with permission from ref. [79], Copyright 2016, American Chemical Society.

modified colloidal synthesis of $CsPbBr_3$ perovskite nanowires with a tunable nanowire width from 3.4 ± 0.5 nm to 20 ± 3 nm, by introducing carboxylic acids with short aliphatic chains (Fig. 4c) [88,89]. Besides the introduction of carboxylic acids, Amgar and coworkers found that the addition of hydrohalic acids (HX, X = Cl, Br, I) would strongly affect the perovskite nanowire length, composition, and optical properties [90]. The introduction of HCl or HI acids could influence the crystal structure and optical properties and shorten the nanowires, while the HBr addition only shortened the nanowires without any change on structure or optical properties. Hot-injection methods have also been reported to synthesize perovskite nanorods [94,95]. Liu and coworkers demonstrated a microwave-assisted technique to produce all-inorganic $CsPbBr_3$ nanorods within minutes by transferring Cs-oleate and $PbBr_2$ with the organic solvent (octadecene, oleic acid, and oleylamine) into the microwave oven to react with each other (Fig. 4d) [95]. The solvents, $PbBr_2$ precursors, and microwave powers all played important roles in the growth of the perovskite nanorods. By controlling the microwave powers and irradiation times, their sizes could be tailored as well. In the meantime, a hot-injection method was demonstrated to synthesize lead-free perovskites with lower toxicity [96]. A series of lead-free cesium tin halide perovskite quantum rods were produced by Chen and coworkers via a simple solvothermal process [94]. The as-prepared $CsSnX_3$ (X = Cl, Br, and I) quantum rods show composition dependent PL emissions over the visible spectral range varying from 625 to 709 nm.

2.2.4. *Template-assisted methods*

Synthesis of perovskite nanowires with well-defined shape and geometry using solution phase methods is not trivial due to the limited control of the nucleation process. To achieve a well-defined structure, one effective approach is to use templates, such as anodized aluminum oxide (AAO) templates with tuned, oriented, and cylindrical nanopores [39]. Recently, AAO template was used by Mirkin and coworkers to obtain uniform perovskite nanowires with diameters from 50 to 200 nm (Fig. 4e) [97]. A layer of TiO_2 was first deposited onto FTO glass and aluminum was then evaporated onto these substrates and anodized to form an AAO template. $MAPbI_3$ nanowires formed by adding $MAPbI_3$ DMF solution on the template followed by the removal of excess liquid. This template-assisted method does not require unique ligands or surface chemistries for preparing perovskite nanowires, which can be extended to synthesize a series of 1D perovskite materials with controlled diameters. As a result, large-area organometal halide perovskite ($MAPbI_3$ and $MAPbBr_3$) and all-inorganic perovskite (Cs_2SnI_6) nanowires can be synthesized. While the crystallinity, either single crystalline or polycrystalline, could not be fully confirmed for individual nanowires, the prepared of FTO/TiO_2/AAO/perovskites with high uniformity and aligned orientation could be used for the fabrication of nanowire-array solar cells; the device performance could be optimized by tuning the nanowire diameter, length, spacing, and composition. Fan and coworkers demonstrated a vapor-solid-solid reaction process to grow ordered $MAPbI_3$ nanowire arrays in AAO template (Fig. 4f) [98]. The Pb nanoclusters were deposited at a bottom of the free-standing

AAO template (2 μm-thick) to initiate $MAPbI_3$ nanowire growth, in which the Pb is not a catalyst but a reactant. The reaction between Pb and CH_3NH_3I vapor produced $MAPbI_3$ nanowires with precisely engineered geometry. An ultrahigh nanowire density in the range of 4×10^8-10^9 cm^{-2} can be achieved in these ordered nanowire arrays at a sizable scale of about 9 cm^2. This approach was also applied to synthesize lead-free perovskite $MASnI_3$ and all-inorganic halide perovskite $CsPbI_3$ nanowires, revealing the universality of this template-assisted method [100,101]. However, the template, which plays a crucial role in achieving well-defined shape and geometry, cannot be selectively removed due to the vulnerability of perovskites to etchants. Also, the geometries of nanowires are limited by the structure of their templates [99]. In this regard, Fan and coworkers introduced a modified template-assisted method to fabricate free-standing solution-based vertical nanowires. An AAO template was used to confine the precursor solution in highly ordered nanopores, as shown in Fig. 4g. The precursor was then extruded from the AAO templates induced by a small pressure gradient. As a result, highly uniform free-standing perovskite nanowires with a wide variety of dimensions were obtained after thermal annealing (Fig. 4h). More importantly, by tuning the pore size of templates, the size distribution of high-quality perovskite nanowires can be well manipulated.

2.2.5. Application of 1D metal halide perovskites

1D metal halide perovskites have been used to fabricate many optoelectronic devices due to their great optoelectronic properties [55,63,68]. 1D perovskite nanowires are excellent candidates for use in optically pumped lasers owing to their great optical properties and strong isotropy. For instance, a $MAPbI_3$ nanowire-based nanolaser was reported by Xiong and coworkers to exhibit 777 nm near-infrared light with a low threshold of 11 μJ cm^{-2} and a quality factor as high as 405 (Fig. 5a) [51]. The color tunability of perovskite nanowire lasers was demonstrated by Park et al. in $CsPbX_3$ (X = Cl, Br, and I) metal halide perovskites [55]. The emission color of nanowires was tuned over a wide range, from deep blue to green and red, by changing the halide compositions (Fig. 5b). Later, Pan group further realized complete composition and emission color tuning of cesium lead halide perovskite lasing with low lasing thresholds (about 14.1 μJ cm^{-2}) and high *Q* factors (about 3500) (Fig. 5c-d) [59]. Remarkably, Zhu and his colleagues used high quality single-crystalline perovskite nanowires to achieve a wavelength-tunable lasing with very low lasing thresholds (220 nJ cm^{-2}) and high-quality factors about 3600 [62]. The high lasing quantum yields of up to 100%, are attributed to the little-to-no charge carrier trapping in these single-crystalline nanowires (Fig. 5e). The stability of these all-inorganic $CsPbX_3$ (X = Cl, Br, I) was explored by Jin and coworkers. The lasing emission exhibited no measurable degradation after 8 h or 7.2×10^9 laser shots under continuous illumination [79] (Fig. 5f). It has been shown that these Cs-based perovskite nanowires could be an excellent platform for tunable nanowire lasers and other nanoscale optoelectronic devices.

Apart from optically pumped lasers, the $MAPbI_3$ nanowires were also used as the light absorption layer in perovskite solar cells (Fig. 6a) [63]. Time-resolved fluorescence spectroscopy indicated that charge separation at the interface between hole transport and perovskite layers is faster if the perovskite layer consists of 1D nanowires. As reported in 2015, the best performing device based on $MAPbI_3$ nanowires showed photocurrent density of 19.12 mA, cm^{-2} the voltage of 1.052 V, and fill factor of 0.721, leading to a PCE of 14.71% at standard AM 1.5 G solar illumination. Since then, $MAPbI_3$ nanowires with various size have been prepared, and a series of perovskite solar cells based on $MAPbI_3$ nanowires have been fabricated [82–84]. With the optimized fabrication of perovskite solar cells, a remarkable PCE of up to 18.83% was achieved, among the highest PCEs ever reported for perovskite nanowire solar cells [82]. In 2016, Chen and coworkers achieved a PCE of 12.96% under AM 1.5 G by using a lead-free $CsSnI_3$ quantum rod absorber layer (9.66% for $CsSnCl_3$, 10.46% for $CsSnBr_3$) (Fig. 6b) [94]. 1D perovskite nanowires have also been used to fabricate LEDs and sensors. For example, Yang and coworkers demonstrated LEDs based on $MAPbX_3$ (X = Br, I) nanorod arrays (Fig. 6c, d) [64]. The $MAPbBr_3$ nanorod-based LED exhibits green electroluminescence at 533 nm with a small fwhm of 26 nm. Fan and colleagues fabricated image sensors consisting of 1024 nanowire photodiodes pixels; the imaging functionality was verified by recognizing some optical patterns projected on the sensor (Fig. 6e, f) [98]. This suggests the great potential of unique nanowire arrays as high-resolution image sensors since the diameter of each nanowire sensor pixel can be as small as hundreds of nanometers.

2.3. 0D perovskite nanocrystals

0D nanocrystals (NCs) or quantum dots (QDs) with all three dimensions in the nanoscale range often exhibit enhanced optical and electronic proprieties over their bulk counterparts, due to large surface to volume ratio, strong quantum confinement effect, and anisotropic geometry. Metal halide perovskites in the form of 0D nanocrystals have attracted great research attention, for their facile synthesis, high PLQEs, property tunability, and enhanced stability. To date, a variety of approaches have been demonstrated to prepare perovskite QDs, including ligand-assisted reprecipitation (LARP), hot-injection, *in-situ* preparation, and template-assisted methods. Their remarkable optical and electronic properties enable their applications in PVs, LEDs, lasers, photodetectors, etc.

2.3.1. Ligand-assisted re-precipitation methods

In 2014, Perez-Prieto and colleagues demonstrated that nanometer-sized $MAPbBr_3$ could be facilely synthesized via reacting the mixture of CH_3NH_3Br and medium/long chain alkyl ammonium bromide with $PbBr_2$ in the presence of oleic acid and octadecene at room temperature, as illustrated in Fig. 7a [102]. Optimizing the molar ratio of reactants, perovskite NCs with high PLQEs have been obtained by the same group. This synthetic approach was subsequently adopted and improved by several groups [10,103]. For instance, by incorporating *n*-octylamine and oleic acid as ligands into the reprecipitation process, Zhong and coworkers produced colloidal $MAPbBr_3$ QDs with an average diameter of 3.3 nm and absolute PLQEs of up to 70% [10]. Zeng and co-workers reported a ligand-assisted re-precipitation method for the preparation of high-quality $CsPbX_3$ NCs, where precursors were dissolved in a polar solvent and then injected into a nonpolar solvent, resulting in rapid nucleation and crystal growth [103]. Pan group developed a novel homogeneous approach to prepare highly luminescent $CsPbX_3$ NCs in a variety of nonpolar organic solvents [104]. Cesium and lead fatty acid salts, as well as quaternary ammonium bromides, were used as the precursors. The as-prepared $CsPbX_3$ (X = Cl, Br, or I) perovskite QDs exhibit highly efficient photoluminescence with the tunable emission wavelength from 440 nm to 682 nm and high PLQEs of 50–85 %.

2.3.2. Hot-injection methods

Motivated by the success of the organic-inorganic hybrid perovskites, all-inorganic cesium lead halide ($CsPbX_3$, X = Cl, Br, or I) NCs were first reported by Kovalenko and coworkers in 2015 [9]. The crystallization of $CsPbX_3$ NCs was achieved by the swift injection of cesium oleate into an octadecene solution containing PbX_2, oleic acid (OA), and oleylamine (OAm) at high temperatures (140–200 °C) as shown in Fig. 7b. In the synthesis, long-chain organic ligands OAm and OA were employed to solubilize PbX_2 and stabilize the perovskite NCs. Due to the fast nucleation and growth kinetics, the majority of the crystal growth process completed within the first 3 s after the injection of Cs-oleate. The bandgap energy and emission of colloidal $CsPbX_3$ NCs can be readily tuned by modulating their composition and crystal size. Interestingly, the size of these NCs can be controlled by changing the reaction temperature.

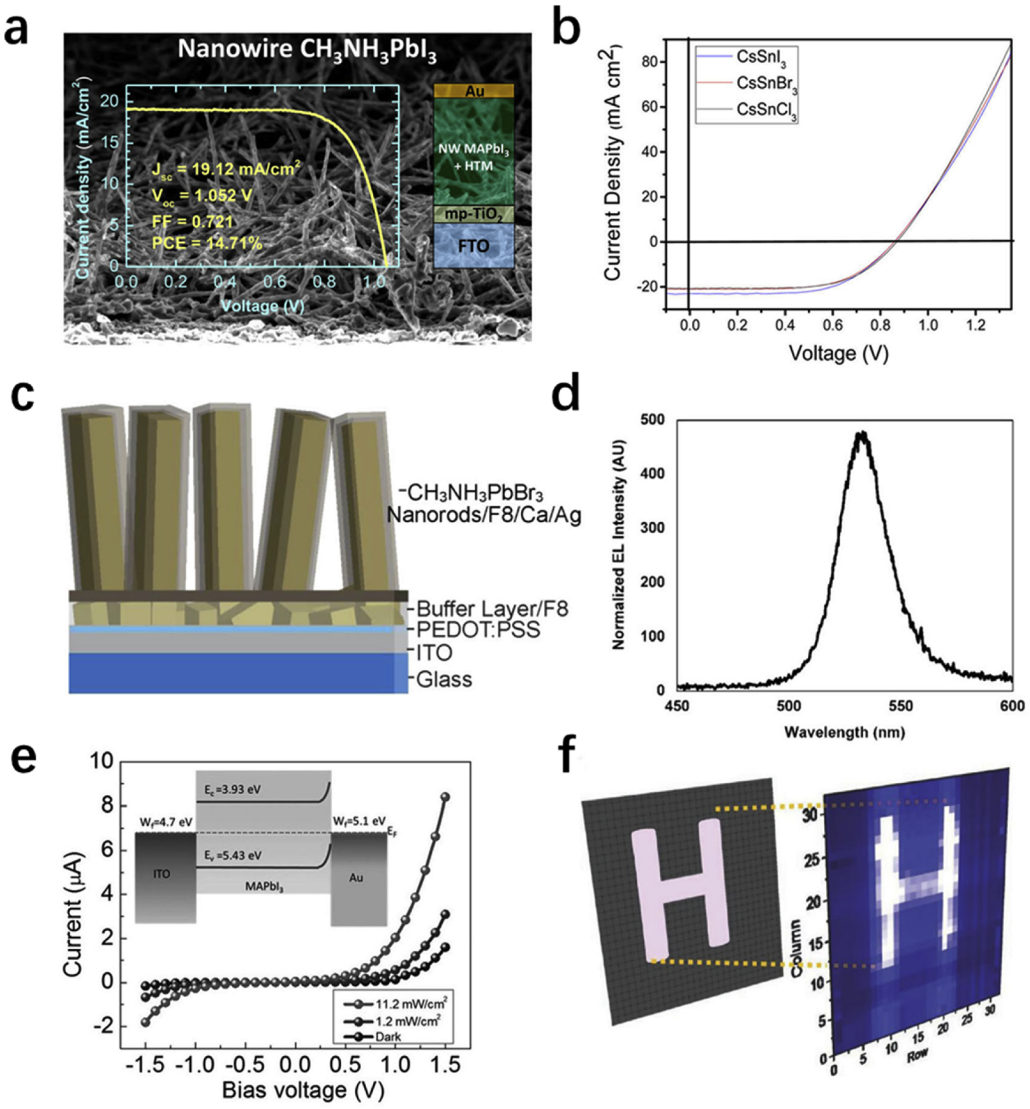

Fig. 6. (a) Device structure and current-voltage curve measured at AM 1.5 G illumination of perovskite solar cell based on $MAPbI_3$ nanowires. Reprinted with permission from ref. [63], Copyright 2015, American Chemical Society. (b) Current-voltage characteristics of $CsSnI_3$ (blue), $CsSnBr_3$ (red), and $CsSnCl_3$ (black) solar cells. Reprinted with permission from ref. [94], Copyright 2016, American Chemical Society. (c) The device structure of a $MAPbBr_3$ nanorod array LED. (d) Electroluminescence spectrum from the hybrid perovskite nanorod array LED. Reprinted with permission from ref. [64], Copyright 2015, American Chemical Society. (e) I–V curves under different illumination intensity (white color light). Inset: band structure of a single-pixel device under zero bias and in the dark. (f) Original and imaged letter ("H"). Reprinted with permission from ref. [98], Copyright 2016, Wiley-VCH (For interpretation of the references to colour in this figure legend, the reader is referred to the web version of this article).

2.3.3. *In-situ preparation methods*

One of the drawbacks for wet chemistry prepared perovskite NCs is the use of long insulating organic ligands as surface capping agents that would negatively impact the electronic properties and thin film formation. Recently, *in situ* formations of perovskite NC thin film contained thin films has been reported as an alternative to address these issues [105,107–110]. In general, bulky organic molecules were introduced to the precursor solutions to confine crystal growth of perovskite during film formation by solution processing. Zhong and colleagues applied *in-situ* fabrication strategy to prepare $MAPbX_3$ NCs embedded in polyvinylidene fluoride (PVDF) matrix by separating the crystallization processes of PVDF and $MAPbX_3$ (Fig. 7c) [105]. The composite films showed enhanced photoluminescence with PLQE of up to 95% and improved stability against moisture and UV-radiation. Later, the use of bulky organic ammonium halide was investigated by Rand and coworkers [107,108]. Large *n*-butylammonium halide was added to the perovskite precursor solution as a surfactant that dramatically constrains the growth of 3D perovskite grains during the film formation with the grain size of as small as 10 nm and film roughness of less than 1 nm. The 4-flurophenylmethylammonium iodide and phenethyl ammonium bromide were used as additives to confine the crystal growth of $MAPbI_3$ and $MAPbBr_3$ and form the corresponding nanocrystalline films. The additive-confined NCs exhibited enormously enhanced photoluminescence properties with a high PLQE and a long decay lifetime. The LED device performance based on this NC film showed significant improvement over the control device that was fabricated without the additives. Moreover, many other organic molecules besides *n*-butylammonium halides [108], e.g. methylammonium bromide [109], and poly(methyl methacrylate) (PMMA) [110], have been explored for *in-situ* preparations of perovskite NCs.

2.3.4. *Template-assisted methods*

Another strategy to fabricate perovskite QDs is utilizing mesoporous templates, such as aluminium oxide [111,112] and silica [106,113]. This method was first used to synthesize lead bromide perovskite by Miyasaka and colleagues in 2012 [111]. The DMF precursor solution comprising stoichiometric CH_3NH_3Br and $PbBr_2$ was spin-coated on the moderately heated porous Al_2O_3 film (< 50 °C). Nanocrystalline lead bromide perovskite was obtained by rapid self-organization on a mesoporous aluminum oxide film. However, quantitative estimation of the PLQE was not reported at that time. In 2015, Bolink and coworkers presented a new approach to preparing high-PLQE perovskite NCs by mixing CH_3NH_3Br and $PbBr_2$ with Al_2O_3 NCs and then spin-coating them onto glass or quartz substrate in the ambient condition followed by thermal annealing [112]. The nanocrystal dimensions are governed by the size and concentration of the alumina nanoparticles. In addition to the Al_2O_3 nanoparticle, mesoporous silica has been used as templates to prepare perovskite NCs by simply dipping the mesoporous silica in a

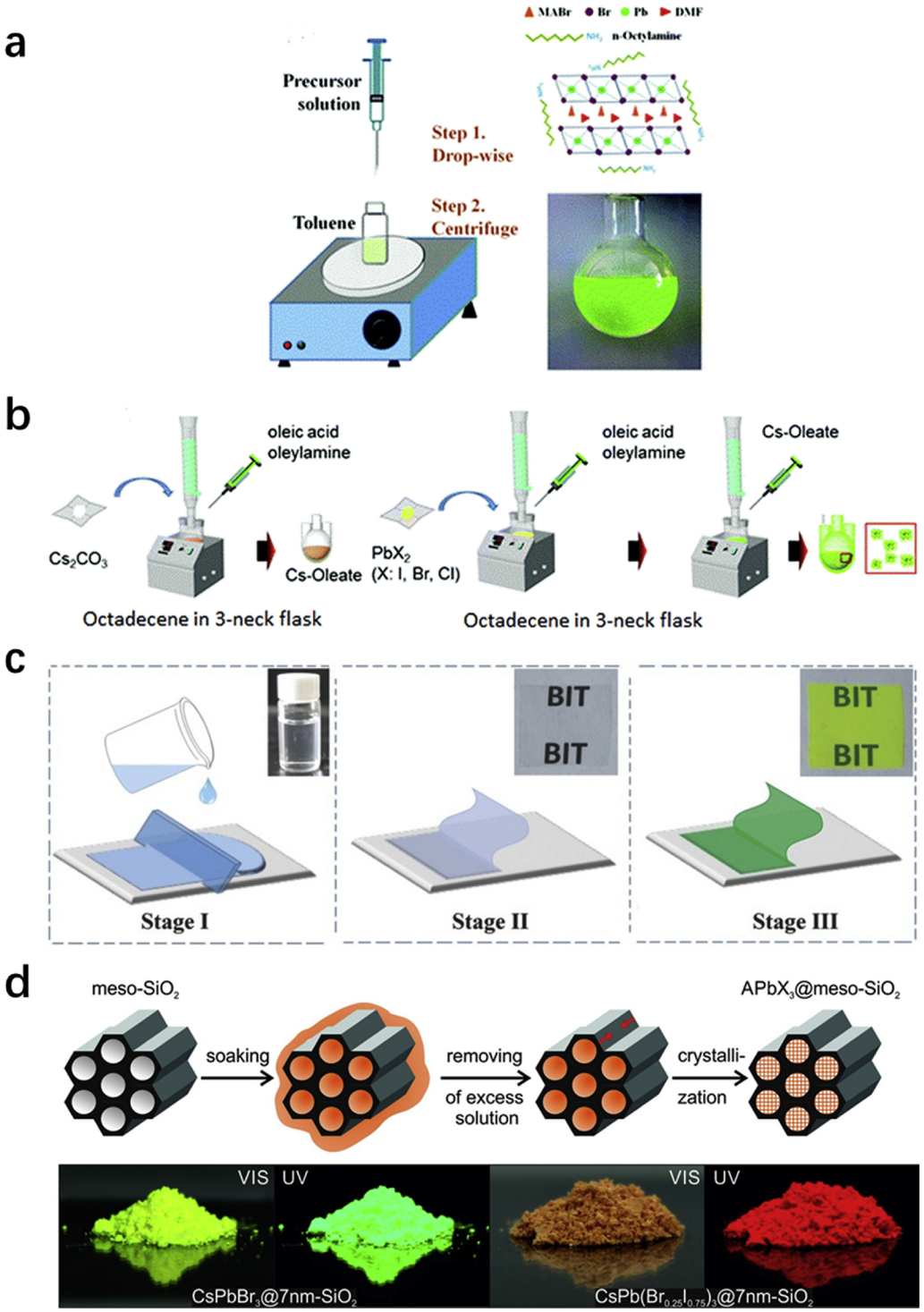

Fig. 7. Schematic illustration of the synthesis of perovskite quantum dots via (a) ligand-assisted re-precipitation method. Reprinted with permission from ref. [10] Copyright 2015, American Chemical Society. (b) hot-injection method. Reprinted with permission from ref [9]. Copyright 2015, American Chemical Society. (c) *in-situ* preparation method. Reprinted with permission from ref. [105] Copyright 2016, Wiley-VCH (d) template-assisted method. Reprinted with permission from ref [106]. Copyright 2016, American Chemical Society.

perovskite precursor (Fig. 7d) [106]. This facile, complementary, non-colloidal, and ligand-free preparation route yields templated NCs that exhibit an unprecedented high-quality emission owing to the intrinsic tolerance of the electronic structure to the defects in these materials.

2.3.5. Applications of perovskite QDs

Perovskites QDs show great potential in making solar cells owing to their unique optoelectronic properties. Park group demonstrated perovskite QD sensitized solar cells in 2011 with a PCE of 6.54%, a record value at the time for perovskite QD-sensitized solar cells [114]. After that, $CsPbI_3$ QDs with a cubic phase were widely employed to fabricate solar cells because of their broad absorption and appropriate bandgap (E_g = 1.73 eV) [115,116]. However, the α-$CsPbI_3$ with cubic phase can be immediately transformed into an orthorhombic phase when exposed to the ambient condition as the α-$CsPbI_3$ is merely stable at high temperature. With the partial substitution of I by Br, mixed

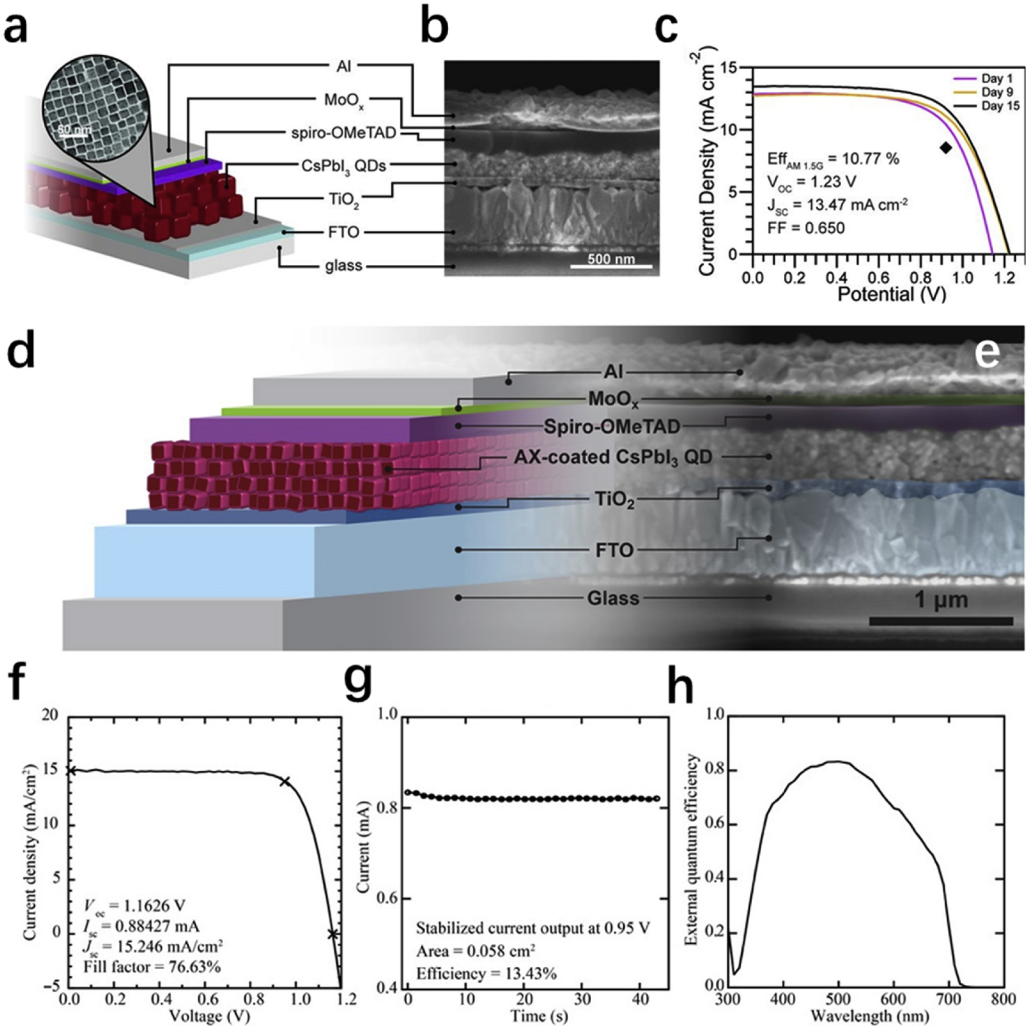

Fig. 8. (a) QD-sensitized solar cell architecture based on $CsPbI_3$ (Inset: TEM image of QDs). (b) SEM cross-section of $CsPbI_3$ PV cell. (c) Current density-voltage curves of a device measured in the air over the course of 15 days. Reprinted with permission from ref. [119] Copyright 2016, AAAS. (d) Schematic cross-section of a solar cell. FTO, fluorine-doped tin oxide. (e) SEM image of a device cross section. NREL-certified (f) *J-V* characteristics from forward bias to reverse bias, (g) stabilized current at a constant voltage of 0.95 V, and (h) EQE. Reprinted with permission from ref. [120] Copyright 2017, AAAS.

halide perovskite $CsPbBrI_2$ has also been attempted. Although this approach can stabilize the cubic phase, the resulting increase in band gap is undesired [117,118]. To avoid this, Luther group demonstrated a new strategy to stabilize α-$CsPbI_3$ at room temperature by purifying $CsPbI_3$ QDs [119]. An air-stable, highly efficient perovskite QD solar cell with a PCE of > 10% has been achieved by controlling the electronic coupling of QDs through purification of QDs with anti-solvent methyl acetate. The device structure and characteristics are shown in Fig. 8a–c. Thereafter, the same group demonstrated the certified record solar cell efficiency of 13.43% based on the $CsPbI_3$ QDs (Fig. 8d-h) with improved mobility and photocurrent by employing the A-site cation halide salt treatments [120].

The high exciton binding energy, strong photoluminescence, high color purity and tunable bandgaps exhibited by halide perovskite QDs make them highly attractive for LEDs. The all-inorganic halide perovskite QDs were first used as emitters in LED by Zeng group [121]. The LARP method was adopted to prepare perovskite QDs with a high PLQE. Blue, green and yellow QLEDs were realized by tuning the halide composition (Fig. 9a–c). However, the luminance and external quantum efficiency (EQE) were extremely low, which could be attributed to: i) dramatic decrease of PLQEs in thin films; ii) excessive insulating ligands that inhibited the charge transport; iii) surface-defect-induced non-radiative recombination. Later, the same group demonstrated a remarkable improvement of the EQE from 0.12% to 6.27% by carefully balancing the surface passivation and carrier injection through controlling the ligand density with the mixed solvents hexane/ethyl acetate [122]. The comparison of device performance with different solvents optimization was shown in Fig. 9d-e. Some other strategies have also been developed to improve the device performance of LEDs based on perovskite QDs, such as surface engineering [123,124] and device structure optimization [125,126]. However, the organic capping ligands used in these methods for stabilizing perovskite QDs have the detrimental effect of suppressing charge injection into emitters; thereby, resulting in low brightness and high turn-on voltage. To address this issue, *in-situ* perovskite QDs film preparation method has been used to fabricate QDs film, which exhibited enhanced PLQE and longer decay lifetime [107]. The $MAPbI_3$ and $MAPbBr_3$ LEDs made from these films showed a peak EQE of 7.9% and 7%, respectively (Fig. 9f-i). Simultaneously, Park group also reported *in-situ* formed nanocrystalline films for highly efficient LEDs [109]. The highly luminescent nanocrystalline $MAPbBr_3$ film was achieved with excess MABr that inhibits the growth of $MAPbBr_3$ followed by a non-thermal solvent-vacuum drying approach. As a result, highly efficient perovskite LEDs with maximum EQE of 8.21% and current efficiency of 34.46 cd/A were achieved.

Perovskite thin films were demonstrated to exhibit amplified

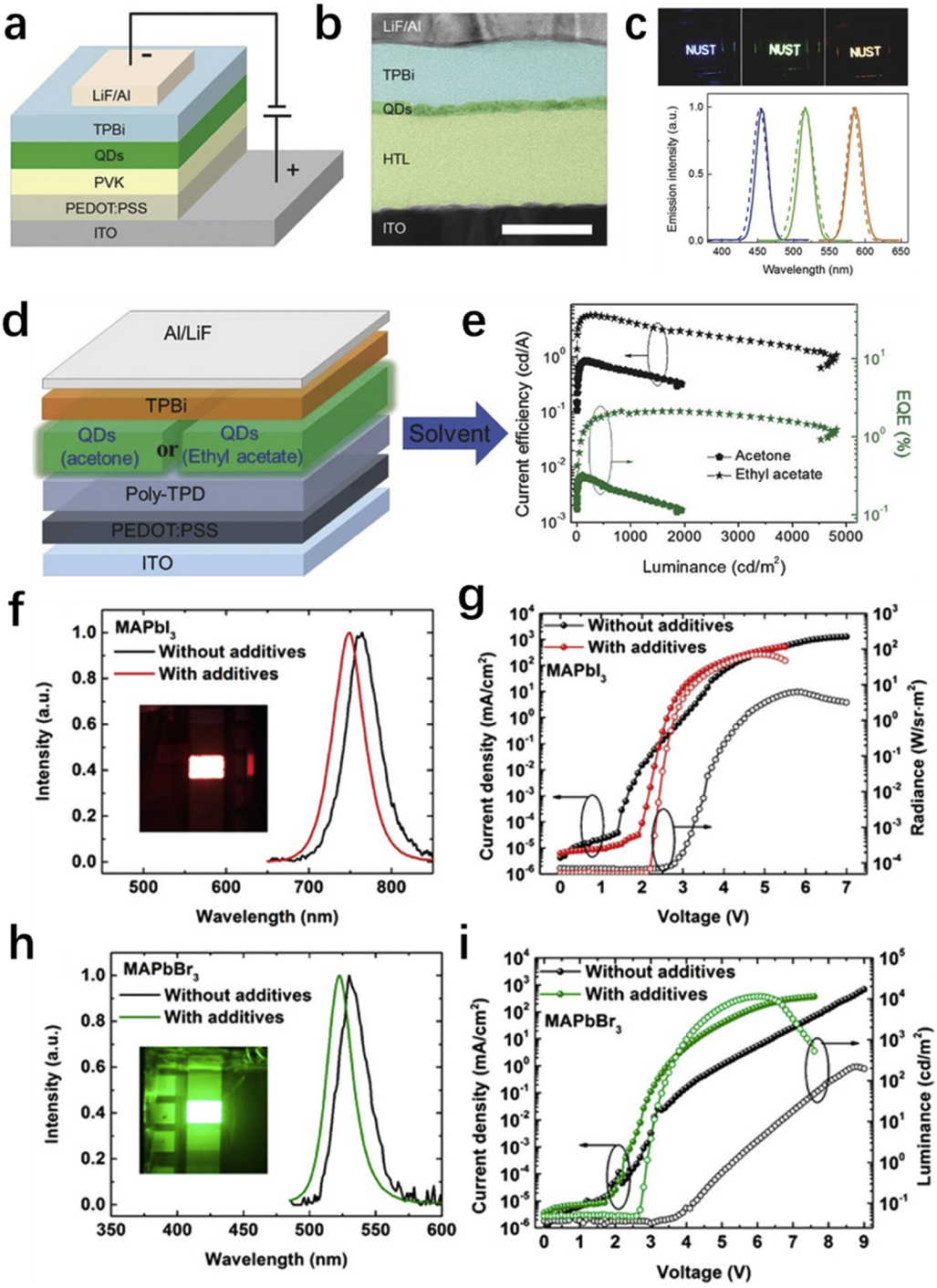

Fig. 9. (a) Device structure of the perovskite QLED devices. (b) Cross-sectional TEM image of the QLED. (c) Photographs of QLED devices with the Nanjing University of Science and Technology (NUST) logo. (top) The EL spectra (straight line) of the sample shown in top photos under an applied voltage of 5.5 V and the PL spectra (dashed line) of QDs dispersed in hexane. (bottom) Reprinted with permission from ref. [121] Copyright 2015, Wiley-VCH. (d) Schematic illustration of a device for purifying solvent optimization. (e) corresponding comparison of current efficiency and EQE. Reprinted with permission from ref [122]. Copyright 2017, Wiley-VCH. (f) EL spectra, (g) J-R-V curves of $MAPbI_3$ red LEDs with and without fluorophenylmethylammonium iodide additives. (h) EL spectra, (i) J-L-V curves of $MAPbBr_3$ LEDs with and without phenethylammonium bromide additives. Reprinted with permission from ref. [107] Copyright 2017, American Chemical Society. (For interpretation of the references to colour in this figure legend, the reader is referred to the web version of this article).

spontaneous emission (ASE) in 2014 [127]. However, intrinsic crystalline defects and strong self-absorption of bulk perovskite films resulted in low quantum efficiency that limits the gain of media. By virtue of high PLQE and tunable emission, perovskite QDs show promise in fabricating high-performance lasers. In 2015, Kovalanko group demonstrated low-threshold amplified spontaneous lasing from colloidal NCs of $CsPbBr_3$ [128]. A room-temperature optical amplification was realized that covered the entire visible spectral range (400–700 nm) with low pump thresholds down to 5 μJ cm^{-2} and high value of the modal net gain of at least 450 cm^{-1}, as shown in Fig. 10a-d. Moreover, the laser was successfully observed in whispering-gallery-mode and random mode. Sun and Zeng discovered that the $CsPbX_3$ QDs possess superior optical gain properties such as low-threshold, high-stability, and wavelength-tunable [53]. The same groups then demonstrated nonlinear absorption and low-threshold multiphoton (two-photon and three-photon) pumped stimulated emission from these inorganic perovskite QDs (Fig. 10e-f) [129]. To enhance their inherent stability, Pan and coworkers developed a passivation strategy by introducing an inorganic-organic hybrid ion pair as the capping ligand to achieve higher air- and photo-stability [130]. The resulting QDs exhibited ultra-stable ASE by one- (1 PA) and two-photon absorption (2 PA) process as shown in Fig. 10g-h. The corresponding QDs film showed good photostability under continuous pulsed laser excitation in ambient conditions for at least 34 h.

Lee and coworkers reported perovskite QDs-based photodetectors by using the halide exchange reaction to prepare the chloride-substitute

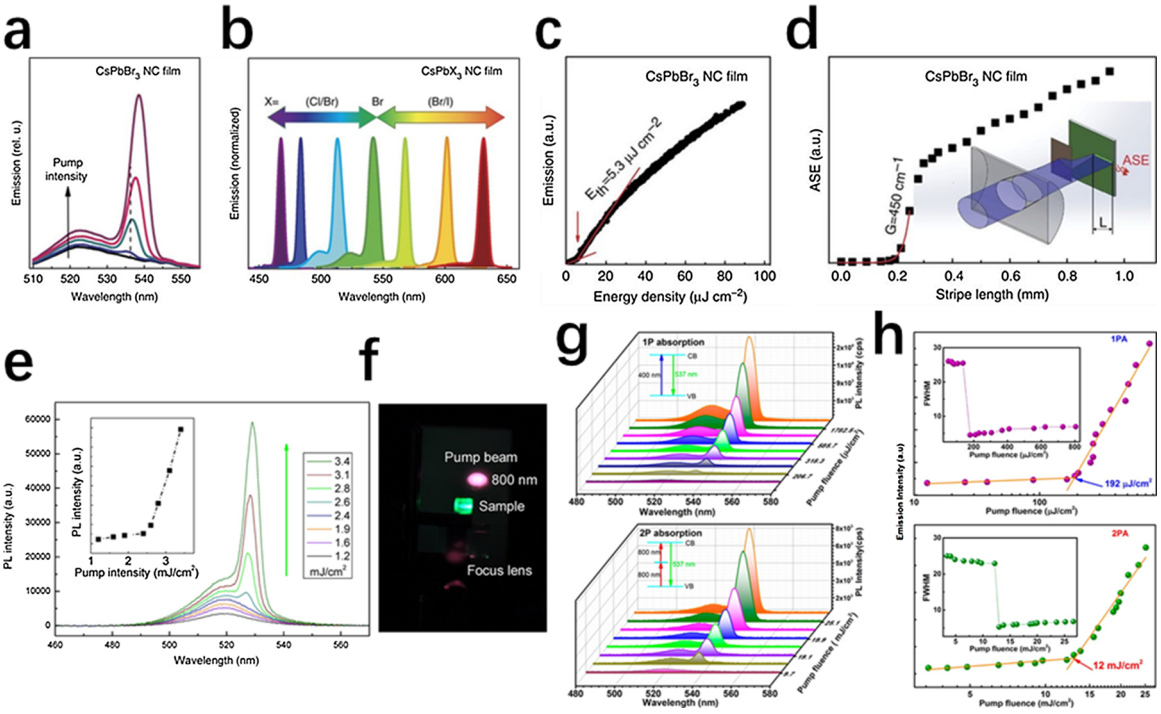

Fig. 10. (a) Pump-fluence dependence of the emission from a $CsPbBr_3$ NC film. (b) The spectral tunability of ASE via compositional modulation. (c) Threshold behavior for the intensity of the ASE band of the $CsPbBr_3$NC film. (d) Variable stripe-length experiment for an estimate of modal net gain for the $CsPbBr_3$ NC film. Reprinted with permission from ref. [128] Copyright 2015, Nature Publishing Group (e) Pump intensity dependent frequency-upconverted PL spectra from a thin film of $CsPbBr_3$ nanocrystal excited at 800 nm. (f) Photograph of the stripe pumping configuration adopted here. Reprinted with permission from ref. [129] Copyright 2016, American Chemical Society. (g) Pump-fluence relationship determined for the treated $CsPbBr_3$ QD film in 1 PA and 2 PA process. (h) Threshold behavior of the intensity of the ASE of the treated $CsPbBr_3$ in 1 PA and 2 PA process. Reprinted with permission from ref. [130] Copyright 2015, American Chemical Society.

and iodide-substitute QDs from $CsPbBr_3$ QDs (see Fig. 11a) [131]. The $CsPbI_3$ QDs were chosen for photodetectors as they have a longer radiative lifetime than $CsPbCl_3$ and $CsPbBr_3$. The adopted device structure is shown in Fig. 11b where the photodetectors based on $CsPbI_3$ NCs exhibited a good on/off photocurrent ratio of 105 and rise and decay times of 24 and 29 ms, respectively (Fig. 11c-g). Thereafter, Zeng and coworkers demonstrated high-performance photodetectors based on $CsPbBr_3$ QDs with plasma synergetic enhancement [132]. In this case, the Au NCs were introduced into the perovskite $CsPbBr_3$ QDs, the as-fabricated device showed great improvement due to localized surface plasmon resonance effect with the on/off ratio and photocurrent increased from 1.6 × 105 and 245.6 μA to 1.6 × 106 and 831.1 μA, respectively. The improved performance after localized surface plasmon resonance (LSPR) can be seen in Fig. 11h-m.

3. Molecular-level low dimensional metal halide hybrids

Lowering the dimensionality of the organic-inorganic metal halide hybrids from 3D network to 2D layer, 1D wire, and 0D molecular/cluster structures reduce the conductivity significantly along the direction in which the metal-halogen bonding network is disrupted. The dimensional reduction increases the band gap and the exciton binding energy due to quantum and dielectric confinements. The increasing level of exciton localization could enhance radiative recombination. Both Wannier-Mott and self-trapped excitons (STEs) have been observed experimentally in low-dimensional metal halide hybrids [19,20,22,133–136]. A STE is formed when a localized exciton causes local lattice distortion, which in turn traps the exciton. The STE formation is promoted by high ionicity, low dimensionality, and soft lattice which typically leads to narrow conduction and valence bands. These features promote the creation of bound exciton levels inside the bandgap, while the soft lattice reduces the energy cost for local structural distortion. Therefore, the STE is more frequently observed in low-dimensional metal halide hybrids. Compared to the Wannier-Mott exciton, the optical emission from STE is usually strongly Stokes shifted with broad emission band due to the extensive excited-state structural relaxation associated with the exciton self-trapping.

3.1. 2D metal halide hybrids

3.1.1. Layered Ruddlesden-Popper Perovskites

The research attention on 2D and quasi-2D organic metal halide hybrids have grown significantly in recent years for their unique optoelectronic properties and higher stability than 3D perovskites. This type of materials has the general formula $A_{n-1}A'_2B_nX_{3n+1}$, where A' is a monovalent large organic cation which acts as a spacer between the inorganic layers, A is a small cation incorporated into the inorganic framework, B is a bivalent metal cation and X is a halogen ion. Depending on the number of metal halide layers, they can be classified as single layered 2D (n = 1) or quasi-2D ($1 < n < \infty$) metal halide hybrids. Reducing the dimensionality from 3D to 2D significantly reduces the conductivity along the direction perpendicular to the inorganic layers and increases the band gap. The conduction and the valence bands of the 2D halide perovskites remain dispersive along directions parallel to the inorganic layers as shown in the calculated electronic band structures of 2D Ruddlesden-Popper hybrid lead iodides $(C_4H_9NH_3)_2(CH_3NH_3)_{n-1}Pb_nI_{3n+1}$ with three different thicknesses of the inorganic layers (n = 1, 3, and 4) (Fig. 12a) [133]. In the case of $(C_4H_9NH_3)_2PbI_4$ (n = 1), the electron and hole effective masses along the directions parallel to the Pb iodide layers are still comparable to those in 3D halide perovskites (< 0.3) [133,137]. Increasing the Pb iodide layer thickness leads to reduced band gap and carrier effective masses. This trend is also applied to inorganic 2D metal halides as demonstrated by DFT calculations on the hypothetical $Cs_{n+1}Pb_nI_{3n+1}$ layered perovskite family (tetragonal, space group I4/mmm) [138]. The DFT calculations of 3D $CsPbI_3$ and 2D Cs_2PbI_4 perovskites further show

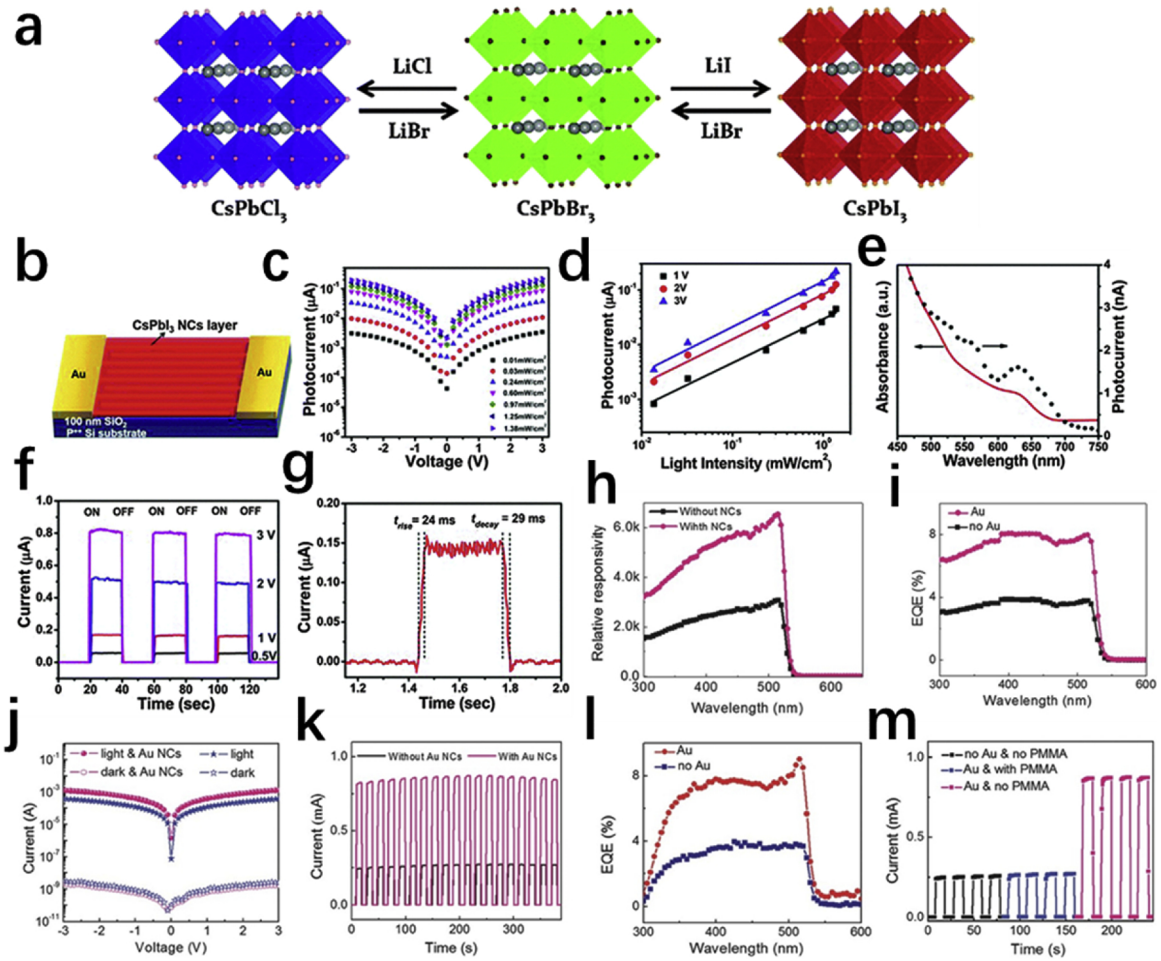

Fig. 11. (a) Schematic of the anion exchange reaction in $CsPbX_3$ NCs. (b) Schematic of $CsPbI_3$ NCs photodetector. Reprinted with permission from ref. [131] Copyright 2016, The Royal Society of Chemistry (c) I–V characteristics of closed-packed $CsPbI_3$ NC films as a function of incident light intensity. (d) Dependence of the photocurrent on the light intensity at different applied bias. (e) Absorption and spectral dependence of photocurrent measured at 1 V bias. (f) Photocurrent-time response measured in the dark and under illumination using a laser diode at 405 nm. (g) Rise and decay time of the photodetector device. (h) Relative responsivity and (i) EQE spectra of devices with and without Au NCs under 2 V bias from front illumination. (j) Measured I–V characteristics of the two devices under 532 nm laser (4.65 mW cm^{-2}). (k) The reproducible current-time curves of $CsPbBr_3$ NC/(Au NCs) photodetectors under 532 nm laser (4.65 mW cm^{-2}) illumination under 2 V bias. (l) EQE spectra of two devices under 2 V bias on glass substrate from back illumination. (m) Current-time curves of photodetectors without Au NCs, with PMMA (spin-coating between Au and $CsPbBr_3$ NCs, ~100 nm) and Au without PMMA. Reprinted with permission from ref. [132] Copyright 2016, Wiley-VCH.

that decreasing the Pb-I-Pb bond angle from the 180° reduces the hybridization between the linear p orbitals in the valance and the conduction bands, leading to narrower valence and conduction bands, and larger band gaps.

Reducing the number of metal halide layers n also simultaneously increases the exciton binding energy due to quantum and dielectric confinements. This can be evidenced by the decreased exciton dissociation rate and increased radiative-decay recombination rate for 2D perovskites with small inorganic layer thickness. For example, in $(C_4H_9NH_3)_2(CH_3NH_3)_{n-1}Pb_nI_{3n+1}$ with n = 1–4, narrow exciton absorption and emission bands with negligible Stokes shifts were reported [133]. Atomically thin 2D perovskites $(C_4H_9NH_3)_2PbBr_4$ with well-defined square shape and large size was reported by Yang and coworkers [14]. The unusual structural relaxation leads to the band gap widening. Strongly Stokes-shifted broadband STE emission has also been reported for many 2D hybrid Pb halide perovskites, especially for the more ionic bromide and chloride perovskites [19–21,139]. Gélvez-Rueda and coworkers used microwave conductivity techniques and photoluminescence measurements to investigate the dissociation and recombination of electron-hole pairs in 2D $(C_4H_9NH_3)_2(CH_3NH_3)_{n-1}Pb_nI_{3n+1}$ Ruddlesden-Popper hybrid perovskites [140]. The mobility of charge, the probability of exciton dissociation, and the lifetime of charges increased along with the thickness of the quantum wells owing to an increased dielectric shielding of the electron-hole interactions. Zheng and coworkers studied the effect of different types of linear or branched spacing cations on the photo-induced charge carrier dynamics using both transient absorption and transient photoluminescence spectroscopy [141]. The inter-phase charge/energy transfer was found to be faster in the case of the shorter spacing cations which can prevent the charge accumulation as the result of the unbalanced transfer rates between electrons and holes. Moreover, Proppe and coworkers showed the importance of the choice of the spacing cation on governing the distribution of quantum wells in quasi-2D organic inorganic metal halide hybrids and their effect on the optoelectronic properties [142]. Liu and coworkers showed that the multi-quantum-well structure in phenylethylamine lead iodide, $(PEA)_2PbI_4$, enhances the quantum and dielectric confinements, leading to a giant two-photon absorption and saturation effect larger than those of 3D perovskite films [143].

The single-layered 2D organic-inorganic metal halide hybrids, as the extreme case of $A_{n-1}A'_2B_nX_{3n+1}$ (n = 1), have been investigated for decades. The early report of 2D organometal halide perovskites dates back to the 1980s [148,149] when long alkyl chain ammoniums were used as organic spacers between the inorganic single layers. To obtain

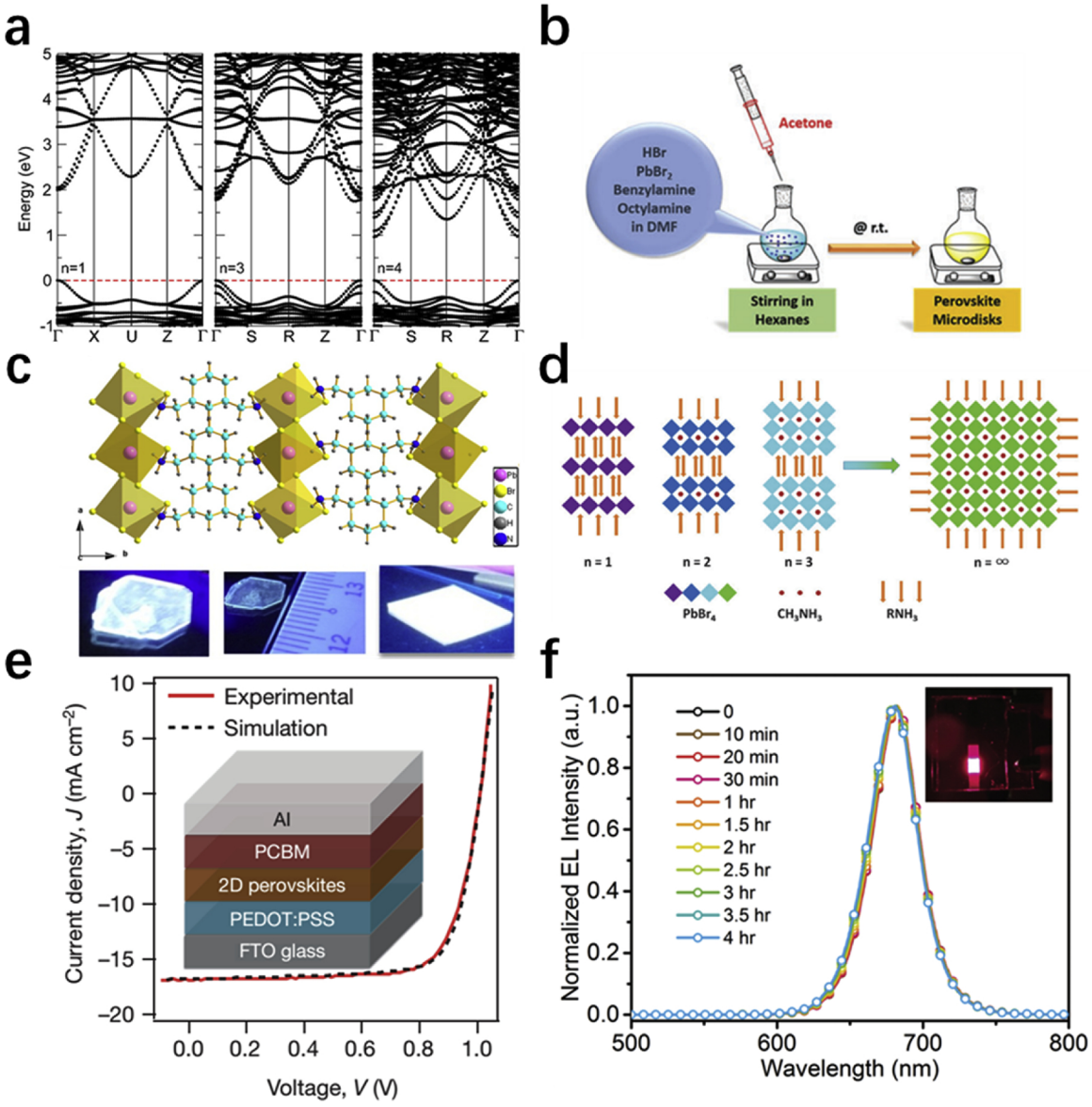

Fig. 12. (a) Electronic band structure of the polar configurations of selected $(BA)_2(MA)_{n-1}Pb_nI_{3n+1}$ perovskites (n = 1, 3, 4) along the Γ(0,0,0)-X/S(1/2,0,0)-U/R(1/2,0,1/2)-Z(0,0,1/2)-Γ(0,0,0) path (solid vertical lines) throughout the Brillouin zone. The Fermi level is set to 0 eV and indicated by the horizontal broken red line. Reprinted with permission from Ref [133] Copyright 2016 American Chemical Society. (b) One-pot solution synthetic method for highly luminescent layered lead(II) bromide perovskite microdisks. Reprinted with permission from Ref [26] Copyright 2015 Royal Society of Chemistry. (c) Top: Crystal packing diagram for single-layer 2D $(CyBMA)PbBr_4$ (CyBMA: cis-1,3-bis(methylamino)cyclohexane). Bottom: Photographs of a $(CyBMA)PbBr_4$ crystal with scale bar and spin-coated film illuminated under UV lamp. Reprinted with permission from Ref [144] Copyright 2017, Wiley-VCH. (d) The schematic layered structures of perovskites from 2D to 3D, i.e. $(RNH_3)_2(CH_3NH_3)_{n-1}Pb_nBr_{3n+1}$ (where RNH_3 is the long organic ammonium cation and n = 1, 2, 3…∞). Reprinted with permission from Ref [145] Copyright 2016, Royal Society of Chemistry. (e) Experimental (red line) and simulated (black dashed line) current-density-voltage (*J-V*) curves under an AM.1.5 G solar simulator for planar devices using 2D $(BA)_2(MA)_3Pb_4I_{13}$ (BA = *n*-butylammonium) perovskites as the absorbing layer at an optimized thickness (230 nm). The inset shows the device architecture. Reprinted with permission from Ref [146] Copyright 2016 Nature Publishing Group. (f) Electroluminescence spectral stability under 3.5 V continuous voltage operation of $(BnA)_2Cs_{n-1}Pb_nI_{3n+1}$ (where BnA = benzyl ammonium) based device. Inset: photograph of device @ 4 V. Reprinted with permission from Ref [147] Copyright 2018 WILEY-VCH. (For interpretation of the references to colour in this figure legend, the reader is referred to the web version of this article).

the bulk assembly 2D crystal structure, solution-processing method is the most popular method because of its simplicity and effectiveness in growing high-quality crystals. For instance, our group used a facile one-pot synthesis method (Fig. 12b) to prepare single-layered 2D lead bromide microdisks, which exhibited highly efficient deep blue emission and great stability [26]. Chen and coworkers employed a ternary co-solvent method and studied the effect of solvent volume ratio, crystallization temperature, and solvent polarity on the morphologies of the 2D perovskite sheets with restricted thickness [150]. Zhang and coworkers used a binary solvent mixture at room temperature instead of ternary solvent to synthesize single-layered 2D sheets with high quantum yield and negligible Stokes shift and studied the effect of crystal thickness on the photoluminescence properties [151]. $(C_{18}H_{37}NH_3)_2PbI_4$ with a long alkyl chain organic cation was found to undergo a phase transition at elevated temperature due to the melting of the oriented alkyl chains which resulted in the expansion of the bi-layer thickness [152]. Neogi and coworkers reported that 2D organic metal halide $(CyBMA)PbBr_4$ (CyBMA: cis-1,3-bis(methylamino)cyclohexane) could exhibit a broadband emission from self-trapped excited states (Fig. 12c) [144].

Quasi-2D organic metal halide hybrids are the bulk assemblies of 2D metal halide nanosheets with larger inorganic layer thickness than single layer 2D organic metal halide hybrids. Several approaches have been used to control the inorganic layer number n and their bandgaps. Stoumpos and coworkers synthesized 2D and quasi-2D $(CH_3(CH_2)_3NH_3)_2(CH_3NH_3)_{n-1}Pb_nI_{3n+1}$ perovskites with various thickness n by adjusting the ratio between the spacer cation and the small organic cation [133]. Soe and coworkers reported a series of 2D $(GA)(MA)_nPb_nI_{3n+1}$ (n = 1–3, GA: guanidinium, $C(NH_2)_3^+$) with alternating cations in the organic interlayer space [153]. $(C_4H_9NH_3)_2(MA)_2Pb_3Br_{10}$ quasi-2D crystals were obtained by temperature lowering method with seed growth, which was found to have ferroelectric properties [154]. Furthermore, a series of mixed-halide quasi-2D $(CH_3CH_2NH_3)_4Pb_3Br_{10-x}Cl_x$ were reported by Mao and coworkers, in which the broadband white-light emission was attributed to the high distortion level of the inorganic layers induced by the large ethyl ammonium cations [155]. The experimental bandgap and exciton binding energy for 2D organic metal halide hybrids were dependent on the layer number n and also the chemical composition, consistent with the theoretical modeling. In 2016, our group reported a series of quasi-2D organic metal halide hybrids with a chemical formula of $(RNH_3)_2(CH_3NH_3)_nPb_nBr_{3n+1}$ with tunable emission ranging from deep blue to bright green (Fig. 12d) [145]. Aharon and coworkers synthesized a mixed-halide quasi-2D $(C_8H_{17}NH_3)_2(CH_3NH_3)_2Pb_3(I_xBr_{1-x})_{10}$ ($0 > x > 1$) with nanorod morphology, [156] which showed strong photoluminescence with bandgaps controlled between 1.9 eV and 2.26 eV by halide exchange from iodide to bromide. In addition, there are several studies focusing on lead-free 2D organic metal halide hybrids. For example, Cheng and coworkers synthesized a 2D mixed Ge-Sn halide hybrids, $(PEA)_2Ge_{1-x}Sn_xI_4$ (where PEA = $C_6H_5CH_2CH_2NH_3^+$) [157]. The band gaps decreases linearly with increasing Sn/Ge ratio and $(PEA)_2Ge_{0.5}Sn_{0.5}I_4$ has the smallest bandgap of 1.95 eV suitable for potential photovoltaic applications. Ma and coworkers reported quasi-2D hybrid $BA_2MA_{n-1}M_nI_{3n+1}$ (M = Sn or Ge, n = 2–4) and approached the optimal bandgap range for solar cells by increasing n [158]. It is also worth mentioning that some non-traditional 2D perovskites have emerged recently. For instance, Que and coworkers synthesized a new single-layer 2D organic metal halide in which the large organic cations bis-protonated 2-(2-aminoethyl) pyrazole were incorporated into six adjacent octahedrons [159]. Other than the Ruddlesden-Popper phase, Dion-Jacobson phase perovskite with divalent organic cations as interface spacers was also demonstrated by Mao and coworkers [160].

The unique and remarkable properties of 2D organic metal halide hybrids make them promising materials for various electronic devices. In 2014, the use of 2D organic-inorganic metal halide hybrids in photovoltaics was investigated by Smith and coworkers (Fig. 12e). Even though the efficiency of these solar cells was low, their superior chemical stability and moisture resistance made them promising candidates to replace 3D perovskites for perovskite solar cells [17]. After that, tremendous efforts have been made to improve the performance of solar cell devices based on 2D organic metal halide hybrids and a respectable PCE of 12.52% has been achieved [146]. It was found that a strong vertical orientation of the 2D nanostructures on the substrate is favorable for charge transport and thus could enhance the PCE [161,162]. More recently, Passereli and coworkers demonstrated a new organic cation that could improve the out-of-plane conductivity in single layered 2D organic metal halide hybrids [163]. In contrast to the pure quasi-2D crystals with fixed n numbers, it is intriguing that thin films in solar cells formed by solvent processing usually contain several phases with varied n numbers. Liu and coworkers found that, the film of $(BA)_2(MA)_{n-1}Pb_nI_{3n+1}$ (BA = $CH_3(CH_2)_3NH_3^+$, MA = $CH_3NH_3^+$) is a mixture of multiple perovskite phases, with n = 2, 3, 4 and $\approx \infty$, which naturally align in the order of n along the direction perpendicular to the substrate. The band alignment between the 2D perovskite phases drives the electrons and holes to opposite surface of the films, which is beneficial for photovoltaic applications [164]. Yan and coworkers observed the similar vertical phase separation phenomenon for a post-annealed $(C_4H_9NH_3)_2MA_3Pb_4I_{13}$ thin film and found that the efficient energy transfer and possible charge transfer account for the high device performance [165]. The mechanism of energy transfer from low-n to high-n quasi-2D perovskite was studied by Williams and workers, who suggested the excitonic funneling from one side to another side of the film could happen in a time scale of 100 ps [166]. Other than PVs, 2D organic metal halide hybrids were also found to have applications in LEDs. Saito and coworkers explored the use of 2D organic metal halide hybrids in electroluminescent devices in the 1990s [167,168]. Tsai and coworkers developed a stable and bright emitting LED by controlling the 2D quantum wells thickness and the phase purity [169]. Recently, our group developed a highly efficient stable red LED based on quasi-2D $(BnA)_2Cs_{n-1}Pb_nI_{3n+1}$ (where BnA = benzyl ammonium) with an EQE of 6.23% as shown in Fig. 12f [147]. Exceptional electroluminescence spectral stability under continuous device operation has been achieved for these red perovskite LEDs. The phase separation and energy funnel effect also exist in some LED thin films. The efficient energy transfer from low-n to high-n species in the film results in high EQE and narrow emission spectrum of the electroluminescence devices. Wang and coworkers reported an LED based on solution-processed self-organized 2D perovskite film with a quantum efficiency of up to 11.7%, exceptionally high-power performance, and high stability. They attributed the outstanding device performance to the multiple quantum well structures, in which components with lower bandgaps were confined by components with larger bandgaps resulting in efficient radiative decay [170]. Yuan and coworkers also fabricated a thin film containing $(C_6H_5C_2H_4NH_3)_2(CH_3NH_3)_{n-1}Pb_nI_{3n+1}$ with multiple n numbers. The multi-components act as charge carrier concentrators which ensure the radiative recombination process outcompetes the non-radiative recombination at traps and defects [171]. Very recently, Zhao and coworkers fabricated a LED with a quasi-2D/3D perovskite-polymer bulk heterostructure. The ultrafast excitation migration to low energy sites eliminates the non-radiative pathways leading to near 100% PLQY and an excellent device EQE of 20.1% [172]. Moreover, single-layered 2D and quasi-2D perovskites were also applied to thin-film transistors [173,174], lasers [175,176], and spintronics [177], etc. A more detailed list of 2D perovskite materials and their applications in devices can be found in previous reviews and references therein [34,36,178].

3.1.2. Corrugated-2D perovskites

The corrugated-2D structure can be achieved by cutting 3D perovskites into slices along the (110) crystallographic direction [179]. Back in the 90s, Mitzi and coworkers reported the first (110) perovskites, $[NH_2C(I)=NH_2]_2(CH_3NH_3)_mSn_mI_{3m+2}$ (m = 2), which were stabilized by methylammonium and iodoformamidinium cations [180]. Apart from "2 × 2" corrugated 2D structure, a new layered Sn(II) iodides perovskite, α-$[NH_3(CH_2)_5NH_3]SnI_4$, with "4 × 4" structure was reported by Guan and coworkers, as shown in Fig. 13a. These "4 × 4" corrugated structures are very rare as compared to "2 × 2" counterparts [181,182]. Later, a Stokes-shifted emission was observed for the first time in $(C_6H_{13}N_3)PbBr_4$ stabilized by N-(3-aminopropyl)-imidazolium cations [183]. Karunadasa group has explored the potential of these corrugated-2D materials as a single component white light emitter. A series of corrugated-2D perovskites such as (N-MEDA)$PbBr_4$ and (EDBE)PbX_4 (N-MEDA = N^1-methylethane-1,2-diammonium; EDBE = 2,2'-(ethylenedioxy)bis(ethylammonium); X = Cl and Br) were discovered in recent years. Due to the efficient exciton self-trapping in corrugated-2D structure, broadband intrinsic white-light emissions were observed for these materials [19,20]. (Fig. 13b) In 2017, a new corrugated-2D "3 × 3" lead bromide perovskite, α-(DMEN)$PbBr_4$ (DMEN = 2-(dimethylamino)ethylamine) was obtained by Kanatzidis and coworkers, which is thermodynamically stable in solution and can be transformed from the kinetically stable β-(DMEN)$PbBr_4$ (Fig. 13c) [184].

One of the most important optical properties of corrugated-2D

perovskites is their broadband white emission due to the formation of self-trapped excitons, which was often observed in low dimensional metal halide hybrids (Fig. 13d) [20,139]. In corrugated-2D perovskites, the strong exciton-lattice coupling can induce the transient lattice distortion, resulting in the strongly Stokes-shifted broadband emission [179]. Unlike 3D ABX_3 perovskites exhibiting narrow-band emission from the free excitons only, corrugated-2D perovskites could have emissions from both free excitons and self-trapped excitons simultaneously. The emission from the self-trapped excitons is broadened due to the distortion of the excited state structures with respect to the ground state (given by the Huang-Rhys parameter, S) [18,139,186]. The broadband white-light emission from corrugated-2D structures could be analogous to sunlight, making them of great interest for application as single component down-conversion emitters in optically pumped white LEDs. The white emission colors are tunable from "cold" to "warm" white light by changing organic cations and halogen composition (Fig. 13e, f). The color rendering index (CRI) has already been improved to 93 in N-(3-aminopropyl)-imidazolium tetrachloro-lead perovskite [187]. Despite high CRI obtained for such corrugated-2D structures, obtaining high PLQEs suitable for practical applications is

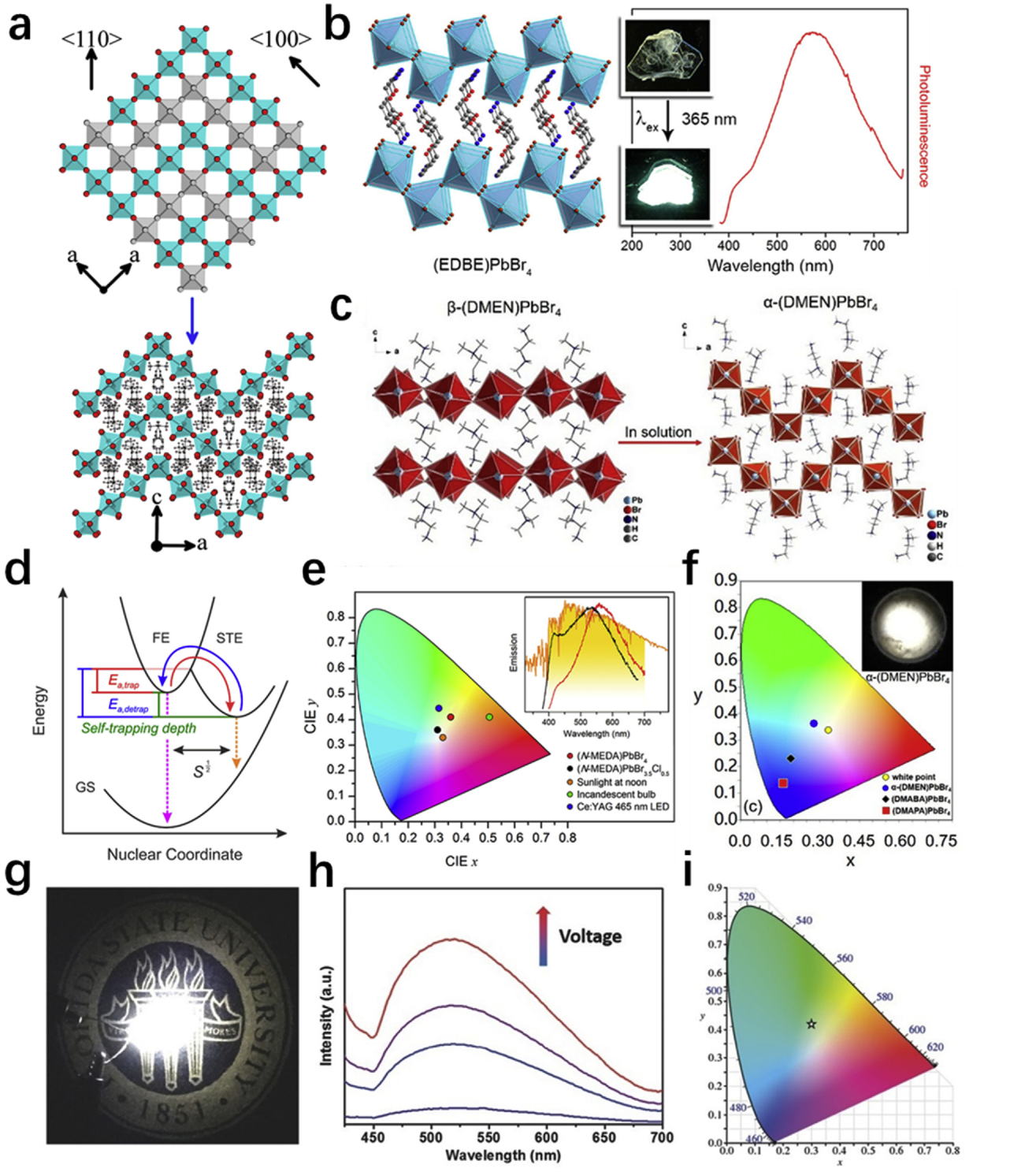

(caption on next page)

Fig. 13. (a) In the crystal structure of α-$[NH_3(CH_2)_5NH_3]SnI_4$, the inorganic layers are composed of 4-octahedra long ⟨100⟩-oriented layer fragments that are interconnected at 45° angles. The resultant zigzag perovskite layers are a combination of the ⟨100⟩-and the ⟨110⟩-oriented fragments that are separated by 1,5-pentanediammonium cations. Reprinted with permission from Ref [185] Copyright 2016, American Chemical Society. (b) Crystal structures of $EDBEPbBr_4$ and emission spectrum (inset: the image of crystals under ambient light and UV irradiation). Reprinted with permission from Ref [19] Copyright 2014, American Chemical Society. (c) Transformation of β-$(DMEN)PbBr_4$ to α-$(DMEN)PbBr_4$ in the mother liquor solution. Reprinted with permission from Ref [184] Copyright 2017, American Chemical Society. (d) Schematic of exciton self-trapping (red arrow) and detrapping (blue arrow) in 2D Pb–Br perovskites (FE = free exciton state, STE = self-trapped exciton state, $E_{a,trap}$ = activation energy for self-trapping, and $E_{a,detrap}$ = activation energy for detrapping). FE emission and STE emission are shown in pink and orange, respectively. Reprinted with permission from Ref [18] Copyright 2017, Royal Society of Chemistry. (e) Chromaticity coordinate diagram for some white-light emitters. Inset: Solar spectrum (orange) with the visible region shaded in yellow and the emission spectra of (*N*-MEDA)$PbBr_4$ (red) and (*N*-MEDA)$PbBr_{3.5}Cl_{0.5}$ (black). Reprinted with permission from Ref [20] Copyright 2014, American Chemical Society. (f) Chromaticity coordinates of α-$(DMEN)PbBr_4$ (0.28, 0.36), Inserted: white light emission picture of polycrystalline α-$(DMEN)PbBr_4$ excited at 365 nm. Reprinted with permission from Ref [184] Copyright 2017, American Chemical Society. (g) Image of a UV-pumped white LED (operated at 3.0 V) by using the microscale $EDBEPbBr_4$ as down-conversion phosphors. (h) Emission spectra of the white-light LED demo at different operating voltages. (i) CIE coordinates for the white LED plotted on the CIE1931 chromaticity chart. Reprinted with permission from Ref [21] Copyright 2016, Wiley-VCH. (For interpretation of the references to colour in this figure legend, the reader is referred to the web version of this article).

still challenging. Most of them suffer from low quantum efficiency because of efficient non-radiative decay and lattice defects in bulk crystals. To date, the $(EDBE)PbBr_4$ showed the highest PLQE of up to 9% in bulk single crystals and of up to 18% in microscale crystals that were prepared via a facile solution processible approach [21]. The emission spectra of the white LED based on a microscale $(EDBE)PbBr_4$ were measured at different voltages, of which the emission structure exhibits little-to-no voltage dependence, as shown in Fig. 13g-h. For microscale $(EDBE)PbBr_4$, a CIE color coordinate (0.30, 0.42) was achieved from the emission at 3.0 V as shown in Fig. 13i with a CCT of 6519 K, corresponding to a "cold" white light. Nevertheless, the PLQEs of reported corrugated 2D materials still do not satisfy the requirement of white emitters for down-conversion LEDs.

To further shed light on the intriguing optical properties of corrugated 2D materials, theoretical calculations have been performed. The optical absorption spectra of corrugated-2D $(EDBE)PbCl_4$ and $(EDBE)PbBr_4$ were calculated by solving the Bethe-Salpeter equation. The results show a sharp excitonic absorption peak and high-energy absorption continuum (Fig. 14), in excellent agreement with the experimental results [188]. The strongly Stokes-shifted broadband emission in $(EDBE)PbX_4$ (X = Cl, Br) was explained by the formation of self-trapped electrons Pb_2^{3+} as well as self-trapped holes X_2^- and Pb^{3+} in the form of small polarons localized in the Pb-halide framework [189]. Here, Pb_2^{3+}, X_2^-, and Pb^{3+} involve the shortening of the Pb-Pb, X-X, and Pb-X distances, respectively. However, the stability of the above polaron species was not demonstrated in calculations. It was simply shown in the calculations that introducing *ad hoc* local structural distortion creates localized electron or hole levels within the band gap, which is expected; but, whether such structural distortion is energetically favorable was not shown. In fact, the Perdew-Burke-Ernzerhof (PBE) exchange-correlation functional used in these calculations is known to be inadequate in describing charge localization associated with the polaron formation; thus, cannot predict the polaron structures [190,191]. Hybrid functional calculations (CAM-B3LYP functional) was further used to study the hole polaron in $(EDBE)PbCl_4$ [188]. The inclusion of a fraction of Fock exchange in the hybrid functional calculation significantly improves the band gap energy and the description of charge localization in insulators [191,192]. The hybrid functional calculation of the polaron in $(EDBE)PbCl_4$ found the shortening of the Pb-X distance, but not the shortening of the Cl-Cl distance. It should be noted that these hybrid functional calculations were performed based on a cluster model, which may introduce errors related to the artificial quantum confinement and

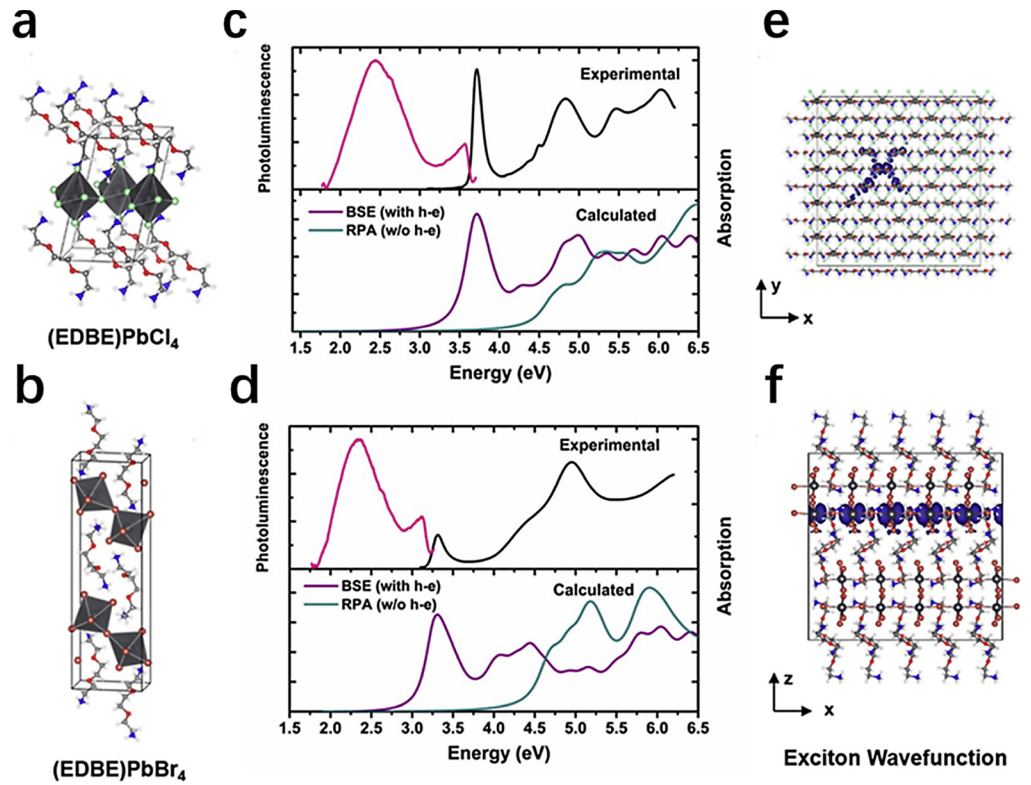

Fig. 14. (a, b) Crystal structures. (c, d) Experimental absorption and PL spectra at room temperature (upper panel) and calculated absorption spectra with and without consideration of hole-electron interactions (bottom panel). (e, f) Illustration of the exciton wave functions corresponding to the excitonic peaks. Reprinted with permission from ref. [188], Copyright 2017, American Chemical Society.

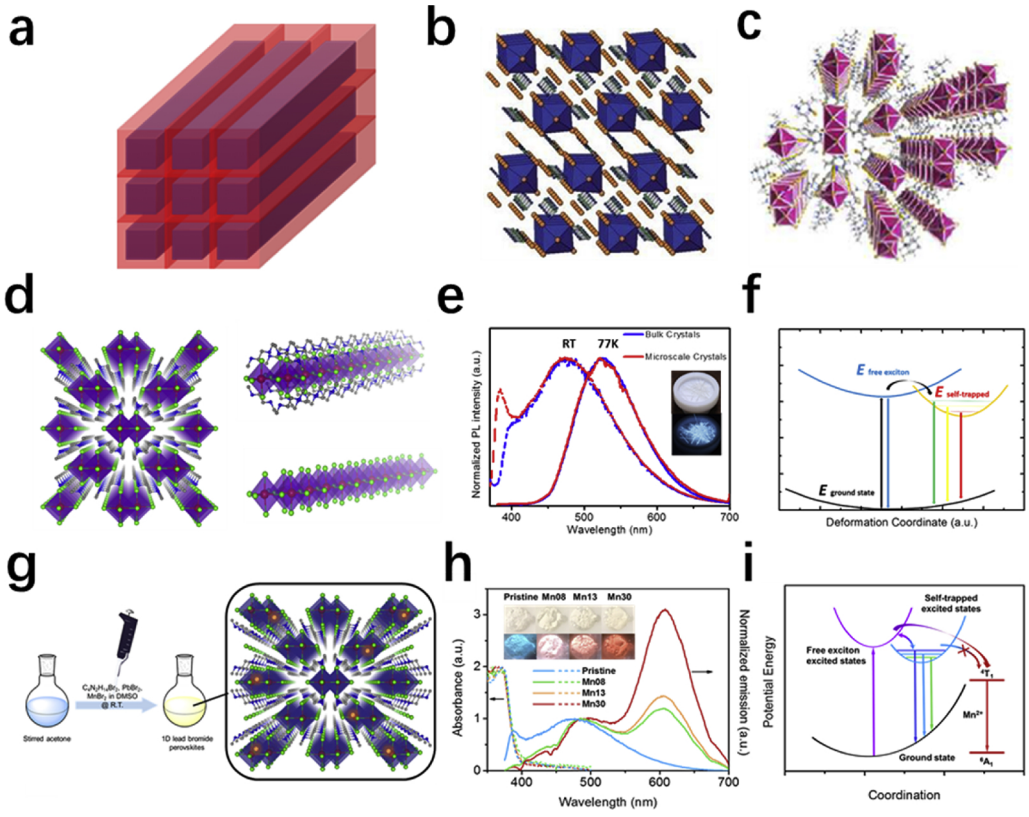

Fig. 15. (a) Schematic illustration molecular level 1D structure (blue: metal halide chains/wires, red: organic cations). (b) 1D chains with corner-sharing of SnI_6 octahedra. (c) Crystal structure of $(2,6\text{-dmpz})_3Pb_2Br_{10}$ (2,6-dmpz = 2,6-dimethylpiperazine), which consists of two types of 1D chains. Reprinted with permission from ref. [196], Copyright 2018, American Chemical Society. (d) Structure of 1D perovskite $C_4N_2H_{14}PbBr_4$ (red spheres: lead atoms; green spheres: bromine atoms; blue spheres: nitrogen atoms; grey spheres: carbon atoms; purple polyhedrons: $PbBr_6$ octahedrons; hydrogen atoms were hidden for clarity). (e) Absorption (dash lines) and emission (solid lines, excited at 360 nm) spectra of the bulk and microscale perovskite crystals at room temperature. (inset) Image of bulk perovskite crystals under ambient light and under UV light (365 nm). (f) Proposed energy diagram and excited state dynamics of 1D lead bromide perovskites: the straight and curved arrows represent optical and energy relaxation/transfer transitions, respectively. Reprinted with permission from ref. [134], Copyright 2017, Nature Publishing Group. (g) One-pot synthesis of Mn-doped 1D lead bromide perovskites. (h) Absorption (dashed line) and emission (solid line) spectra of the pristine and Mn-doped 1D lead bromide perovskites, the inset shows the images of the pristine and Mn-doped 1D lead bromide perovskites under ambient light (top) and UV light (365 nm, bottom). (i) Proposed energy diagram and excited state dynamics of Mn-doped 1D lead bromide perovskites: the straight and curved arrows represent optical and energy relaxation/transfer transitions, respectively. Reprinted with permission from ref. [197], Copyright 2017, American Chemical Society. (For interpretation of the references to colour in this figure legend, the reader is referred to the web version of this article).

the surface effect. More rigorous hybrid functional calculations of extended crystal structures based on the supercell model should shed light on the structure and energetics of polarons and excitons in layered perovskites.

3.2. 1D metal halide hybrids

In bulk assemblies of 1D organic metal halide hybrids, the metal halide octahedra MX_6 can form chains via corner-sharing, edge-sharing, or face-sharing. These anionic metal halide chains and surrounding organic cations can be assembled to form the single crystalline bulk structures. Unlike morphological 1D metal halide perovskites being nanomaterials, 1D organic metal halide hybrids are large crystals indeed with the 1D structure at the molecular level, [193] which can be considered as bulk assemblies of metal halide quantum wires (Fig. 15a). The first examples of 1D metal halide hybrids were reported in the 1990s, when Mitzi and coworkers prepared a family of metal halide hybrid structures $[NH_2C(I)=NH_2]_2(CH_3NH_3)_mSn_mI_{3m+2}$ (Fig. 15b) [180,194,195]. Whilst m = 1, the corrugated 2D structures break down into 1D chains with corner-sharing of SnI_6 octahedra. As perovskite-related materials, 1D organic metal halide hybrids have attracted great attention in recent years. A very recent work by Kanatzidis and coworkers has shown that a single crystal can consist of two types of 1D metal halide chains (Fig. 15c) [196]. The recent interest in photoactive 1D metal halide hybrids was greatly promoted by our work in 2017, when we reported a 1D lead halide hybrid $C_4N_2H_{14}PbBr_4$, in which the edge-sharing octahedral chains $[PbBr_4^{2-}]$ are entirely surrounded by the organic cations $C_4N_2H_{14}^{2+}$ (Fig. 15d) [134]. This structure can be considered as the bulk assembly of core-shell quantum wires [185]. This unique 1D structure of $C_4N_2H_{14}PbBr_4$ synthesized by wet chemistry method exhibits intriguing bluish white-light emission upon UV irradiation due to the strong quantum confinement in 1D structure and the formation of self-trapped excitons (Fig. 15e, f). The as-prepared bulk and microscale 1D lead bromide perovskites showed broadband emission with a maximum at 475 nm and a fwhm of 157 nm with PLQE of 18–20% for bulk single crystals and 10–12% for microscale crystals, respectively. To further improve the quality of white emission, Mn ions have been introduced to these 1D lead bromide perovskites [197]. In these Mn-doped 1D perovskites prepared by a facile one-pot synthesis method, the excited-state energy transfers from the direct free exciton excited states to the STEs and doped Mn^{2+} ions without energy transfer between the STEs and Mn^{2+} states (Fig. 15g-i). By combining the self-trapped emission and Mn dopant emission, tunable broadband white emissions with CRI of up to 87 and a PLQE of up to 28% were achieved.

Replacing Br with Cl, 1D $C_4N_2H_{14}PbCl_4$ was prepared, in which edge sharing octahedral lead chloride chains $[PbCl_4^{2-}]_\infty$ are surrounded by $C_4N_2H_{14}^{2+}$ cations. Unlike most of the previously reported organic metal halide hybrids with excitation independent emissions, this 1D $C_4N_2H_{14}PbCl_4$ exhibits inverse excitation-dependent broadband emission from bluish-green to yellow. (Fig. 16a, b) DFT calculations were performed to gain a better understanding of the mechanism of this excitation-dependent broadband emission. It was found this 1D hybrid material has two emission centers corresponding to the self-trapped excitons and vacancy-bound excitons. The excitation-dependent emission is the result of different populations of these two types of excitons generated at different excitation wavelengths. Replacing Pb^{2+} by Sn^{2+} in 1D structure, a lead-free 1D $C_4N_2H_{14}SnBr_4$ hybrid was discovered by our group [199]. (Fig. 16c) Interestingly, this non-emissive 1D $C_4N_2H_{14}SnBr_4$ can undergo structural transformation upon continuous UV irradiation to form a highly emissive 0D Sn bromide hybrid with

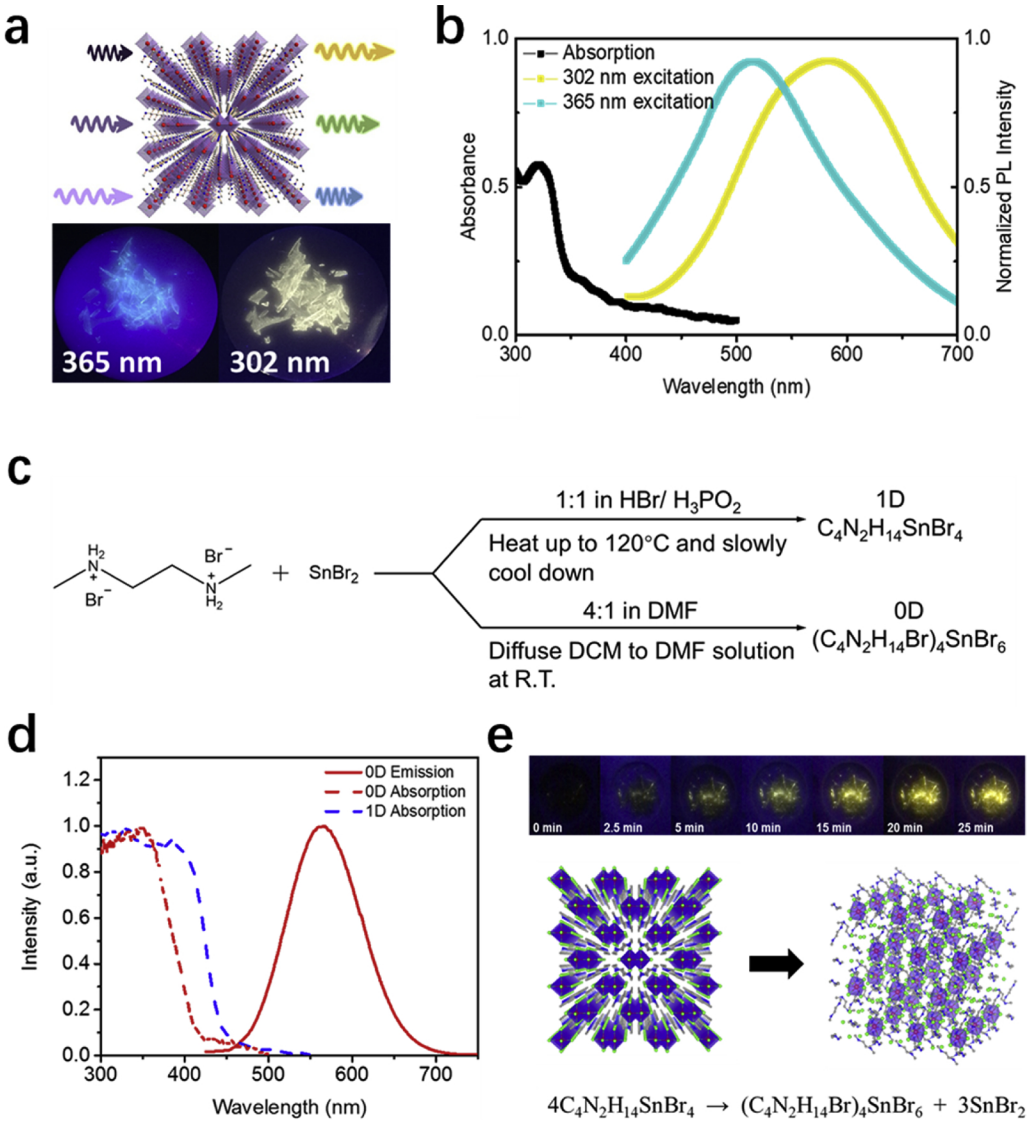

Fig. 16. (a) Structure of $C_4N_2H_{14}PbCl_4$ and photographs of crystals under 365 nm and 302 nm excitation. (b) Absorption (black) and emission spectra excited at 365 nm (green) and 302 nm (yellow), respectively. Reprinted with permission from ref. [198], Copyright 2018, American Chemical Society. (c) The synthesis of the 1D and 0D Sn bromide perovskites. (d) Absorption spectra of 1D $C_4N_2H_{14}SnBr_4$ and 0D $(C_4N_2H_{14}Br)_4SnBr_6$, as well as the emission spectrum of 0D $(C_4N_2H_{14}Br)_4SnBr_6$. (e) Photographs of 1D Sn bromide perovskite crystals under UV irradiation. (top) the proposed reaction for the photoinduced structural transformation. (bottom). Reprinted with permission from ref. [199], Copyright 2017, Wiley-VCH. (For interpretation of the references to colour in this figure legend, the reader is referred to the web version of this article).

near-unity PLQE. This structural transformation was confirmed by the theoretical results that kinetically preferred 1D structure can transform into a thermodynamically stable 0D structure, as shown in Fig. 16d, e. Besides metal halide quantum wires, our group has also discovered for the first time a 1D metal halide hybrid containing tubular metal halides [200]. With the protonated organic cation, hexamethylenetetramine (HMTA, $C_6H_{13}N_4^+$), a bulk assembly of 1D lead bromide nanotubes of $(C_6H_{13}N_4)_3Pb_2Br_7$ was prepared by the slow solution diffusion method. In the tubular structure, there are two building blocks: the protonated HMTA ($C_6H_{13}N_4^+$), and face-sharing metal halide dimers ($Pb_2Br_9^{5-}$). In an individual nanotube, six face-sharing metal halide dimers are connected at the corners to form rings, which are coated with the protonated HMTA on both the interior and the exterior of the tube (Fig.17a). The 1D lead bromide tubular structure is completely isolated and has highly localized electronic states with strong quantum confinement, exhibiting the intrinsic optical properties of an individual tube. Due to the self-trapped excitons, the structure showed broadband yellowish-white emission (fwhm ~ 158 nm) with large Stokes shift and a PLQE of around 7% (Fig. 17b). The relatively low PLQE, as compared to 1D nanowire structure, is likely caused by more non-radiative pathways in the 1D nanotube structures. We further conducted an experimental study probing the dynamics of these self-trapped excitons in this bulk assembly of 1D organic metal halide nanotubes. Through time-resolved photoluminescence measurements at different excitation intensities, we observed a marked variation in the PL decay behavior that is manifested by an accelerated decay rate with increasing excitation fluence (Fig. 17c). Our results offer direct evidence of the occurrence of an exciton-exciton annihilation process, a nonlinear relaxation phenomenon that takes place only when some of the self-trapped excitons become mobile and can approach either each other or other trapped excitons (Fig. 17d). We further identified a fast and dominant PL decay component with a lifetime of ~ 2 ns with a nearly invariant relative area for all acquired PL kinetics, suggesting that this rapid relaxation process is intrinsic.

To address the toxicity issue of Pb, researchers have developed and studied 1D organic metal halide hybrids containing other metals with the similar electronic structure as Pb, including Sn, Sb, and Bi. Mousdis and coworkers reported the zigzag-chain 1D Sb halide hybrids, $[CH_3SC(NH_2)_2]_2SbX_5$, containing corner-sharing SbX_6 octahedra and $CH_3SC(NH_2)_2^+$ cations in the cavities between the chains [202]. Despite higher E_g values in $[CH_3SC(NH_2)_2]_2SbX_5$ than that of the $MAPbI_3$ perovskite and low efficiencies, these non-toxic new materials are more stable, rendering them good candidates for optoelectronic devices. Zhang and coworkers recently reported a new lead-free organic Sb halide hybrid, $(C_6H_{14}N)_2SbCl_5$, which is composed of hexamethyleneimine and one-dimensional $[SbCl_5]_n^{2-}$ polyanionic zigzag chains [203]. Switchable materials have been studied in the past few years because of their advantages in memory devices, processors, and sensors.

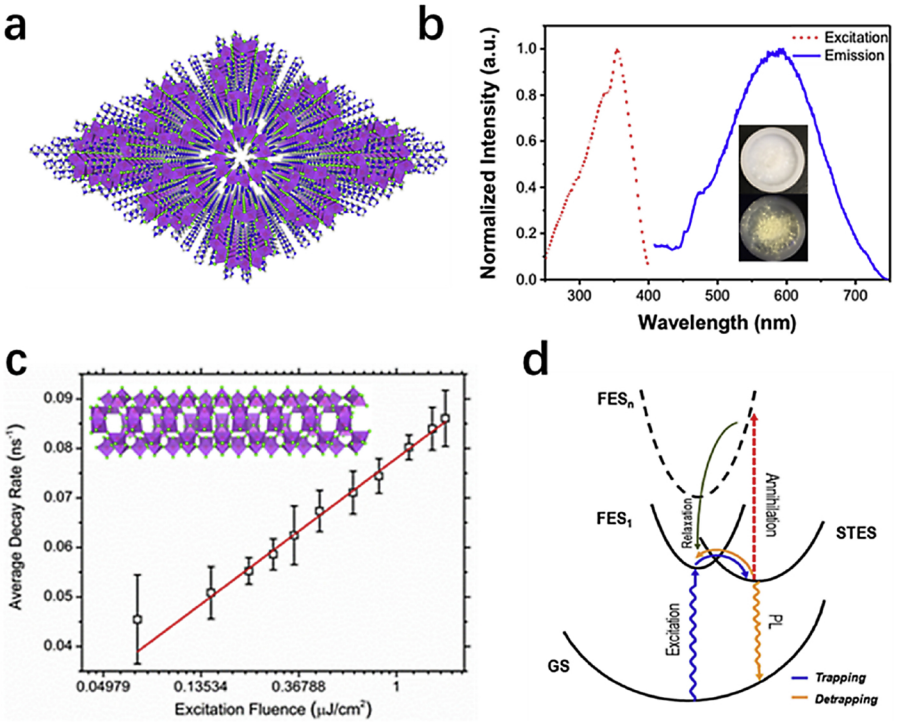

Fig. 17. (a) View of the structure of $(HMTA)_3Pb_2Br_7$ (red: lead atoms; green: bromine atoms; blue: nitrogen atoms; gray: carbon atoms; purple polyhedra: $PbBr_6$ octahedra and Pb_2Br_9 dimers; hydrogen atoms are hidden for clarity) (b) Excitation (black line, probed at 580 nm) and emission (red line, excited at 380 nm; blue line, excited at 350 nm) spectra of $(HMTA)_3Pb_2Br_7$ crystals at room temperature. (inset) Images of $(HMTA)_3Pb_2Br_7$ crystals under ambient light and UV light (365 nm) Reprinted with permission from ref. [200], Copyright 2017, The Royal Society of Chemistry. (c) The plot of the average PL decay rate as a function of the natural logarithm of the excitation fluence. The error bars were calculated based on the errors of both the decay lifetimes and associated relative amplitudes estimated by the fitting algorithm, and the solid red line depicts a linear fit to the data. The inset shows the same data but plotted on a linear excitation intensity scale. (d) Schematic energy level diagram of a nanotube involving exciton-exciton annihilation and exciton self-trapping and detrapping between the lowest-lying free exciton state (FES_1) and self-trapped exciton state (STES). GS and FES_n denote the ground and a high-lying free exciton state, respectively. Reprinted with permission from ref [201], Copyright 2018, American Chemical Society. (For interpretation of the references to colour in this figure legend, the reader is referred to the web version of this article).

Due to the intriguing order-disorder conformational changes of the flexible organic moiety, nonlinear optical (NLO)-switching activities were observed in $(C_6H_{14}N)_2SbCl_5$. Dammak and coworkers reported the synthesis of an organic-inorganic hybrid $(C_6H_{14}N)_2[BiBr_5]$ by the slow evaporation method [204]. The 1D quantum wire shows a strong blue emission at 457 nm (2.71 eV), which is attributed to radiative recombination of strongly bound excitons. Zhang and coworkers also reported a 1D Bi-based light-absorbing organic halide hybrid, $(C_6H_{14}N)_2BiI_5$, where the corner-sharing octahedral chains are surrounded by 4-methylpiperidinium cations [205]. The environmentally friendly, moisture stable light absorber has a narrow direct band gap of ~ 2.02 eV with long PL lifetime and photoconductive behavior, which makes it promising for application in the field of optoelectronics.

3.3. 0D metal halide hybrids

3.3.1. Bulk assemblies of metal halide species

0D metal halide hybrids are featured with isolated metal halide polyhedrons surrounded by organic or inorganic cations. The earliest reports on metal halide hybrids with 0D structure were on Cs_4PbBr_6, in which $PbBr_6$ octahedrons are separated from each other by Cs^+ cations [206]. Recently, our group has used large organic cations instead of Cs^+ to make highly luminescent bulk assemblies of 0D organic metal halide hybrids [22,135,136,207]. In contrast to morphological 0D systems, such as quantum dots, which typically exhibit small Stokes shifts, narrow emissions, and quantum size effect, molecular-level 0D organic metal halide hybrids retain the photophysical properties (e.g. strongly Stokes-shifted broadband emissions) of individual metal halide polyhedra, which are completely isolated from each other by wide-bandgap organic cations as illustrated in Fig. 18a [207]. As a result, the bulk crystals retain the photophysical properties of individual metal halide building blocks, e.g. high PLQEs, Stokes-shifted broadband emissions, long decay lifetimes. Therefore, these systems can be considered as perfect host-guest systems with the photoactive emitting species doped into the wide bandgap host matrix [22].

In 2017, our group reported a series of 0D organic metal halide hybrids with the chemical formula $(C_4N_2H_{14}X)_4SnX_6$ (X = Br or I) that exhibit broadband emissions (fwhm > 100 nm) with large Stokes-shifts and near-unity PLQEs as shown in Fig. 18a–c [22]. Unlike Cs_4PbBr_6 with small inorganic cations Cs^+, the large-sized wide bandgap organic cation $C_4N_2H_{14}X^+$ inhibits electronic band formation between neighboring $[SnX_6]^{4-}$ octahedra, thereby achieving strong electronic confinement [208]. This allows the bulk crystalline material to display the intrinsic properties of the individual metal halide octahedra. The strongly Stokes-shifted broadband emission was ascribed to ultrafast excited state structural reorganization which is schematically depicted in Fig. 18d. Emission color tunability has also been demonstrated for this class of materials via halide mixing [209]. Taking advantage of their high PLQEs, broad emissions, and large Stokes-shifts, these 0D organic metal halide hybrids are excellent candidates for use as phosphors in down-conversion white LEDs. By combining these 0D organic metal halide hybrids with a commercial blue phosphor, our group demonstrated UV-pumped white LEDs with color tunability from “cold” to “warm” white and good chromaticity coordinates. Fig. 18e shows the white light spectrum generated by these white LEDs and the linear dependence of irradiance on forward bias current.

Beyond the metal halide hybrids based on octahedra, our group has discovered that 0D metal halide hybrids can also be obtained based on other metal halide polyhedrons, such as pyramidal, tetrahedral and seesaw structural metal halides [135,136,210]. Recently, we reported 0D organic metal halide hybrids based on pyramidal $[SbCl_5]^{2-}$ ions exhibiting broadband emissions with large Stokes-shift and near-unity PLQEs. Like the SnX_6^{4-} octahedra in $(C_4N_2H_{14}Br)_4SnX_6$, these Sb chloride pyramids, as shown in Fig. 18f, are isolated from each other and surrounded by wide bandgap large organic cations $C_9NH_{20}^+$ or Ph_4P^+ [22,136]. Interestingly, two synthesis routes have been identified for $(Ph_4P)_2SbCl_5$, where slow crystallization via antisolvent vapor precipitation yields a thermodynamically stable product and a fast crystallization technique through antisolvent injection precipitation produces a highly emissive metastable product which can convert into the thermodynamically preferred product. The thermodynamically stable crystals obtained through the fast crystallization method possessed the higher PLQE of around 99%, which is likely due to the fewer defects in these crystals. Similarly, Xu and coworkers reported a highly efficient green emitting 0D metal halide hybrid consisting of a tetrahedral $[MnBr_4]^{2-}$ surrounded by Ph_4P^+ wide bandgap cations [210].

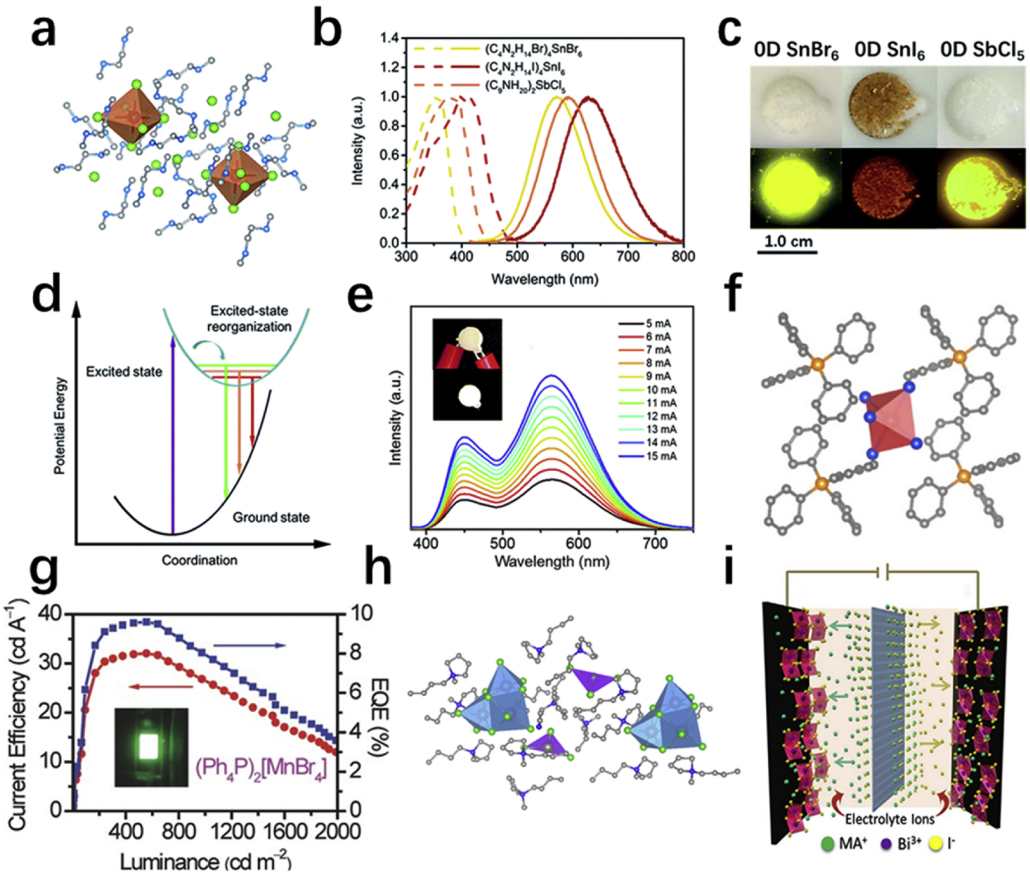

Fig. 18. a) Individual $[SnBr_6]^{4-}$ octahedra surrounded by $(C_4N_2H_{14}Br)^+$ organic ions. b) Strongly Stokes-shifted broadband emission and excitation spectra of $(C_4N_2H_{14}X)SnX_6$ (X = Br, I). (c) Photo of $(C_4N_2H_{14}X)SnX_6$ (X = Br, I) and $(C_9NH_{20})_2SbCl_5$ crystals under ambient light (top) and UV irradiation (bottom). (d) Configuration coordinate diagram illustrating the large Stokes-shift due to excited state structural reorganization. (e) UV pumped down-conversion white LED based on $(C_4N_2H_{14}Br)SnBr_6$ and commercial blue phosphor $BAM:Eu^{2+}$. Reprinted with permission from ref. [22] Copyright 2017, The Royal Society of Chemistry. (f) View of $[SbCl_5]^{2-}$ pyramid surrounded by Ph_4P^+ ions. Reprinted with permission from ref. [136] Copyright 2018, American Chemical Society. (g) Current efficiency and external quantum efficiency of $(Ph_4P)_2MnBr_4$ based OLED; inset: device under operation. Reprinted with permission from ref. [210] Copyright 2017, Wiley-VCH. (h) Crystal structure of 0D metal halide clusters $(C_9NH_{20})_7(PbCl_4)Pb_3Cl_{11}$. Reprinted with permission from ref. [213] Copyright 2018, American Chemical Society. (i) Schematic diagram of an electrochemical double layer capacitor based on $(CH_3NH_3)_3Bi_2I_9$. Reprinted with permission from ref. [217] Copyright 2017, American Chemical Society. (For interpretation of the references to colour in this figure legend, the reader is referred to the web version of this article).

The emission was identified to originate from the d-d $^4T_1$-$^6A_1$ transition of the Mn(II) ions with a tetrahedral coordination geometry. Efficient green LEDs, as illustrated in Fig. 18g were fabricated through solution processing by using this 0D metal halide hybrid as the emitting layer. Moreover, a rare seesaw structural 0D organic Pb bromide hybrid was also discovered, exhibiting highly efficient broadband emission with one of the largest Stokes shift to ever be reported [135]. By using these 0D materials with different colors and a commercial blue phosphor, a series of UV-pumped WLED with extremely high CRIs of up to 99, excellent deep-red color rendering, R9s of up to 99, and superior color quality scale (CQS) values have been fabricated to produce full spectrum white light that approximates halogen or incandescent lighting and natural daylight [211]. By carefully controlling the phosphor blend ratios, white emissions with CCTs, ranging from 3000 to 6000 K, have been achieved, which perfectly mimic sunlight at different times of the day.

In addition to 0D metal halide hybrids based on polyhedrons, metal halide clusters were also investigated as anions to build up the 0D structure. The earliest report of these variants was of $(CH_3NH_3)_3Bi_2I_9$, featuring the localization of excitons on the Bi^{3+} ion and the resulting large binding energy [212]. Very recently, our group reported for the first time a single crystalline assembly of metal halide clusters, $(C_9NH_{20})_7(PbCl_4)Pb_3Cl_{11}$, in which lead chloride tetrahedrons ($PbCl_4^{2-}$) and face-sharing lead chloride trimer clusters ($Pb_3Cl_{11}^{5-}$) co-crystallize with organic cations ($C_9NH_{20}^+$) to form a periodical 0D structure at the molecular level (Fig. 18h) [213]. Blue light emission peaked at 470 nm with a PLQE of around 83% was realized for this single crystalline hybrid material, which is attributed to the individual lead chloride clusters. Upon UV photoexcitation, only $Pb_3Cl_{11}^{5-}$ clusters are excited to the higher energy excited state, which can undergo ultrafast structural reorganization and intersystem crossing from the singlet state (S_1) to the triplet states (T_1) due to the heavy atom effect. A highly efficient blue phosphorescence with a large Stokes shift was then generated by radiative decay from the lowest triplet states. This finding once again shows the molecular nature of small metal halide species in the 0D structure and allows us to establish relations between the emission from either structural reorganization or localized excitons in metal halides and molecular phosphorescence.

Regarding the applications of 0D metal halide hybrids, a few reports have come out demonstrating the use of Sb^{3+} and Bi^{3+} based 0D metal halide hybrids as absorbers for solar cells via solution processing [214–216]. However, the efficiencies reported were not up to par with those reported for 3D perovskites, because of the strong localization of charges on the metal halide cluster. Similar materials with Cs^+ as A site cation have also been studied alongside showing better performance as absorbers for solar cells [216]. On the other hand, Pious and coworkers demonstrated the use of $(CH_3NH_3)_3Bi_2I_9$ in the electrochemical double-layer capacitor. $(CH_3NH_3)_3Bi_2I_9$ was synthesized by dissolving the iodide salts in DMF and heating the solution to remove the solvent to obtain a perovskite powder. Taking advantage of the large vacant surface area in 0D structures, the lower charge-transfer resistance yields high ionic conductivity and consequently a capacitor with three orders of magnitude higher capacitance than that based on 3D $MAPbI_3$ [217]. The schematic diagram of the capacitor is shown in Fig. 18i. Wu and coworkers recently reported Cs_4EuX_6 (X = Br, I) with a trigonal 0D structure and blue emission for use as a self-activated scintillator for gamma-ray detection and spectroscopy. To obtain large single crystals, the Bridgman synthesis method was implemented. In this material, although the conduction band minimum was found to be derived from Cs 6 s orbital, because of the strong electron-hole binding on the Eu^{2+} ion,

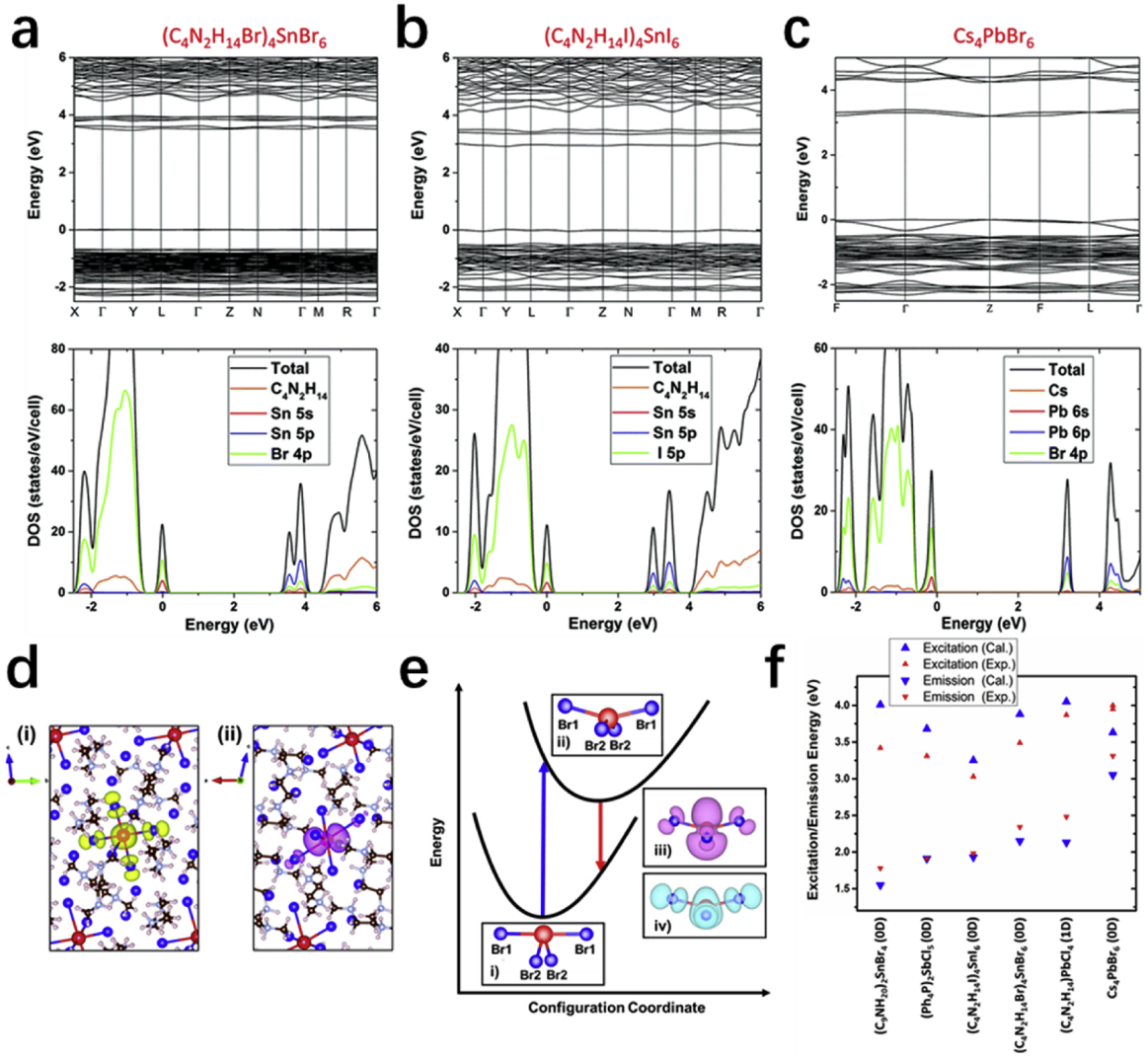

Fig. 19. Electronic band structures and density of states (DOS) of $(C_4N_2H_{14}Br)_4SnBr_6$ (a), $(C_4N_2H_{14}I)_4SnI_6$ (b), and Cs_4PbBr_6 (c) calculated using PBE functionals. The SOC is included in the calculations for Cs_4PbBr_6 due to the strong effect of the SOC on Pb-6p levels. Note that the PBE band gaps are underestimated. (d) Partial density contours of the hole (i) and the electron (ii) in a relaxed exciton in $(C_4N_2H_{14}Br)_4SnBr_6$; (i) and (ii) are viewed from the directions of axes a and b, respectively. The hole localization in (i) results in a decrease of the four planar Sn-Br bonds by 9.9% in average while the electron localization in (ii) results in an increase of the two vertical Sn-Br bonds by 19.8% in average. The Sn and the Br atoms are represented by the red and the blue balls. Reprinted with permission from ref. [208] Copyright 2018, The Royal Society of Chemistry. (e) The configuration coordinate diagram of exciton excitation and emission. The ground-state and the relaxed excited-state structures of the seesaw-structured $(SnBr_4)^{2-}$ anion are shown in (i) and (ii), respectively. The partial densities of the electron and the hole in the exciton are shown in (iii) and (iv), respectively. The Sn and the Br atoms are represented by the red and the blue balls. Reprinted with permission from ref. [135] Copyright 2018, Wiley-VCH. (f) Calculated exciton excitation and emission energies in several 0D and 1D metal halides compared with the experimental values. Following the Franck-Condon principle, the exciton excitation and emission energies were obtained by calculating the total energy differences between the excited and the ground states using PBE0-optimized ground-state and excited-state structures, respectively. The SOC is included in the calculations for the Pb compounds. (For interpretation of the references to colour in this figure legend, the reader is referred to the web version of this article).

emission was attributed to strongly bound excitons localized on the Eu^{2+} ion [218]. Furthermore, Tan and coworkers observed blue emission centered at 455 nm by doping Bi^{3+} ion in the non-emissive Cs_2SnCl_6 crystal lattice. The observed emission displayed large Stokes-shift and a high PLQE of ~80%. They also concluded that there is no energy transfer from the host to the dopant and that the large Stokes-shift is a result of exciton self-trapping. The 0D metal halide hybrid was used, along with a commercial yellow phosphor, to fabricate a down-conversion white LED with good CIE chromaticity coordinates [219].

From the point of theoretical calculation, the 0D metal halide hybrids are essentially molecular crystals, resembling the Zintl-phase compounds [220]. The size of organic or inorganic cations determines the strength of the electronic coupling between the metal halide clusters. Fig. 19 a–c shows the electronic band structures and DOS for three 0D metal halide hybrids, i.e., $(C_4N_2H_{14}Br)_4SnBr_6$, $(C_4N_2H_{14}I)_4SnI_6$, and Cs_4PbBr_6 [208]. The large organic cations in the hybrid organic-inorganic halides $(C_4N_2H_{14}X)_4SnX_6$ (X = Br, I) reduces the electronic coupling among inorganic SnX_6 octahedra, resulting in nearly flat conduction and valence bands made up of metal-halide states; whereas in all-inorganic Cs_4PbBr_6, the band dispersion is more significant due to the relatively small Cs^+ cations. The electronic structure calculation of 0D $(C_9NH_{20})_2SnBr_4$, in which seesaw shaped $SnBr_4^{2-}$ are separated by large $C_9NH_{20}^+$ organic cations, also shows nearly flat metal-halide-derived conduction and valence bands due to the negligible coupling between metal halide species [135].

The localized electronic states in 0D metal halide hybrids, as evidenced by the small dispersion of the electronic bands, lead to strong exciton localization and relaxation. The large calculated STE binding energies, which is relative to free electrons and holes, indicate that the free electrons and holes do not exist at room temperature in these

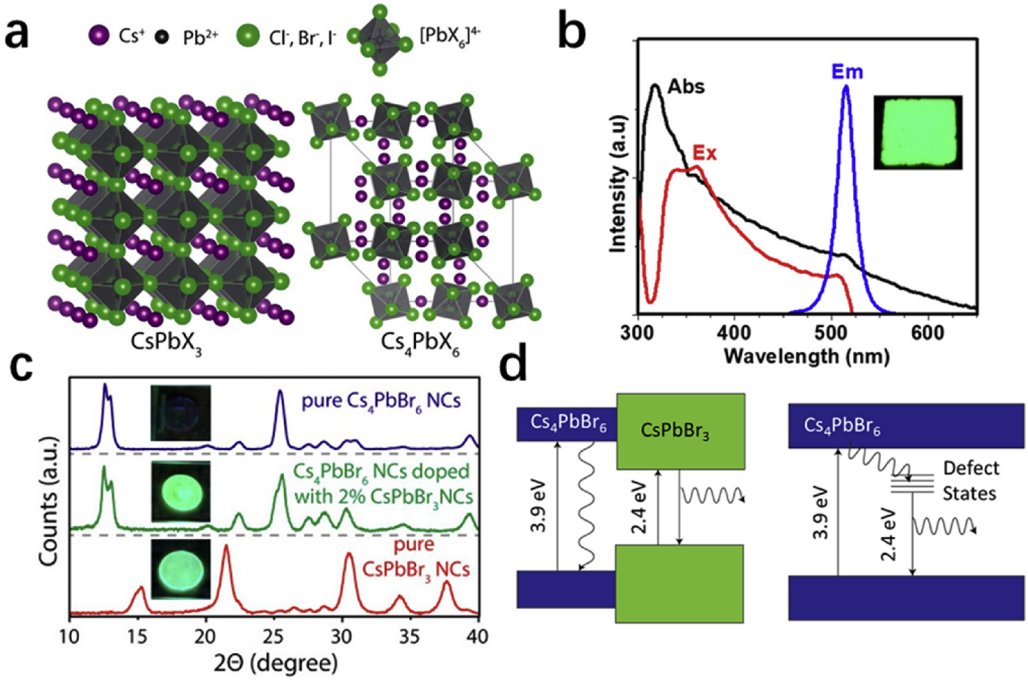

Fig. 20. a) Crystal structure of 3D $CsPbX_3$ (left) and 0D Cs_4PbX_6 (right) where X is a halide ion. Reprinted with permission from ref. [224] Copyright 2018, American Chemical Society. b) Absorption, photoluminescence excitation and emission spectra of Cs_4PbBr_6 micro-disks. Reprinted with permission from ref. [233] Copyright 2017, American Chemical Society. c) Band diagram schematic for emission from $CsPbBr_3$ NC impurity phases (left) and defect states (right); d) XRD pattern of pure Cs_4PbBr_6, 2% $CsPbBr_3$ NCs doped Cs_4PbBr_6 and pure $CsPbBr_3$ NCs illustrating the absence of diffraction peaks attributable to $CsPbBr_3$ even after impurity doping. Reprinted with permission from ref. [225] Copyright 2017, American Chemical Society.

compounds. The STE formation is accompanied by strong excited-state structural relaxation. Fig. 19d shows the structure and the partial charge densities of the electron and hole for the STE in $(C_4N_2H_{14}Br)_4SnBr_6$. The exciton localization at one $SnBr_6$ octahedron results in the shortening of the four planar Sn-Br bonds (by 9.9%) and the elongation of the two vertical Sn-Br bonds (by 19.8%) [208]. Fig. 19e shows another example, i.e., the exciton localization at the seesaw-structured $SnBr_4$ in $(C_9NH_{20})_2SnBr_4$ [135]. Here, the exciton localization transforms the seesaw structure into a nearly planar structure. The strong exciton relaxation leads to large Stokes shifts in these 0D compounds. Fig. 19f shows the calculated exciton excitation and emission energies as well as the corresponding experimental values for several 0D and 1D metal halide hybrids. The good agreement between the calculated and measured values validated the hybrid functional PBE0 calculations of exciton properties in these metal halide hybrids. Among them, Cs_4PbBr_6 has the smallest Stokes shift; this is because of the relatively small Cs^+ cations and the resulting compact crystal structure that limits the extent of the local structural distortion. In contrast, the 0D hybrid organic-inorganic metal halide hybrids have large organic cations and large interstitial space that allows more substantial excited-state structural relaxation.

3.3.2. *The controversial case of 0D perovskite Cs_4PbBr_6*

Cs_4PbBr_6, a "zero-dimensional" phase with disconnected $[PbBr_6]^{4-}$ octahedra coordinated to Cs^+ ions (Fig. 20a), has been the subject of much attention after reestablished interest in lead halide perovskites. Recently, controversial reports on 0D Cs_4PbBr_6 have sparked debates on the origin of the observed photophysical properties. There is a consensus on the wide energy bandgap and emission in the UV region from the direct band [206,221–225]. However, the controversy over the origin of green emission from some of the 0D Cs_4PbBr_6 samples remains, with many believing that it comes from $CsPbBr_3$ NCs present in Cs_4PbBr_6, while others considering the presence of defect-induced sub-bandgap states (V_{Br}^+) as the origin.

A number of green emitting 0D Cs_4PbBr_6 materials have been reported to exhibit high PLQE (40–65%), narrow emission band (fwhm of ~22 nm), and small Stokes shift [226–228]. The absorption, photoluminescence excitation and emission spectra of emissive Cs_4PbBr_6 microdisks are shown in Fig. 20b. De Bastiani and coworkers claimed that they successfully synthesized pure Cs_4PbBr_6 because the powder XRD patterns that attribute to $CsPbBr_3$ NC phases were not recorded [222]. Also, no distinguishing features were observed when comparing the electron diffraction patterns of emissive and non-emissive Cs_4PbBr_6. However, Akkerman and coworkers synthesized nearly monodisperse Cs_4PbBr_6 NCs, which were found to be non-emissive in the visible range and weakly emissive in the UV region (around 380 nm) [225]. In this work, the authors also doped 2 M % (0.5 wt%) of $CsPbBr_3$ NCs in the non-emissive Cs_4PbBr_6 which resulted in strong green emission. Interestingly, powder XRD on impurity doped Cs_4PbBr_6 did not result in diffraction peaks ascribable to $CsPbBr_3$ phases as can be observed from Fig. 20c. They, therefore, concluded that diffraction peaks from $CsPbBr_3$ NCs doped Cs_4PbBr_6 are not likely to appear distinguishable, because broadening of the diffraction peaks is unavoidable for NCs and the small number of impurity results in low diffraction intensity. On the other hand, since halide vacancies are commonly present in metal halide perovskites, the presence of defect-induced sub-bandgap states was proposed as the origin of green emission for 0D Cs_4PbBr_6 [229]. Fig. 20d schematically shows the band structure of Cs_4PbBr_6 with $CsPbBr_3$ NC impurities and sub-bandgap states caused by defects. However, the calculated Stokes shift of 0.79 eV of the bound exciton at V_{Br}^+ is substantially larger than that observed in green-emitting Cs_4PbBr_6 (< 0.1 eV) [208]. This large Stokes shift is reasonable because the strong exciton localization should lead to structural distortion and large Stokes shift. These calculations do not support the V_{Br}^+ - induced green emission mechanism. Moreover, the calculated emission energy of the bound exciton at Pb_{Cs}^{2+} is 0.99 eV, which is too small to account for the green emission (2.3–2.4 eV) [208]. Manna group presented an argument in a recent perspective for the presence of defect states in Cs_4PbBr_6 phase [224]. Although halogen vacancies are abundant in perovskites, these vacancies are known to form deep trap states which could significantly reduce PLQE. Moreover, emission from defect states are characteristically broad, strongly Stokes-shifted and display long lifetimes, as observed in corrugated-2D, 1D, and 0D organic metal halide hybrids discussed above. However, the green emission from many 0D Cs_4PbBr_6 materials is narrow with small Stokes-shift and short lifetime. In addition, the presence of defect states does not adequately address the absorption peak in the visible region observed for Cs_4PbBr_6 "pure" phases.

Although DFT calculations of the electronic band structure of Cs_4PbBr_6 (based on the PBE calculation including the SOC) have been reported to agree with each other, [208,222,223] the claim of the good agreement between the experimentally observed peak exciton excitation energy and the calculated band gap, by PBE without the SOC or Heyd-Scuseria-Ernzerhof (HSE) hybrid functional with the SOC [206,221,223,225,230–232], is misleading because the single-particle energy band gap of Cs_4PbBr_6 obtained without considering the electron-hole binding cannot be compared with the measured excitonic absorption due to the strong exciton binding in Cs_4PbBr_6. Also, the PBE calculation of the band gap of Cs_4PbBr_6 without including the SOC is incorrect. Solving the Bethe-Salpeter equation based on the PBE calculation including the SOC yielded the excitonic absorption energy of 3.3 eV [223]. Directly calculating the total energy difference between the excited and the ground state (both in the ground-state structure following the Franck-Condon principle) by applying the constrained DFT for the excited state combined with the PBE0 hybrid functionals (including the SOC) results in the exciton excitation energy of 3.63 eV (Fig. 19c), [208] in good agreement with the experimental value (3.95–4 eV) [206,221,225]. (In the constrained DFT calculation, the electron occupation is constrained to create a hole in the valence band and an electron in the conduction band.) The exciton emission energy was calculated to be 3.05 eV [208] (PBE0-SOC calculation) and 3.2 eV [232] (HSE-SOC calculation) by taking the energy difference between the excited and the ground states in the excited-state structure, which are in good agreement with the experimentally measured value of 3.31 eV (375 nm) [206]. These results suggest that the observed UV emission at 375 nm is the intrinsic exciton emission and that the frequently observed green emission is not due to the STE in Cs_4PbBr_6. According to experimental and theoretical results, the green emission of Cs_4PbBr_6 is likely from the contamination by $CsPbBr_3$ nanocrystal-like impurities rather than Cs_4PbBr_6 or Br^- vacancy [208,224]. To our point of view, since the Cs^+ cations might be too small to have individual metal halide octahedra completely isolated from each other without electronic band formation, Cs_4PbBr_6 might not be considered to have a perfect 0D structure like what is present in other 0D organic metal halide hybrids.

4. Stability

Stability is a critical issue that should be taken seriously for the applications of organic-inorganic metal halide hybrids. The stability of 3D metal halide perovskites has been intensively studied since it is considered as the major limiting factor for the commercialization of perovskite solar cells. For example, it was found that $MAPbI_3$ is sensitive to moisture, oxygen, UV irradiation, electric field and heat which synergistically result in the degradation of the material and deteriorated device performance (Fig. 21). The degradation of $MAPbI_3$ is mainly attributed to its intrinsic chemical instability nature, which could form an equilibrium with the decomposed volatile products such as CH_3NH_3I, CH_3NH_2, and HI [234]. Exposure of $MAPbI_3$ to moisture leads to the formation of hydrolyzed phases and permanent loss of the water-soluble small molecule species that drives the decomposition reaction forward [235,236]. With the assist of UV light, oxygen could interact with the photoexcited electron to form superoxide (O_2^-) which further reacts with the organic components [237,238]. Ion migration is another important factor in accounting for the instability of $MAPbI_3$ under operation. Hopping of organic cations between the neighboring lattice sites is facilitated via defect states [239]. Ion migration was also found to occur in mixed 3D metal halide perovskites such as $MAPbBr_xI_{3-x}$ under illumination, resulting in phase separation into iodine-rich and iodine-poor phase [240]. The migration of ions requires an activation energy to overcome the energy barrier between two lattice sites, which is largely dependent on temperature, electric field, light, etc. [241]. Other than causing the expansion of the crystal lattice for easier ion migration, raising temperature can also result in the phase transition of 3D materials. For instance, $MAPbI_3$ transforms from tetragonal to cubic phase at around 57°C, resulting in significant changes in photophysical properties [242]. Various efforts have been made to increase the stability of 3D metal halide perovskites and alleviate the effects of the ambient condition, which include chemical and structural engineering, device architecture optimizing, device protection, encapsulation, etc. as summarized in several previous accounts [243–246].

Low dimensional organic metal halide perovskites and hybrids have been shown to exhibit better stability than their 3D analogs. This is mainly due to the incorporation of bulky organic cations which dynamically stabilize the metal halide nanostructures and separate them from outside environment. Therefore, the large organic cations can also be regarded as surface passivating components protecting metal halide quantum materials from moisture, oxygen etc. Based on the computational study, Quan and coworkers suggested that quasi-2D perovskites with a chemical formula of $(C_8H_9NH_3)_2(CH_3NH_3)_{n-1}Pb_nI_{3n+1}$ have increased stability along with the decreased n value due to the increased formation energy from the precursors [247]. Lin and coworkers found that ionic conductivity of quasi-2D $(BA)_2(MA)_3Pb_4I_{13}$ was not observed, suggesting suppressed ion migration at temperatures up to 330 K both in dark and under illumination [248]. The higher stability of 2D organic metal halide hybrids confers their applications in stable electronic

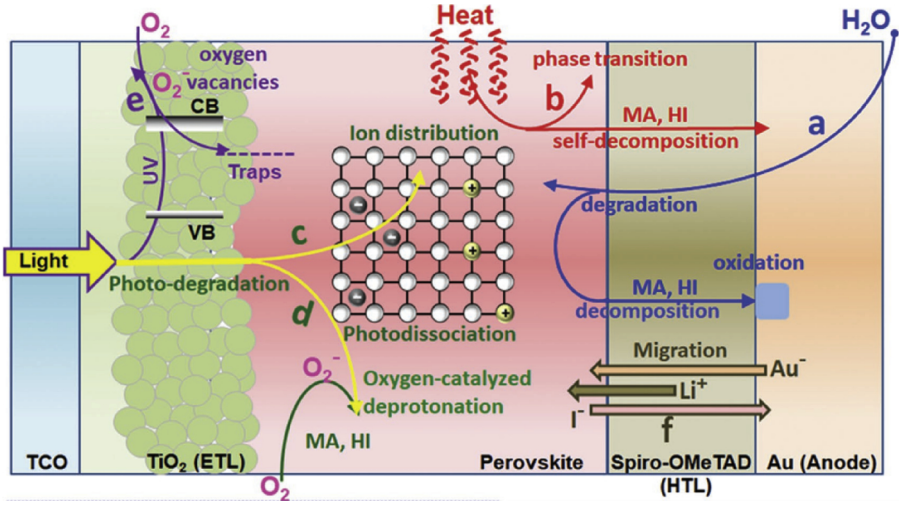

Fig. 21. Schematically illustration of six representative degradation pathways induced by moisture, heat, and light in a regular perovskite solar cell. Reprinted with permission from ref. [246] Copyright 2018, Wiley-VCH.

devices. The study by Tsai and coworkers demonstrated the long-term stability of 2D Ruddlesden-Popper perovskite in solar cell, in which $(BA)_2(MA)_3Pb_4I_{13}$ based device remain almost unchanged under AM1.5 G (standard solar spectrum) illumination and 65% humidity for over 2,250 h when the devices are encapsulated, while PCE of 3D $MAPbI_3$ dropped to about 50% under the same condition [146]. Unencapsulated 2D perovskite devices retain over 60% of their efficiency for over 2,250 h under constant, standard (AM1.5 G) illumination, and exhibit greater tolerance to 65% relative humidity than their 3D counterparts. LED devices based on 2D organic metal halide components fabricated by Wang and coworkers showed a significant improvement (by two orders of magnitudes) of duration than that based on a 3D material [170]. Another compound, N-(3-aminopropyl)imidazole tetrachloro-lead with corrugated-2D structure was observed to exhibit nearly identical photoluminescent properties after being stored under ambient condition for one week, indicating possible improvement in stability for the corrugated 2D family [187].

1D and 0D organic metal halide hybrids have the potential to act as down-conversion light emitters. Therefore, characterization of their stability mainly focused on the aspects of thermal and photo-stability which are important for the UV-excited LED devices. For example, 1D bluish-white light emitting material $C_4N_2H_{14}PbBr_4$ was reported to have moderate photostability in the air with a slow decrease of emission intensity under continuous high-power Hg lamp irradiation [134]. Peng and coworkers reported a similar 1D organic metal halide with a chiral organic cation which exhibits good photostability and environment stability evidenced by negligible photoluminescence changes after irradiation for 48 h or after exposure to ambient conditions for two weeks [249]. In contrast, a tin-based 1D material $C_4N_2H_{14}SnBr_6$ is not stable under UV illumination and can undergo a photoinduced structural transformation into 0D $(C_4N_2H_{14}Br)_4SnBr_6$, suggesting that 0D structure is more energetically stable than the 1D counterpart [199]. For 0D organic metal halide hybrids, most of them exhibit great photo- and thermal-stability under the ambient and operation condition. For example, $(C_4N_2H_{14}Br)_4SnBr_6$, $(C_4N_2H_{14}I)_4SnI_6$ and $(C_9NH_{20})_2SbCl_5$ are resistive to continuous high-power mercury lamp irradiation (150 mW cm^{-2}) and they do not decompose until 200 °C [136]. The 0D organic metal halide $(Ph_4P)_2MnBr_4$ was also reported to show electroluminescence properties with a good thermal stability [210]. Although low dimensional organic metal halide hybrids are relatively more stable than 3D ABX_3 perovskites, they are still less stable as compared to conventional inorganic semiconductors. Also, the detailed degradation mechanisms for low dimensional organic metal halide hybrids have not been fully understood due to the limited research on material and device stability. Based on our current understanding, the organic moiety plays an important role in stabilizing the material, not only by isolating the photoactive metal halide nanostructures from outside molecules, but also by interacting with other components in the crystal lattice at both ground states and excited states. Choosing appropriate metals which are inert to air such as lead and bismuth would also help to reduce degradation pathways. The factors, including complete protection of the quantum nanostructures, high intrinsic chemical stability, strong ionic and Van de Waals interaction and high formation energy for the bulk crystal, stabilized excited states, are critical requirements to achieve high thermal and photo stabilities of organic metal halide hybrids.

5. Remarks and prospects

Organic metal halide hybrids with low dimensionalities have gained a lot of research attention over last few years in various aspects, i.e. effective tuning of dimensionality, discovering new members for each category, understanding basic mechanisms accounting for their physical properties, fabrication of solar cells, LEDs, and other devices. Their structural tunability and versatile structural-property relationships indicate that there is still a large space for material development and property tuning. Several developed organic metal halide hybrids that are not limited to the conventional 2D to 0D categories with unique properties (e.g. 1D nanotube, 0D cluster) have already emerged to demonstrate the infinite possibilities of this class of materials [200,250]. Here are several challenges and issues that we believe need to be addressed in the future to further advance the research in this field:

1 The development of new organic metal halide hybrids still mainly relies on the trial-and-error synthetic method. Can we develop guidelines for the precise control of the dimensionality, nanostructure, and crystallinity of organic metal halide hybrids? For instance, can other metal halide polyhedrons, e.g. tetrahedrons, pyramids, etc. be used as building blocks to assemble 1D, 2D, and 3D structures? Can the size of metal halide clusters be well controlled to bridge molecules (molecular orbital theory) to crystals (electronic band theory)? Can we develop computational methods to predict how the organic and inorganic components self-assemble to form bulk crystals? Are there any other synthetic methods besides solution process?
2 Although many photophysical and electronic properties of organic metal halide hybrids can be explained by the established theories and computational studies, there is still a huge gap to fully understand the kinetics and dynamics of the energy diagram, especially on the excited states. How the topology of the metal halide framework, the interaction between organic and inorganic moieties affect the ground- and excited-state properties need to be better understood.
3 In terms of applications, organic metal halide hybrids are still not stable enough to compete with inorganic semiconductors or even organic semiconductors. It is, therefore, necessary to further increase the stability of these materials by investigating the detailed degradation mechanisms and study how moisture, oxygen, heat, and other factors will affect. Moreover, how these materials respond to other stimulations such as pressure, magnetic field, polarized lights, etc. have not been well studied. Other potential applications based on these characteristics, such as solar concentrators, phonon transport, magnetic storage, light guiding, scintillators, and so on could be promising future research directions.

Acknowledgements

The authors thank the support from the National Science Foundation (NSF) (DMR-1709116), the Air Force Office of Scientific Research (AFOSR) (17RT0906), and Florida State University Office of Research. X. S. acknowledges the funding support from China Postdoctoral Science Foundation (No. 2014M551595). M. D. was supported by the U.S. Department of Energy, Office of Science, Basic Energy Sciences, Materials Sciences and Engineering Division.

References

[1] C.K. MØLLER, Nature 182 (1958) 1436.
[2] D. Weber, Z. Naturforsch. 33b (1978) 862–865.
[3] D.B. Mitzi, C.A. Feild, W.T.A. Harrison, A.M. Guloy, Nature 369 (1994) 467–469.
[4] C. Kagan, D. Mitzi, C. Dimitrakopoulos, Science 286 (1999) 945–947.
[5] D.B. Mitzi, K. Chondroudis, C.R. Kagan, IBM J. Res. Dev. 45 (2001) 29–45.
[6] M.A. Green, A. Ho-Baillie, H.J. Snaith, Nat. Photonics 8 (2014) 506.
[7] A. Kojima, K. Teshima, Y. Shirai, T. Miyasaka, J. Am. Chem. Soc. 131 (2009) 6050–6051.
[8] Z.-K. Tan, R.S. Moghaddam, M.L. Lai, P. Docampo, R. Higler, F. Deschler, M. Price, A. Sadhanala, L.M. Pazos, D. Credgington, F. Hanusch, T. Bein, H.J. Snaith, R.H. Friend, Nat. Nanotechnol. 9 (2014) 687–692.
[9] L. Protesescu, S. Yakunin, M.I. Bodnarchuk, F. Krieg, R. Caputo, C.H. Hendon, R.X. Yang, A. Walsh, M.V. Kovalenko, Nano Lett. 15 (2015) 3692–3696.
[10] F. Zhang, H. Zhong, C. Chen, X.-g. Wu, X. Hu, H. Huang, J. Han, B. Zou, Y. Dong, ACS Nano 9 (2015) 4533–4542.
[11] Q.A. Akkerman, V. D'Innocenzo, S. Accornero, A. Scarpellini, A. Petrozza, M. Prato, L. Manna, J. Am. Chem. Soc. 137 (2015) 10276–10281.
[12] L.C. Schmidt, A. Pertegás, S. González-Carrero, O. Malinkiewicz, S. Agouram, G. Mínguez Espallargas, H.J. Bolink, R.E. Galian, J. Pérez-Prieto, J. Am. Chem. Soc. 136 (2014) 850–853.

[13] P. Tyagi, S.M. Arveson, W.A. Tisdale, J. Phys. Chem. Lett. 6 (2015) 1911–1916.
[14] L.T. Dou, A.B. Wong, Y. Yu, M.L. Lai, N. Kornienko, S.W. Eaton, A. Fu, C.G. Bischak, J. Ma, T.N. Ding, N.S. Ginsberg, L.W. Wang, A.P. Alivisatos, P.D. Yang, Science 349 (2015) 1518–1521.
[15] D. Zhang, S.W. Eaton, Y. Yu, L. Dou, P. Yang, J. Am. Chem. Soc. 137 (2015) 9230–9233.
[16] S. Sun, D. Yuan, Y. Xu, A. Wang, Z. Deng, ACS Nano 10 (2016) 3648–3657.
[17] I.C. Smith, E.T. Hoke, D. Solis-Ibarra, M.D. McGehee, H.I. Karunadasa, Angew. Chem. Int. Ed. 53 (2014) 11232–11235.
[18] M.D. Smith, A. Jaffe, E.R. Dohner, A.M. Lindenberg, H.I. Karunadasa, Chem. Sci. 8 (2017) 4497–4504.
[19] E.R. Dohner, A. Jaffe, L.R. Bradshaw, H.I. Karunadasa, J. Am. Chem. Soc. 136 (2014) 13154–13157.
[20] E.R. Dohner, E.T. Hoke, H.I. Karunadasa, J. Am. Chem. Soc. 136 (2014) 1718–1721.
[21] Z. Yuan, C. Zhou, J. Messier, Y. Tian, Y. Shu, J. Wang, Y. Xin, B. Ma, Adv. Opt. Mater. 4 (2016) 2009–2015.
[22] C. Zhou, H. Lin, Y. Tian, Z. Yuan, R. Clark, B. Chen, L.J. van de Burgt, J.C. Wang, Y. Zhou, K. Hanson, Q.J. Meisner, J. Neu, T. Besara, T. Siegrist, E. Lambers, P. Djurovich, B. Ma, Chem. Sci. 9 (2018) 586–593.
[23] H. Huang, L. Polavarapu, J.A. Sichert, A.S. Susha, A.S. Urban, A.L. Rogach, NPG Asia Mater. 8 (2016) e328.
[24] Y. Bekenstein, B.A. Koscher, S.W. Eaton, P. Yang, A.P. Alivisatos, J. Am. Chem. Soc. 137 (2015) 16008–16011.
[25] J. Shamsi, Z. Dang, P. Bianchini, C. Canale, F.D. Stasio, R. Brescia, M. Prato, L. Manna, J. Am. Chem. Soc. 138 (2016) 7240–7243.
[26] Z. Yuan, Y. Shu, Y. Tian, Y. Xin, B. Ma, Chem. Commun. (Camb.) 51 (2015) 16385–16388.
[27] J.A. Sichert, Y. Tong, N. Mutz, M. Vollmer, S. Fischer, K.Z. Milowska, R. Garcia Cortadella, B. Nickel, C. Cardenas-Daw, J.K. Stolarczyk, A.S. Urban, J. Feldmann, Nano Lett. 15 (2015) 6521–6527.
[28] Q.A. Akkerman, S.G. Motti, A.R. Srimath Kandada, E. Mosconi, V. D'Innocenzo, G. Bertoni, S. Marras, B.A. Kamino, L. Miranda, F. De Angelis, A. Petrozza, M. Prato, L. Manna, J. Am. Chem. Soc. 138 (2016) 1010–1016.
[29] S.T. Ha, X.F. Liu, Q. Zhang, D. Giovanni, T.C. Sum, Q.H. Xiong, Adv. Opt. Mater. 2 (2014) 838–844.
[30] Y. Ling, Z. Yuan, Y. Tian, X. Wang, J.C. Wang, Y. Xin, K. Hanson, B. Ma, H. Gao, Adv. Mater. 28 (2016) 305–311.
[31] Q. Zhang, R. Su, X. Liu, J. Xing, T.C. Sum, Q. Xiong, Adv. Funct. Mater. 26 (2016) 6238–6245.
[32] Y. Zhao, K. Zhu, J. Am. Chem. Soc. 136 (2014) 12241–12244.
[33] C.X. Huo, B. Cai, Z. Yuan, B.W. Ma, H.B. Zeng, Small Methods 1 (2017).
[34] X. Qi, Y. Zhang, Q. Ou, S.T. Ha, C.W. Qiu, H. Zhang, Y.B. Cheng, Q. Xiong, Q. Bao, Small 14 (2018) 1800682.
[35] E. Shi, Y. Gao, B.P. Finkenauer, Akriti, A.H. Coffey, L. Dou, Chem. Soc. Rev. 47 (2018) 6046–6072.
[36] S. Chen, G. Shi, Adv. Mater. 29 (2017) 1605448.
[37] W. Zhang, G.E. Eperon, H.J. Snaith, Nat. Energy 1 (2016) 16048.
[38] J.S. Manser, J.A. Christians, P.V. Kamat, Chem. Rev. 116 (2016) 12956–13008.
[39] H.C. Kwon, W. Yang, D. Lee, J. Ahn, E. Lee, S. Ma, K. Kim, S.C. Yun, J. Moon, ACS Nano 12 (2018) 4233–4245.
[40] W.N. Du, S. Zhang, J. Shi, J. Chen, Z.Y. Wu, Y. Mi, Z. Liu, Y.Z. Li, X.Y. Sui, R. Wang, X.H. Qiu, T. Wu, Y.F. Xiao, Q. Zhang, X.F. Liu, ACS Photonics 5 (2018) 2051–2059.
[41] X.Z. Xu, X.J. Zhang, W. Deng, J.S. Jie, X.H. Zhang, Small Methods 2 (2018) 1700340.
[42] A.A. Petrov, N. Pellet, J.Y. Seo, N.A. Belich, D.Y. Kovalev, A.V. Shevelkov, E.A. Goodilin, S.M. Zakeeruddin, A.B. Tarasov, M. Graetzel, Chem. Mater. 29 (2017) 587–594.
[43] S.T. Ha, R. Su, J. Xing, Q. Zhang, Q.H. Xiong, Chem. Sci. 8 (2017) 2522–2536.
[44] E. Horvath, M. Spina, Z. Szekrenyes, K. Kamaras, R. Gaal, D. Gachet, L. Forro, Nano Lett. 14 (2014) 6761–6766.
[45] D.D. Zhang, S.W. Eaton, Y. Yu, L.T. Dou, P.D. Yang, J. Am. Chem. Soc. 137 (2015) 9230–9233.
[46] Y.P. Zhang, J.Y. Liu, Z.Y. Wang, Y.Z. Xue, Q.D. Ou, L. Polavarapu, J.L. Zheng, X. Qi, Q.L. Bao, Chem. Commun. (Camb.) 52 (2016) 13637–13655.
[47] X. Yang, J. Wu, T. Liu, R. Zhu, Small Methods 2 (2018) 1800110.
[48] J.N. Chen, S.S. Zhou, S.Y. Jin, H.Q. Li, T.Y. Zhai, J. Mater. Chem. C Mater. Opt. Electron. Devices 4 (2016) 11–27.
[49] Y.P. Zhang, Y.S. Wang, Z.Q. Xu, J.Y. Liu, J.C. Song, Y.Z. Xue, Z.Y. Wang, J.L. Zheng, L.C. Jiang, C.X. Zheng, F.Z. Huang, B.Q. Sun, Y.B. Cheng, Q.L. Bao, ACS Nano 10 (2016) 7031–7038.
[50] J. Chen, Y.P. Fu, L. Samad, L.N. Dang, Y.Z. Zhao, S.H. Shen, L.J. Guo, S. Jin, Nano Lett. 17 (2017) 460–466.
[51] J. Xing, X.F. Liu, Q. Zhang, S.T. Ha, Y.W. Yuan, C. Shen, T.C. Sum, Q.H. Xiong, Nano Lett. 15 (2015) 4571–4577.
[52] M. Kulbak, D. Cahen, G. Hodes, J. Phys. Chem. Lett. 6 (2015) 2452–2456.
[53] Y. Wang, X.M. Li, J.Z. Song, L. Xiao, H.B. Zeng, H.D. Sun, Adv. Mater. 27 (2015) 7101–7108.
[54] L. Huang, Q.G. Gao, L.D. Sun, H. Dong, S. Shi, T. Cai, Q. Liao, C.H. Yan, Adv. Mater. 30 (2018) 1800596.
[55] K. Park, J.W. Lee, J.D. Kim, N.S. Han, D.M. Jang, S. Jeong, J. Park, J.K. Song, J. Phys. Chem. Lett. 7 (2016) 3703–3710.
[56] E. Oksenberg, E. Sanders, R. Popovitz-Biro, L. Houben, E. Joselevich, Nano Lett. 18 (2018) 424–433.
[57] M. Shoaib, X.H. Zhang, X.X. Wang, H. Zhou, T. Xu, X. Wang, X.L. Hu, H.W. Liu, X.P. Fan, W.H. Zheng, T.F. Yang, S.Z. Yang, Q.L. Zhang, X.L. Zhu, L.T. Sun, A.L. Pan, J. Am. Chem. Soc. 139 (2017) 15592–15595.
[58] X.X. Wang, M. Shoaib, X. Wang, X.H. Zhang, M. He, Z.Y. Luo, W.H. Zheng, H.L. Li, T.F. Yang, X.L. Zhu, L.B. Ma, A.L. Pan, ACS Nano 12 (2018) 6170–6178.
[59] H. Zhou, S.P. Yuan, X.X. Wang, T. Xu, X. Wang, H.L. Li, W.H. Zheng, P. Fang, Y.Y. Li, L.T. Sun, A.L. Pan, ACS Nano 11 (2017) 1189–1195.
[60] X.X. Wang, H. Zhou, S.P. Yuan, W.H. Zheng, Y. Jiang, X.J. Zhuang, H.J. Liu, Q.L. Zhang, X.L. Zhu, X. Wang, A.L. Pan, Nano Res. 10 (2017) 3385–3395.
[61] A.Z. Pan, M.J. Jurow, F. Qiu, J. Yang, B.Y. Ren, J.J. Urban, L. He, Y. Liu, Nano Lett. 17 (2017) 6759–6765.
[62] H.M. Zhu, Y.P. Fu, F. Meng, X.X. Wu, Z.Z. Gong, Q. Ding, M.V. Gustafsson, M.T. Trinh, S. Jin, X.Y. Zhu, Nat. Mater. 14 (2015) 636–642.
[63] J.H. Im, J.S. Luo, M. Franckevicius, N. Pellet, P. Gao, T. Moehl, S.M. Zakeeruddin, M.K. Nazeeruddin, M. Gratzel, N.G. Park, Nano Lett. 15 (2015) 2120–2126.
[64] A.B. Wong, M.L. Lai, S.W. Eaton, Y. Yu, E. Lin, L. Dou, A. Fu, P.D. Yang, Nano Lett. 15 (2015) 5519–5524.
[65] K. Hong, Q.V. Le, S.Y. Kim, H.W. Jang, J. Mater. Chem. C Mater. Opt. Electron. Devices 6 (2018) 2189–2209.
[66] H. Deng, D.D. Dong, K.K. Qiao, L.L. Bu, B. Li, D. Yang, H.E. Wang, Y.B. Cheng, Z.X. Zhao, J. Tanga, H.S. Song, Nanoscale 7 (2015) 4163–4170.
[67] H. Deng, X.K. Yang, D.D. Dong, B. Li, D. Yang, S.J. Yuan, K.K. Qiao, Y.B. Cheng, J. Tang, H.S. Song, Nano Lett. 15 (2015) 7963–7969.
[68] L. Gao, K. Zeng, J.S. Guo, C. Ge, J. Du, Y. Zhao, C. Chen, H. Deng, Y.S. He, H.S. Song, G.D. Niu, J. Tang, Nano Lett. 16 (2016) 7446–7454.
[69] J. Zhang, X.K. Yang, H. Deng, K.K. Qiao, U. Farooq, M. Ishaq, F. Yi, H. Liu, J. Tang, H.S. Song, Nano-Micro Lett. 9 (2017) 36.
[70] S. Wang, K.Y. Wang, Z.Y. Gu, Y.J. Wang, C. Huang, N.B. Yi, S.M. Xiao, Q.H. Song, Adv. Opt. Mater. 5 (2017) 1700023.
[71] M. Spina, M. Lehmann, B. Nafradi, L. Bernard, E. Bonvin, R. Gaal, A. Magrez, L. Forro, E. Horvath, Small 11 (2015) 4824–4828.
[72] Y.P. Fu, F. Meng, M.B. Rowley, B.J. Thompson, M.J. Shearer, D.W. Ma, R.J. Hamers, J.C. Wright, S. Jin, J. Am. Chem. Soc. 137 (2015) 5810–5818.
[73] W. Tian, C. Zhao, J. Leng, R. Cui, S. Jin, J. Am. Chem. Soc. 137 (2015) 12458–12461.
[74] R. Xiao, Y. Hou, Y.P. Fu, X.Y. Peng, Q. Wang, E. Gonzalez, S. Jin, D. Yu, Nano Lett. 16 (2016) 7710–7717.
[75] X.X. He, P. Liu, S.N. Wu, Q. Liao, J.N. Yao, H.B. Fu, J. Mater. Chem. C Mater. Opt. Electron. Devices 5 (2017) 12707–12713.
[76] W.M. Tian, J. Leng, C.Y. Zhao, S.Y. Jin, J. Am. Chem. Soc. 139 (2017) 579–582.
[77] Y.X. Wang, R.X. Lin, P.C. Zhu, Q.H. Zheng, Q.J. Wang, D.Y. Li, J. Zhu, Nano Lett. 18 (2018) 2772–2779.
[78] Y.P. Fu, H.M. Zhu, A.W. Schrader, D. Liang, Q. Ding, P. Joshi, L. Hwang, X.Y. Zhu, S. Jin, Nano Lett. 16 (2016) 1000–1008.
[79] Y.P. Fu, H.M. Zhu, C.C. Stoumpos, Q. Ding, J. Wang, M.G. Kanatzidis, X.Y. Zhu, S. Jin, ACS Nano 10 (2016) 7963–7972.
[80] J.H. Im, I.H. Jang, N. Pellet, M. Gratzel, N.G. Park, Nat. Nanotechnol. 9 (2014) 927–932.
[81] P.C. Zhu, S. Gu, X.P. Shen, N. Xu, Y.L. Tan, S.D. Zhuang, Y. Deng, Z.D. Lu, Z.L. Wang, J. Zhu, Nano Lett. 16 (2016) 871–876.
[82] C.Y. Chang, B.C. Tsai, M.Z. Lin, Y.C. Huang, C.S. Tsao, J. Mater. Chem. A Mater. Energy Sustain. 5 (2017) 22824–22833.
[83] S.W. Wang, S. Yan, M.A. Wang, L. Chang, J.L. Wang, Z. Wang, Sol. Energy Mater. Sol. Cells 167 (2017) 173–177.
[84] R. Singh, S.R. Suranagi, S.J. Yang, K. Cho, Nano Energy 51 (2018) 192–198.
[85] S.W. Eaton, M.L. Lai, N.A. Gibson, A.B. Wong, L.T. Dou, J. Ma, L.W. Wang, S.R. Leone, P.D. Yang, Proc. Natl. Acad. Sci. U. S. A. 113 (2016) 1993–1998.
[86] L. Dou, M.L. Lai, C.S. Kley, Y.M. Yang, C.G. Bischak, D.D. Zhang, S.W. Eaton, N.S. Ginsberg, P.D. Yang, Proc. Natl. Acad. Sci. U. S. A. 114 (2017) 7216–7221.
[87] D.D. Zhang, Y. Yu, Y. Bekenstein, A.B. Wong, A.P. Alivisatos, P.D. Yang, J. Am. Chem. Soc. 138 (2016) 13155–13158.
[88] M. Imran, F. Di Stasio, Z.Y. Dang, C. Canale, A.H. Khan, J. Shamsi, R. Brescia, M. Prato, L. Manna, Chem. Mater. 28 (2016) 6450–6454.
[89] F. Di Stasio, M. Imran, Q.A. Akkerman, M. Prato, L. Manna, R. Krahne, J. Phys. Chem. Lett. 8 (2017) 2725–2729.
[90] D. Amgar, A. Stern, D. Rotem, D. Porath, L. Etgar, Nano Lett. 17 (2017) 1007–1013.
[91] C.Y. Wang, Y.K. Zhang, A.F. Wang, Q. Wang, H.Y. Tang, W. Shen, Z. Li, Z.T. Deng, Chem. Mater. 29 (2017) 2157–2166.
[92] P. Vashishtha, D.Z. Metin, M.E. Cryer, K. Chen, J.M. Hodgkiss, N. Gaston, J.E. Halpert, Chem. Mater. 30 (2018) 2973–2982.
[93] T. Guner, G. Topcu, U. Savaci, A. Genc, S. Turan, E. Sari, M.M. Demir, Nanotechnology 29 (2018) 927–932.
[94] L.J. Chen, C.R. Lee, Y.J. Chuang, Z.H. Wu, C.Y. Chen, J. Phys. Chem. Lett. 7 (2016) 5028–5035.
[95] W.N. Liu, J.J. Zheng, S. Cao, L. Wang, F.M. Gao, K.C. Chou, X.M. Hou, W.Y. Yang, Inorg. Chem. 57 (2018) 1598–1603.
[96] P.V. Kamat, J. Bisquert, J. Buriak, ACS Energy Lett. 2 (2017) 904–905.
[97] M.J. Ashley, M.N. O'Brien, K.R. Hedderick, J.A. Mason, M.B. Ross, C.A. Mirkin, J. Am. Chem. Soc. 138 (2016) 10096–10999.
[98] L.L. Gu, M.M. Tavakoli, D.Q. Zhang, Q.P. Zhang, A. Waleed, Y.Q. Xiao, K.H. Tsui, Y.J. Lin, L. Liao, J.N. Wang, Z.Y. Fan, Adv. Mater. 28 (2016) 9713–9721.
[99] S.Z. Oener, P. Khoram, S. Brittman, S.A. Mann, Q.P. Zhang, Z.Y. Fan, S.W. Boettcher, E.C. Garnett, Nano Lett. 17 (2017) 6557–6563.
[100] A. Waleed, M.M. Tavakoli, L.L. Gu, Z.Y. Wang, D.Q. Zhang, A. Manikandan, Q.P. Zhang, R.J. Zhang, Y.L. Chueh, Z.Y. Fan, Nano Lett. 17 (2017) 523–530.
[101] A. Waleed, M.M. Tavakoli, L.L. Gu, S. Hussain, D.Q. Zhang, S. Poddar, Z.Y. Wang,

R.J. Zhang, Z.Y. Fan, Nano Lett. 17 (2017) 4951–4957.
[102] L.C. Schmidt, A. Pertegas, S. Gonzalez-Carrero, O. Malinkiewicz, S. Agouram, G. Minguez Espallargas, H.J. Bolink, R.E. Galian, J. Perez-Prieto, J. Am. Chem. Soc. 136 (2014) 850–853.
[103] X. Li, Y. Wu, S. Zhang, B. Cai, Y. Gu, J. Song, H. Zeng, Adv. Funct. Mater. 26 (2016) 2435–2445.
[104] S. Wei, Y. Yang, X. Kang, L. Wang, L. Huang, D. Pan, Chem. Commun. (Camb.) 52 (2016) 7265–7268.
[105] Q. Zhou, Z. Bai, W.G. Lu, Y. Wang, B. Zou, H. Zhong, Adv. Mater. 28 (2016) 9163–9168.
[106] D.N. Dirin, L. Protesescu, D. Trummer, I.V. Kochetygov, S. Yakunin, F. Krumeich, N.P. Stadie, M.V. Kovalenko, Nano Lett. 16 (2016) 5866–5874.
[107] L. Zhao, Y.-W. Yeh, N.L. Tran, F. Wu, Z. Xiao, R.A. Kerner, Y.L. Lin, G.D. Scholes, N. Yao, B.P. Rand, ACS Nano 11 (2017) 3957–3964.
[108] Z. Xiao, R.A. Kerner, L. Zhao, N.L. Tran, K.M. Lee, T.-W. Koh, G.D. Scholes, B.P. Rand, Nat. Photonics 11 (2017) 108–115.
[109] J.W. Lee, Y.J. Choi, J.M. Yang, S. Ham, S.K. Jeon, J.Y. Lee, Y.H. Song, E.K. Ji, D.H. Yoon, S. Seo, H. Shin, G.S. Han, H.S. Jung, D. Kim, N.G. Park, ACS Nano 11 (2017) 3311–3319.
[110] Y. Wang, J. He, H. Chen, J. Chen, R. Zhu, P. Ma, A. Towers, Y. Lin, A.J. Gesquiere, S.-T. Wu, Y. Dong, Adv. Mater. 28 (2016) 10710–10717.
[111] A. Kojima, M. Ikegami, K. Teshima, T. Miyasaka, Chem. Lett. 41 (2012) 397–399.
[112] G. Longo, A. Pertegás, L. Martínez-Sarti, M. Sessolo, H.J. Bolink, J. Mater. Chem. C Mater. Opt. Electron. Devices 3 (2015) 11286–11289.
[113] V. Malgras, S. Tominaka, J.W. Ryan, J. Henzie, T. Takei, K. Ohara, Y. Yamauchi, J. Am. Chem. Soc. 138 (2016) 13874–13881.
[114] J.H. Im, C.R. Lee, J.W. Lee, S.W. Park, N.G. Park, Nanoscale 3 (2011) 4088–4093.
[115] C.F.J. Lau, X. Deng, J. Zheng, J. Kim, Z. Zhang, M. Zhang, J. Bing, B. Wilkinson, L. Hu, R. Patterson, S. Huang, A. Ho-Baillie, J. Mater. Chem. A Mater. Energy Sustain. 6 (2018) 5580–5586.
[116] B. Li, Y. Zhang, L. Fu, T. Yu, S. Zhou, L. Zhang, L. Yin, Nat. Commun. 9 (2018) 1076.
[117] J. Zhang, D. Bai, Z. Jin, H. Bian, K. Wang, J. Sun, Q. Wang, S.F. Liu, Adv. Energy Mater. 8 (2018) 1703246.
[118] J.S. Niezgoda, B.J. Foley, A.Z. Chen, J.J. Choi, ACS Energy Lett. 2 (2017) 1043–1049.
[119] A. Swarnkar, A.R. Marshall, E.M. Sanehira, B.D. Chernomordik, D.T. Moore, J.A. Christians, T. Chakrabarti, J.M. Luther, Science 354 (2016) 92–95.
[120] E.M. Sanehira, A.R. Marshall, J.A. Christians, S.P. Harvey, P.N. Ciesielski, L.M. Wheeler, P. Schulz, L.Y. Lin, M.C. Beard, J.M. Luther, Sci. Adv. 3 (2017) eaao4204.
[121] J. Song, J. Li, X. Li, L. Xu, Y. Dong, H. Zeng, Adv. Mater. 27 (2015) 7162–7167.
[122] J. Li, L. Xu, T. Wang, J. Song, J. Chen, J. Xue, Y. Dong, B. Cai, Q. Shan, B. Han, H. Zeng, Adv. Mater. 29 (2017) 1603885.
[123] X. Li, Y.-B. Zhao, F. Fan, L. Levina, M. Liu, R. Quintero-Bermudez, X. Gong, L.N. Quan, J. Fan, Z. Yang, S. Hoogland, O. Voznyy, Z.-H. Lu, E.H. Sargent, Nat. Photonics 12 (2018) 159–164.
[124] X. Zhang, H. Lin, H. Huang, C. Reckmeier, Y. Zhang, W.C.H. Choy, A.L. Rogach, Nano Lett. 16 (2016) 1415–1420.
[125] G. Li, F.W.R. Rivarola, N.J.L.K. Davis, S. Bai, T.C. Jellicoe, F. de la Peña, S. Hou, C. Ducati, F. Gao, R.H. Friend, N.C. Greenham, Z.-K. Tan, Adv. Mater. 28 (2016) 3528–3534.
[126] Y. Ling, Y. Tian, X. Wang, J.C. Wang, J.M. Knox, F. Perez-Orive, Y. Du, L. Tan, K. Hanson, B. Ma, H. Gao, Adv. Mater. 28 (2016) 8983–8989.
[127] G. Xing, N. Mathews, S.S. Lim, N. Yantara, X. Liu, D. Sabba, M. Grätzel, S. Mhaisalkar, T.C. Sum, Nat. Mater. 13 (2014) 476.
[128] S. Yakunin, L. Protesescu, F. Krieg, M.I. Bodnarchuk, G. Nedelcu, M. Humer, G. De Luca, M. Fiebig, W. Heiss, M.V. Kovalenko, Nat. Commun. 6 (2015) 8056.
[129] Y. Wang, X. Li, X. Zhao, L. Xiao, H. Zeng, H. Sun, Nano Lett. 16 (2016) 448–453.
[130] J. Pan, S.P. Sarmah, B. Murali, I. Dursun, W. Peng, M.R. Parida, J. Liu, L. Sinatra, N. Alyami, C. Zhao, E. Alarousu, T.K. Ng, B.S. Ooi, O.M. Bakr, O.F. Mohammed, J. Phys. Chem. Lett. 6 (2015) 5027–5033.
[131] P. Ramasamy, D.-H. Lim, B. Kim, S.-H. Lee, M.-S. Lee, J.-S. Lee, Chem. Commun. (Camb.) 52 (2016) 2067–2070.
[132] Y. Dong, Y. Gu, Y. Zou, J. Song, L. Xu, J. Li, J. Xue, X. Li, H. Zeng, Small 12 (2016) 5622–5632.
[133] C.C. Stoumpos, D.H. Cao, D.J. Clark, J. Young, J.M. Rondinelli, J.I. Jang, J.T. Hupp, M.G. Kanatzidis, Chem. Mater. 28 (2016) 2852–2867.
[134] Z. Yuan, C. Zhou, Y. Shu, Y. Tian, J. Messier, J. Wang, L. Burgt, K. Kountouriotis, Y. Xin, E. Holt, K.S. Schanze, R. Clark, T. Siegrist, B. Ma, Nat. Commun. 8 (2017) 14051.
[135] C. Zhou, H. Lin, H. Shi, Y. Tian, C. Pak, M. Shatruk, Y. Zhou, P. Djurovich, M.-H. Du, B. Ma, Angew. Chem. Int. Ed. 57 (2018) 1021–1024.
[136] C. Zhou, M. Worku, J. Neu, H. Lin, Y. Tian, S. Lee, Y. Zhou, D. Han, S. Chen, A. Hao, P.I. Djurovich, T. Siegrist, M.-H. Du, B. Ma, Chem. Mater. 30 (2018) 2374–2378.
[137] D. Wang, B. Wen, Y.-N. Zhu, C.-J. Tong, Z.-K. Tang, L.-M. Liu, J. Phys. Chem. Lett. 8 (2017) 876–883.
[138] Z. Xiao, W. Meng, J. Wang, D.B. Mitzi, Y. Yan, Mater. Horiz. 4 (2017) 206–216.
[139] M.D. Smith, H.I. Karunadasa, Acc. Chem. Res. 51 (2018) 619–627.
[140] M.C. Gelvez-Rueda, E.M. Hutter, D.H. Cao, N. Renaud, C.C. Stoumpos, J.T. Hupp, T.J. Savenije, M.G. Kanatzidis, F.C. Grozema, J. Phys. Chem. C 121 (2017) 26566–26574.
[141] K. Zheng, Y. Chen, Y. Sun, J. Chen, P. Chábera, R. Schaller, M.J. Al-Marri, S.E. Canton, Z. Liang, T. Pullerits, J. Mater. Chem. A Mater. Energy Sustain. 6 (2018) 6244–6250.
[142] A.H. Proppe, R. Quintero-Bermudez, H. Tan, O. Voznyy, S.O. Kelley, E.H. Sargent, J. Am. Chem. Soc. 140 (2018) 2890–2896.
[143] W. Liu, J. Xing, J. Zhao, X. Wen, K. Wang, P. Lu, Q. Xiong, Adv. Opt. Mater. 5 (2017) 1601045.
[144] I. Neogi, A. Bruno, D. Bahulayan, T.W. Goh, B. Ghosh, R. Ganguly, D. Cortecchia, T.C. Sum, C. Soci, N. Mathews, S.G. Mhaisalkar, ChemSusChem 10 (2017) 3765–3772.
[145] Z. Yuan, Y. Shu, Y. Xin, B. Ma, Chem. Commun. (Camb.) 52 (2016) 3887–3890.
[146] H. Tsai, W. Nie, J.C. Blancon, C.C. Stoumpos, R. Asadpour, B. Harutyunyan, A.J. Neukirch, R. Verduzco, J.J. Crochet, S. Tretiak, L. Pedesseau, J. Even, M.A. Alam, G. Gupta, J. Lou, P.M. Ajayan, M.J. Bedzyk, M.G. Kanatzidis, Nature 536 (2016) 312–316.
[147] Y. Tian, C. Zhou, M. Worku, X. Wang, Y. Ling, H. Gao, Y. Zhou, Y. Miao, J. Guan, B. Ma, Adv. Mater. 30 (2018) 1707093.
[148] D.Y. I, I. Tamotsu, M. Yusei, Bull. Chem. Soc. Jpn. 59 (1986) 563–567.
[149] T. Ishihara, J. Takahashi, T. Goto, Solid State Commun. 69 (1989) 933–936.
[150] J. Chen, L. Gan, F. Zhuge, H. Li, J. Song, H. Zeng, T. Zhai, Angew. Chem. Int. Ed. 56 (2017) 2390–2394.
[151] Q. Zhang, L. Chu, F. Zhou, W. Ji, G. Eda, Adv. Mater. 30 (2018) 1704055.
[152] V.V. Naik, S. Vasudevan, J. Phys. Chem. C 114 (2010) 4536–4543.
[153] C.M.M. Soe, C.C. Stoumpos, Ml. Kepenekian, B. Traoré, H. Tsai, W. Nie, B. Wang, C. Katan, R. Seshadri, A.D. Mohite, J. Even, T.J. Marks, M.G. Kanatzidis, J. Am. Chem. Soc. 139 (2017) 16297–16309.
[154] L. Li, Z. Sun, P. Wang, W. Hu, S. Wang, C. Ji, M. Hong, J. Luo, Angew. Chem. Int. Ed. 56 (2017) 12150–12154.
[155] L. Mao, Y. Wu, C.C. Stoumpos, B. Traore, C. Katan, J. Even, M.R. Wasielewski, M.G. Kanatzidis, J. Am. Chem. Soc. 139 (2017) 11956–11963.
[156] S. Aharon, L. Etgar, Nano Lett. 16 (2016) 3230–3235.
[157] P. Cheng, T. Wu, J. Liu, W.Q. Deng, K. Han, J. Phys. Chem. Lett. 9 (2018) 2518–2522.
[158] L. Ma, M.G. Ju, J. Dai, X.C. Zeng, Nanoscale 10 (2018) 11314–11319.
[159] C.J. Que, C.J. Mo, Z.Q. Li, G.L. Zhang, Q.Y. Zhu, J. Dai, Inorg. Chem. 56 (2017) 2467–2472.
[160] L. Mao, W. Ke, L. Pedesseau, Y. Wu, C. Katan, J. Even, M.R. Wasielewski, C.C. Stoumpos, M.G. Kanatzidis, J. Am. Chem. Soc. 140 (2018) 3775–3783.
[161] C.M.M. Soe, W. Nie, C.C. Stoumpos, H. Tsai, J.-C. Blancon, F. Liu, J. Even, T.J. Marks, A.D. Mohite, M.G. Kanatzidis, Adv. Energy Mater. 8 (2018) 1700979.
[162] A.Z. Chen, M. Shiu, J.H. Ma, M.R. Alpert, D. Zhang, B.J. Foley, D.M. Smilgies, S.H. Lee, J.J. Choi, Nat. Commun. 9 (2018) 1336.
[163] J.V. Passarelli, D.J. Fairfield, N.A. Sather, M.P. Hendricks, H. Sai, C.L. Stern, S.I. Stupp, J. Am. Chem. Soc. 140 (2018) 7313–7323.
[164] J. Liu, J. Leng, K. Wu, J. Zhang, S. Jin, J. Am. Chem. Soc. 139 (2017) 1432–1435.
[165] L. Yan, J. Hu, Z. Guo, H. Chen, M.F. Toney, A.M. Moran, W. You, ACS Appl. Mater. Interfaces 10 (2018) 33187–33197.
[166] O.F. Williams, Z. Guo, J. Hu, L. Yan, W. You, A.M. Moran, J. Chem. Phys. 148 (2018) 134706.
[167] M. Era, S. Morimoto, T. Tsutsui, S. Saito, Appl. Phys. Lett. 65 (1994) 676–678.
[168] T. Hattori, T. Taira, M. Era, T. Tsutsui, S. Saito, Chem. Phys. Lett. 254 (1996) 103–108.
[169] H. Tsai, W. Nie, J.C. Blancon, C.C. Stoumpos, C.M.M. Soe, J. Yoo, J. Crochet, S. Tretiak, J. Even, A. Sadhanala, Adv. Mater. 30 (2018) 1704217.
[170] N. Wang, L. Cheng, R. Ge, S. Zhang, Y. Miao, W. Zou, C. Yi, Y. Sun, Y. Cao, R. Yang, Y. Wei, Q. Guo, Y. Ke, M. Yu, Y. Jin, Y. Liu, Q. Ding, D. Di, L. Yang, G. Xing, H. Tian, C. Jin, F. Gao, R.H. Friend, J. Wang, W. Huang, Nat. Photonics 10 (2016) 699–704.
[171] M. Yuan, L.N. Quan, R. Comin, G. Walters, R. Sabatini, O. Voznyy, S. Hoogland, Y. Zhao, E.M. Beauregard, P. Kanjanaboos, Z. Lu, D.H. Kim, E.H. Sargent, Nat. Nanotechnol. 11 (2016) 872.
[172] B. Zhao, S. Bai, V. Kim, R. Lamboll, R. Shivanna, F. Auras, J.M. Richter, L. Yang, L. Dai, M. Alsari, X.-J. She, L. Liang, J. Zhang, S. Lilliu, P. Gao, H.J. Snaith, J. Wang, N.C. Greenham, R.H. Friend, D. Di, Nat. Photonics 12 (2018) 783–789.
[173] C.R. Kagan, D.B. Mitzi, C.D. Dimitrakopoulos, Science 286 (1999) 945–947.
[174] D.B. Mitzi, C.D. Dimitrakopoulos, L.L. Kosbar, Chem. Mater. 13 (2001) 3728–3740.
[175] H. Zhang, Q. Liao, Y. Wu, Z. Zhang, Q. Gao, P. Liu, M. Li, J. Yao, H. Fu, Adv. Mater. 30 (2018) 1706186.
[176] C.M. Raghavan, T.P. Chen, S.S. Li, W.L. Chen, C.Y. Lo, Y.M. Liao, G. Haider, C.C. Lin, C.C. Chen, R. Sankar, Y.M. Chang, F.C. Chou, C.W. Chen, Nano Lett. 18 (2018) 3221–3228.
[177] P. Odenthal, W. Talmadge, N. Gundlach, R. Wang, C. Zhang, D. Sun, Z.-G. Yu, Z. Valy Vardeny, Y.S. Li, Nat. Phys. 13 (2017) 894–899.
[178] Y. Chen, Y. Sun, J. Peng, J. Tang, K. Zheng, Z. Liang, Adv. Mater. 30 (2018) 1703487.
[179] M.D. Smith, E.J. Crace, A. Jaffe, H.I. Karunadasa, Annu. Rev. Mater. Res. 48 (2018) 111–136.
[180] D.B. Mitzi, S. Wang, C.A. Feild, C.A. Chess, A.M. Guloy, Science 267 (1995) 1473–1476.
[181] J. Guan, Z. Tang, A.M. Guloy, Chem. Commun. (Camb.) (1999) 1833–1834.
[182] L. Mao, H. Tsai, W. Nie, L. Ma, J. Im, C.C. Stoumpos, C.D. Malliakas, F. Hao, M.R. Wasielewski, A.D. Mohite, M.G. Kanatzidis, Chem. Mater. 28 (2016) 7781–7792.
[183] Y.Y. Li, C.K. Lin, G.L. Zheng, Z.Y. Cheng, H. You, W.D. Wang, J. Lin, Chem. Mater. 18 (2006) 3463–3469.
[184] L. Mao, Y. Wu, C.C. Stoumpos, M.R. Wasielewski, M.G. Kanatzidis, J. Am. Chem. Soc. 139 (2017) 5210–5215.
[185] B. Saparov, D.B. Mitzi, Chem. Rev. 116 (2016) 4558–4596.

[186] T. Hu, M.D. Smith, E.R. Dohner, M.J. Sher, X. Wu, M.T. Trinh, A. Fisher, J. Corbett, X.Y. Zhu, H.I. Karunadasa, A.M. Lindenberg, J. Phys. Chem. Lett. 7 (2016) 2258–2263.
[187] Z. Wu, C. Ji, Z. Sun, S. Wang, S. Zhao, W. Zhang, L. Li, J. Luo, J. Mater. Chem. C Mater. Opt. Electron. Devices 6 (2018) 1171–1175.
[188] J. Yin, H. Li, D. Cortecchia, C. Soci, J.-L. Brédas, ACS Energy Lett. 2 (2017) 417–423.
[189] D. Cortecchia, J. Yin, A. Bruno, S.-Z.A. Lo, G.G. Gurzadyan, S. Mhaisalkar, J.-L. Bredas, C. Soci, J. Mater. Chem. C Mater. Opt. Electron. Devices 5 (2017) 2771–2780.
[190] J.P. Perdew, K. Burke, M. Ernzerhof, Phys. Rev. Lett. 77 (1996) 3865.
[191] M.-H. Du, S.B. Zhang, Phys. Rev. B 80 (2009) 115217.
[192] J.B. Varley, A. Janotti, C. Franchini, C.G. Van de Walle, Phys. Rev. B 85 (2012) 081109.
[193] P. Chen, Y. Bai, M. Lyu, J.-H. Yun, M. Hao, L. Wang, Sol. Rrl 2 (2018) 1700186.
[194] D.B. Mitzi, Dalton T. (2001) 1-12.
[195] S. Wang, D.B. Mitzi, C.A. Feild, A. Guloy, J. Am. Chem. Soc. 117 (1995) 5297–5302.
[196] L. Mao, P. Guo, M. Kepenekian, I. Hadar, C. Katan, J. Even, R.D. Schaller, C.C. Stoumpos, M.G. Kanatzidis, J. Am. Chem. Soc. 140 (2018) 13078–13088.
[197] C.K. Zhou, Y. Tian, O. Khabou, M. Worku, Y. Zhou, J. Hurley, H.R. Lin, B.W. Ma, ACS Appl. Mater. Interfaces 9 (2017) 40446–40451.
[198] G. Wu, C. Zhou, W. Ming, D. Han, S. Chen, D. Yang, T. Besara, J. Neu, T. Siegrist, M.-H. Du, B. Ma, A. Dong, ACS Energy Lett. 3 (2018) 1443–1449.
[199] C.K. Zhou, Y. Tian, M.C. Wang, A. Rose, T. Besara, N.K. Doyle, Z. Yuan, J.C. Wang, R. Clark, Y.Y. Hu, T. Siegrist, S.C. Lin, B.W. Ma, Angew. Chem. Int. Ed. 56 (2017) 9018–9022.
[200] H. Lin, C. Zhou, Y. Tian, T. Besara, J. Neu, T. Siegrist, Y. Zhou, J. Bullock, K.S. Schanze, W. Ming, M.H. Du, B. Ma, Chem. Sci. 8 (2017) 8400–8404.
[201] Y.-Z. Ma, H. Lin, M.-H. Du, B. Doughty, B. Ma, J. Phys. Chem. Lett. 9 (2018) 2164–2169.
[202] G.A. Mousdis, N.-M. Ganotopoulos, H. Barkaoui, Y. Abid, V. Psycharis, A. Savvidou, C.P. Raptopoulou, Eur. J. Inorg. Chem. 2017 (2017) 3401–3408.
[203] J. Zhang, S. Han, X. Liu, Z. Wu, C. Ji, Z. Sun, J. Luo, Chem. Commun. (Camb.) 54 (2018) 5614–5617.
[204] H. Dammak, S. Triki, A. Mlayah, Y. Abid, H. Feki, J. Lumin. 166 (2015) 180–186.
[205] W. Zhang, K. Tao, C. Ji, Z. Sun, S. Han, J. Zhang, Z. Wu, J. Luo, Inorg. Chem. 57 (2018) 4239–4243.
[206] M. Nikl, E. Mihokova, K. Nitsch, F. Somma, C. Giampaolo, G. Pazzi, P. Fabeni, S. Zazubovich, Chem. Phys. Lett. 306 (1999) 280–284.
[207] H.R. Lin, C.K. Zhou, Y. Tian, T. Siegrist, B.W. Ma, ACS Energy Lett. 3 (2018) 54–62.
[208] D. Han, H. Shi, W. Ming, C. Zhou, B. Ma, B. Saparov, Y.-Z. Ma, S. Chen, M.-H. Du, J. Mater. Chem. C Mater. Opt. Electron. Devices 6 (2018) 6398–6405.
[209] C.K. Zhou, Y. Tian, Z. Yuan, H.R. Lin, B.H. Chen, R. Clark, T. Dilbeck, Y. Zhou, J. Hurley, J. Neu, T. Besara, T. Siegrist, P. Djurovich, B.W. Ma, ACS Appl. Mater. Interfaces 9 (2017) 44579–44583.
[210] L.-J. Xu, C.-Z. Sun, H. Xiao, Y. Wu, Z.-N. Chen, Adv. Mater. 29 (2017) 1605739.
[211] M. Worku, Y. Tian, C. Zhou, S. Lee, Q. Meisner, Y. Zhou, B. Ma, ACS Appl. Mater. Interfaces 10 (2018) 30051–30057.
[212] T. Kawai, A. Ishii, T. Kitamura, S. Shimanuki, M. Iwata, Y. Ishibashi, J. Phys. Soc. Jpn. 65 (1996) 1464–1468.
[213] C. Zhou, H. Lin, M. Worku, J. Neu, Y. Zhou, Y. Tian, S. Lee, P.I. Djurovich, T. Siegrist, B. Ma, J. Am. Chem. Soc. 140 (2018) 13181–13184.
[214] J.-C. Hebig, I. Kühn, J. Flohre, T. Kirchartz, ACS Energy Lett. 1 (2016) 309–314.
[215] S. Oz, J.C. Hebig, E.W. Jung, T. Singh, A. Lepcha, S. Olthof, J. Flohre, Y.J. Gao, R. German, P.H.M. van Loosdrecht, K. Meerholz, T. Kirchartz, S. Mathur, Sol. Energy Mater. Sol. Cells 158 (2016) 195–201.
[216] B.W. Park, B. Philippe, X. Zhang, H. Rensmo, G. Boschloo, E.M. Johansson, Adv. Mater. 27 (2015) 6806–6813.
[217] J.K. Pious, M.L. Lekshmi, C. Muthu, R.B. Rakhi, V.C. Nair, ACS Omega 2 (2017) 5798–5802.
[218] Y. Wu, D. Han, B. Chakumakos, H. Shi, S. Chen, M.H. Du, I. Greeley, M. Loyd, D.J. Rutstrom, L. Stand, J. Mater. Chem. C Mater. Opt. Electron. Devices 6 (2018) 6647–6655.
[219] Z. Tan, J. Li, C. Zhang, Z. Li, Q. Hu, Z. Xiao, T. Kamiya, H. Hosono, G. Niu, E. Lifshitz, Adv. Funct. Mater. 28 (2018) 1801131.
[220] S.C. Sevov, Zintl Phases, J.H. Westbrook, R.L. Fleischer (Eds.), Intermetallic Compounds-Principles and Practice, vol 3, John Wiley & Sons, Ltd, 2002.
[221] S. Kondo, K. Amaya, T. Saito, J. Phys. Condens. Matter 14 (2002) 2093–2099.
[222] M. De Bastiani, I. Dursun, Y. Zhang, B.A. Alshankiti, X.-H. Miao, J. Yin, E. Yengel, E. Alarousu, B. Turedi, J.M. Almutlaq, M.I. Saidaminov, S. Mitra, I. Gereige, A. AlSaggaf, Y. Zhu, Y. Han, I.S. Roqan, J.-L. Bredas, O.F. Mohammed, O.M. Bakr, Chem. Mater. 29 (2017) 7108–7113.
[223] J. Yin, P. Maity, M. De Bastiani, I. Dursun, O.M. Bakr, J.-L. Brédas, O.F. Mohammed, Sci. Adv. 3 (2017) e1701793.
[224] Q.A. Akkerman, A.L. Abdelhady, L. Manna, J. Phys. Chem. Lett. 9 (2018) 2326–2337.
[225] Q.A. Akkerman, S. Park, E. Radicchi, F. Nunzi, E. Mosconi, F. De Angelis, R. Brescia, P. Rastogi, M. Prato, L. Manna, Nano Lett. 17 (2017) 1924–1930.
[226] M.I. Saidaminov, J. Almutlaq, S. Sarmah, I. Dursun, A.A. Zhumekenov, R. Begum, J. Pan, N. Cho, O.F. Mohammed, O.M. Bakr, ACS Energy Lett. 1 (2016) 840–845.
[227] Y. Zhang, M.I. Saidaminov, I. Dursun, H. Yang, B. Murali, E. Alarousu, E. Yengel, B.A. Alshankiti, O.M. Bakr, O.F. Mohammed, J. Phys. Chem. Lett. 8 (2017) 961–965.
[228] Y. Zhang, L. Sinatra, E. Alarousu, J. Yin, A.M. El-Zohry, O.M. Bakr, O.F. Mohammed, J. Phys. Chem. C 122 (2018) 6493–6498.
[229] X. Chen, D. Chen, J. Li, G. Fang, H. Sheng, J. Zhong, Dalton Trans. 47 (2018) 5670–5678.
[230] J. Heyd, G.E. Scuseria, M. Ernzerhof, J. Chem. Phys. 118 (2003) 8207–8215.
[231] A.V. Krukau, O.A. Vydrov, A.F. Izmaylov, G.E. Scuseria, J. Chem. Phys. 125 (2006) 224106.
[232] B. Kang, K. Biswas, J. Phys. Chem. Lett. 9 (2018) 830–836.
[233] S. Seth, A. Samanta, J. Phys. Chem. Lett. 8 (2017) 4461–4467.
[234] G. Niu, W. Li, F. Meng, L. Wang, H. Dong, Y. Qiu, J. Mater. Chem. A Mater. Energy Sustain. 2 (2014) 705–710.
[235] A.M.A. Leguy, Y. Hu, M. Campoy-Quiles, M.I. Alonso, O.J. Weber, P. Azarhoosh, M. van Schilfgaarde, M.T. Weller, T. Bein, J. Nelson, P. Docampo, P.R.F. Barnes, Chem. Mater. 27 (2015) 3397–3407.
[236] J.M. Frost, K.T. Butler, F. Brivio, C.H. Hendon, M. van Schilfgaarde, A. Walsh, Nano Lett. 14 (2014) 2584–2590.
[237] N. Aristidou, I. Sanchez-Molina, T. Chotchuangchutchaval, M. Brown, L. Martinez, T. Rath, S.A. Haque, Angew. Chem. Int. Ed. 54 (2015) 8208–8212.
[238] D. Bryant, N. Aristidou, S. Pont, I. Sanchez-Molina, T. Chotchunangatchaval, S. Wheeler, J.R. Durrant, S.A. Haque, Energy Environ. Sci. 9 (2016) 1655–1660.
[239] Y. Yuan, J. Chae, Y. Shao, Q. Wang, Z. Xiao, A. Centrone, J. Huang, Adv. Energy Mater. 5 (2015) 1500615.
[240] E.T. Hoke, D.J. Slotcavage, E.R. Dohner, A.R. Bowring, H.I. Karunadasa, M.D. McGehee, Chem. Sci. 6 (2015) 613–617.
[241] Y. Yuan, J. Huang, Acc. Chem. Res. 49 (2016) 286–293.
[242] T. Baikie, Y.N. Fang, J.M. Kadro, M. Schreyer, F.X. Wei, S.G. Mhaisalkar, M. Graetzel, T.J. White, J. Mater. Chem. A Mater. Energy Sustain. 1 (2013) 5628–5641.
[243] G.D. Niu, X.D. Guo, L.D. Wang, J. Mater. Chem. A Mater. Energy Sustain. 3 (2015) 8970–8980.
[244] T.A. Berhe, W.N. Su, C.H. Chen, C.J. Pan, J.H. Cheng, H.M. Chen, M.C. Tsai, L.Y. Chen, A.A. Dubale, B.J. Hwang, Energy Environ. Sci. 9 (2016) 323–356.
[245] M.L. Petrus, J. Schlipf, C. Li, T.P. Gujar, N. Giesbrecht, P. Muller-Buschbaum, M. Thelakkat, T. Bein, S. Huttner, P. Docampo, Adv. Energy Mater. 7 (2017) 1700264.
[246] A. Rajagopal, K. Yao, A.K. Jen, Adv. Mater. 30 (2018) 1800455.
[247] L.N. Quan, M. Yuan, R. Comin, O. Voznyy, E.M. Beauregard, S. Hoogland, A. Buin, A.R. Kirmani, K. Zhao, A. Amassian, D.H. Kim, E.H. Sargent, J. Am. Chem. Soc. 138 (2016) 2649–2655.
[248] Y. Lin, Y. Bai, Y. Fang, Q. Wang, Y. Deng, J. Huang, ACS Energy Lett. 2 (2017) 1571–1572.
[249] Y. Peng, Y. Yao, L. Li, Z. Wu, S. Wang, J. Luo, J. Mater. Chem. C Mater. Opt. Electron. Devices 6 (2018) 6033–6037.
[250] W. Liu, K. Zhu, S.J. Teat, G. Dey, Z. Shen, L. Wang, D.M. O'Carroll, J. Li, J. Am. Chem. Soc. 139 (2017) 9281–9290.